
Masters Theses

Student Theses and Dissertations

Spring 2022

Experimental optimization of simulated ring rolling operation for heavy rail industry

Jacob M. Summers

Follow this and additional works at: https://scholarsmine.mst.edu/masters_theses



Part of the [Metallurgy Commons](#)

Department:

Recommended Citation

Summers, Jacob M., "Experimental optimization of simulated ring rolling operation for heavy rail industry" (2022). *Masters Theses*. 8098.

https://scholarsmine.mst.edu/masters_theses/8098

This thesis is brought to you by Scholars' Mine, a service of the Missouri S&T Library and Learning Resources. This work is protected by U. S. Copyright Law. Unauthorized use including reproduction for redistribution requires the permission of the copyright holder. For more information, please contact scholarsmine@mst.edu.

EXPERIMENTAL OPTIMIZATION OF SIMULATED RING ROLLING OPERATION
FOR HEAVY RAIL INDUSTRY

by

JACOB MICHAEL SUMMERS

A THESIS

Presented to the Graduate Faculty of the
MISSOURI UNIVERSITY OF SCIENCE AND TECHNOLOGY

In Partial Fulfillment of the Requirements for the Degree

MASTERS OF SCIENCE

in

METALLURGICAL ENGINEERING

2022

Approved by:

Laura N. Bartlett, Advisor

Ronald J. O'Malley

Mario F. Buchely

Richard Pilon

© 2022

Jacob Michael Summers

All Rights Reserved

PUBLICATION THESIS OPTION

This thesis consists of the following three articles, formatted in the style used by the Missouri University of Science and Technology:

Paper I, found on pages 32–60, have been accepted for publication in the proceedings of the Cast Expo 2022 Conference in Columbus, Ohio, in April 2022.

Paper II, found on pages 61–100, is intended for submission to *International Journal of Metalcasting*.

Paper III, found on pages 101–121, is intended for submission to *Journals of Materials Research and Technology*.

ABSTRACT

Industrially cast AISI 1070 steel wheel pre-forms from Amsted Rail Co. were experimentally hot rolled to simulate the conditions for industrial wheel rolling. Ring rolling of near net shape castings can improve location specific properties by decreasing segregation, closing porosity, and reducing grain size without the use of multiple forging operations in a traditional forging line. As-cast wheel sections were subjected to thermomechanical processing routes using a 2-high rolling mill in a temperature range of 830°C to 1200°C. The goal being to simulate the ring rolling process and optimize benefits of mechanical properties of the as-rolled steel. Charpy V- and U-notch impact tests were conducted at -20°C and 20°C, respectively, as a function of thermomechanical processing and notch orientation. Mitigation of cast defects such as inclusions and shrinkage porosity by hot rolling were quantified utilizing scanning electron microscopy and micro-computed X-Ray tomography. Microshrinkage porosity was shown to be virtually eliminated at a 66% reduction. A rolling temperature of 830°C resulted in a 114% increase in KCU at 20°C and 67% increase at -20°C in KCV for L-S impact properties through refinement of prior austenite grain size. Anisotropy related to MnS stringers in the rolling direction were the primary cause for reduction in impact toughness in the T-L orientation although grain texture also likely plays a role. Hot tensile tests performed between 830°C to 1200°C in strain rates of 0.1 to 10 s⁻¹ were utilized to develop a Johnson-Cook Strength model. The experimental parameters determined from the Johnson-Cook model were used as inputs to develop a Finite Element Analysis model of the modified wheel rolling process utilizing FORGE NxT software.

ACKNOWLEDGMENTS

I would like to acknowledge my committee, the Peaslee Steel Manufacturing Research Center (PSMRC) group, and our corporate sponsor, Amsted Rail, for their support and efforts which have made this work possible. I would like to thank each individual member of my committee, Dr. Mario Buchely, Dr. Laura Bartlett, and Dr. Ronald O'Malley for their patience, guidance, and advice throughout the duration of the project. Their expertise and insight have added immeasurable value to this work as well as my own knowledge of the subjects. The ability to partake in open forum discussions with members of the PSMRC, students and professors alike, allowed for an understanding of new ideas and new questions from outside observers on the work which aided in the development of the practices herein. And of course, this work would not have been possible without the contributions of our corporate sponsor, Amsted Rail and specifically Richard Pilon. Their support was the foundation for which this work was performed and the motivation behind the experimental simulation of the industrial wheel rolling process. Their interest and excitement for this project fueled the research and inspired us to strive towards excellence throughout this work. I am proud to have worked with all these individuals and am very thankful for their contributions. I would also like to thank Nicolas Poulain and Tara Selly for their invaluable service during this work. Nicolas Poulain and Transvalor Americas performed the Finite Element Analysis simulation of the modified wheel rolling process presented in this work. Tara Selly performed the micro-X-Ray-CT-scans utilized for volumetric investigation of shrinkage porosity

TABLE OF CONTENTS

	Page
PUBLICATION THESIS OPTION	iii
ABSTRACT	iv
ACKNOWLEDGMENTS	v
LIST OF ILLUSTRATIONS	ix
LIST OF TABLES	xv
 SECTION	
1. INTRODUCTION.....	1
1.1. OVERVIEW.....	1
1.2. INDUSTRIAL PROCESS OF WHEEL FABRICATION.....	10
1.2.1. Griffin Wheel Casting Process.	10
1.2.2. Forging Process.....	13
2. LITERATURE REVIEW	17
2.1. INFLUENCE OF MICROSTRUCTURE ON MECHANICAL PROPERTIES OF EUTECTOID STEELS	17
2.1.1. Influence of Microstructure on the Mechanical Properties of Steel Castings.....	17
2.1.2. Effect of Forging on Microstructure and Mechanical Properties.	19
2.1.3. Role of Inclusions and Porosity on Impact Toughness.	23
2.2. MODELING THE INDUSTRIAL RING ROLLING PROCESS.....	27
2.2.1. Experimental Modeling of the Ring Rolling Process.	28
2.2.2. Finite Element Analysis Modeling of the Ring Rolling Process.	29

PAPER

I. EVALUATION OF NOTCH TOUGHNESS AFTER SIMULATED RING-ROLLING OF AISI 1070 STEEL WHEEL CASTINGS	32
ABSTRACT	32
1. INTRODUCTION.....	33
2. DESIGN OF EXPERIMENTS	36
3. RESULTS AND DISCUSSION	41
4. CONCLUSIONS.....	56
ACKNOWLEDGMENTS	58
REFERENCES	58
II. ON THE EFFECT OF HOT ROLLING ON INCLUSION SIZE AND DISTRIBUTION IN AN AISI 1070 STEEL.....	61
ABSTRACT	61
1. BACKGROUND.....	62
2. INTRODUCTION.....	65
3. PROCEDURE.....	67
4. RESULTS AND DISCUSSION	72
4.1. AFA POROSITY RESULTS	72
4.2. AFA INCLUSION RESULTS	76
5. CONCLUSIONS.....	96
ACKNOWLEDGMENTS	97
APPENDIX.....	97
REFERENCES	98
III. HIGH TEMPERATURE JOHNSON-COOK STRENGTH OF A HIGH CARBON STEEL	101

ABSTRACT	101
1. INTRODUCTION.....	102
2. MATERIALS AND METHODS.....	104
3. RESULTS AND DISCUSSION	107
4. CONCLUSIONS.....	119
ACKNOWLEDGMENTS	120
REFERENCES	120
SECTION	
3. CONCLUSIONS AND RECOMMENDATIONS	122
3.1. CONCLUSIONS.....	122
3.1.1. Impact Testing and Characterization.	122
3.1.2. Hot Rolling and Shrinkage Porosity and Nonmetallic Inclusions.	125
3.1.3. Johnson-Cook Strength Model and Finite Element Analysis Simulation.....	126
3.2. RECOMMENDATIONS	126
BIBLIOGRAPHY	128
VITA.....	133

LIST OF ILLUSTRATIONS

SECTION	Page
Figure 1.1. A schematic drawing of the contour of train wheels and nomenclature for relevant areas (a) and a principal failure mode of freight wheels during severe braking conditions resulting in brittle fracture (b). ⁴	4
Figure 1.2. Locations of tensile and Charpy impact specimens for examination of railway wheels. ⁵	6
Figure 1.3. In the Griffin process, the graphite mold is positioned over the ladle and a ceramic pouring tube extends into the melt below.	10
Figure 1.4. Depiction of equiaxed versus columnar solidification during billet casting.	11
Figure 1.5. As-cast wheel geometry prior to dishing operation.	13
Figure 1.6. Depiction of the forging process of industrially produced railway wheels. ¹²	14
Figure 1.7. “A schematic diagram illustrating the main recrystallization mechanisms during deformation. The dislocation density decreases as the re-crystallized dislocation-free volume fraction increases over time (or strain)”. ¹⁰	14
Figure 2.1. The Fe-C phase diagram which shows that the eutectoid composition is 0.8 % C.	18
Figure 2.2. Standard end-quench (Jominy) test displaying the relationship between C and alloy additions on the relationship with hardenability with peak hardness being controlled by C content. ¹⁴	19
Figure 2.3. Hyzak & Bernstein demonstrated that the yield strength and hardness of pearlitic steels follow a Hall-Petch relationship. ¹⁵	20
Figure 2.4. An example of Type II MnS sulfide formation in an as-cast 0.25 wt. % C steel. ³⁰	25
Figure 2.5. Unpolished images showing example of gas porosity (a) and shrinkage porosity (b) in an AA 5182 remelt secondary ingot. ³¹	26

Figure 2.6. A drawing outlining the effects of gas porosity on fracture during impact testing.	26
Figure 2.7. A schematic drawing of the ring rolling process including the mandrel and drive roll which are driven and induce the deformation of the ring and the expansion and the guide roll and axial rolls which guide the expansion. ³³	27
Figure 2.8. Schematic diagram indicating the wheel blank shape prior to wheel rolling, and after wheel rolling.	28
Figure 2.9. Schematic illustration of a vertical wheel mill. ³⁵	30
 PAPER I	
Figure 1. Sectioning methodology adopted for rolling samples as well as Charpy testing orientations used for as-cast and as-rolled material for comparison.	37
Figure 2. The steel casting was soaked in an electric box furnace with SiC elements for 1.5 hrs at the process temperature before hot rolling and subsequent slow cooling ($\sim 0.1s^{-1}$) in a refractory blanket.	38
Figure 3. Phase transformations during equilibrium solidification and cooling as predicted for AISI 1070 steel in JMatPro.	39
Figure 4. (a) Macroetch showing segregation in the web section of the wheel casting as shown in Figure 1. (b) Quantitative chemistry measurements at locations through the thickness of the casting.	42
Figure 5. Increases in the alloying elements and impurities are observed at the casting center line (red arrow), confirming centerline segregation.	43
Figure 6. Average PAG size vs. isothermal rolling temperature is depicted with the standard sample deviation (a). Histograms per isothermal rolling temperatures at 830°C (b), 900°C (c), 1000°C (d), and 1200°C (e).	45
Figure 7. Optical micrograph of the as-cast material which represents the longitudinal orientation and is sectioned from centerline segregation region of the casting as depicted in Figure 4a.	47
Figure 8. Optical micrographs of as-rolled specimens in the longitudinal orientation showing mainly a microstructure of pearlite.	48

Figure 9. Optical micrographs of as-rolled specimens in the longitudinal orientation showing mainly a microstructure of pearlite with some proeutectoid ferrite, PF.	48
Figure 10. Charpy V- and U-notch impact results at -20°C and 20°C, respectively and in different orientations with the rolling direction (a) L-S orientation, (b) T-S orientation, and (c) T-L orientation.	50
Figure 11. SEM fractography of fracture surfaces of the as-cast material (BE=2.8 J).	52
Figure 12. SEM fractography images of the as-rolled specimens in the L-S orientation.	52
Figure 13. SE images (etched with 4% Picral) just below the fracture surfaces of the as-cast specimen show that porosity is prevalent.	54
Figure 14. SE images just below the fracture surface of hot rolled specimens tested at 20°C in the L-S orientation.....	54
Figure 15. EDS measurements obtained for comparison of MnS to matrix material in the L-S orientation of the as-rolled sample held isothermally at 1200°C.	56
 PAPER II	
Figure 1. Radiography measurements of porosity in fatigue specimens and correlated results to measured modulus in GPa showing the detrimental effects of porosity on stiffness. ⁶	63
Figure 2. Relationship between oxide inclusion volume and service durability (SD) in tons during experimental ARIRT ring testing of oxide inclusions smaller than 8 μm (open circles, R ² =0.92), and oxide inclusions greater than 8 μm (closed circles, R ² =0.70). ⁸	64
Figure 3. Depicted is a schematic of the effects of hot rolling on different types of inclusions (a) and the effect of projected length per unit area on upper shelf energy in a low C steel (b). ^{10,11}	65
Figure 4. The steel casting was soaked in an electric box furnace with SiC elements for 1.5 hrs at the process temperature before hot rolling and subsequent slow cooling (~0.1s ⁻¹) in a refractory blanket.	68
Figure 5. Aspek PICA-1020 performed in a stitched scan for shrinkage porosity and NMIs.	70

Figure 6. The location of the rolled samples as well as the sampling location is in the equiaxed region including the centerline segregation region for the as-cast and as-rolled samples.	71
Figure 7. Depiction of the sectioning method used to prepare cross sections of fracture area to determine NMI and shrinkage porosity interaction with the primary crack.	71
Figure 8. Area fraction (ppm) versus mean pore diameter (μm) in the as-cast and as-rolled conditions.	73
Figure 9. CT-scans of the as-cast (a) and as-rolled 1000°C (b) sample which visualizes the degree of closure of porosity at a 66% cumulative reduction.	77
Figure 10. Central region (3.2 mm height) of the micro-X-Ray CT-scans in the as-cast (a,b) and as-rolled 1000°C (c,d) conditions.	77
Figure 11. Area/Volume Fraction (ppm) of the as-cast and as-rolled 1000°C samples.	78
Figure 12. Optical microscopy of large shrinkage porosity ($\sim 1500 \mu\text{m}$).	79
Figure 13. EDS spectrum of MnS inclusions.	81
Figure 14. EDS spectrum of Al_2O_3 cluster.	81
Figure 15. EDS spectrum of globular complex inclusion of Al_2O_3 and MnS inclusions.	81
Figure 16. Ternary classification of the results from the Aspex AFA of the as-cast, as-rolled 830°C, and 1200°C along with a pie chart of the overall NMI size (%) are depicted.....	83
Figure 17. Ternary classification of the results from the Aspex AFA of the as-rolled conditions 900°C and 1000°C along with a pie chart of the overall NMI size (%) in the T-L direction.....	84
Figure 18. A graphical representation of the area fraction of the NMIs in each condition for the T-L (a) and L-S (b) orientations.	87
Figure 19. The average size, distribution, and morphology of MnS inclusions were examined from the Aspex PICA-1020 results on log-log plots.....	89

Figure 20. The average size, distribution, and morphology of Al_2O_3 inclusions were examined from the Aspex PICA-1020 results on log-log plots.....	90
Figure 21. The average size, distribution, and morphology of complex inclusions were examined from the Aspex PICA-1020 results on log-log plots.....	91
Figure 22. BSE images of a cross section of the fracture surface is depicted in Figure 2.....	94
Figure 23. SE images of Type II MnS interaction with secondary cracks.	95
Figure 24. SE images of Type II MnS interaction with secondary cracks in the T-L bars.	95
 PAPER III	
Figure 1. Depicted are the hot tensile samples (a) and the MTS hydraulic load frame and a depiction of the grip configuration (b).	106
Figure 2. The treatment profile for hot tensile testing of as-cast samples.	106
Figure 3. Engineering Stress-Strain curves and True Stress-Strain curves superimposed on the same plot.	109
Figure 4. Four representative fracture surfaces of the hot tensile samples from SEM fractography with the fracture surface measured by feret diameter in Fiji.	110
Figure 5. Higher magnification images of the 830°C at a strain rate of 0.1 s^{-1} (a), 1200°C at a strain rate of 0.1 s^{-1} (b), 830°C at a strain rate of 10 s^{-1} (c), 1200°C at a strain rate of 10 s^{-1} (d).....	111
Figure 6. Strain to failure versus strain rate which demonstrates the accumulation of damage at higher strain rates which is enhanced as temperature decreases.	112
Figure 7. Johnson-Cook Strength model fit to true stress-true strain data from 830°C to 1200°C with a strain rate of 0.1 s^{-1} to 10 s^{-1}	113
Figure 8. Schematic drawing of wheel rolling mill design for FEA modeling.	115
Figure 9. A cross section of the wheel assembly that shows the movement of the web rollers to induce plastic deformation in the web section of the wheel.	115

Figure 10. Schematic of wheel rolling model in Forge NxT.	116
Figure 11. Cross section of the wheel model in Forge NxT for grain size at seven seconds.	117
Figure 12. Cross section of the wheel model in Forge NxT for triaxiality stress at seven seconds.	117
Figure 13. The tonnage on the web rolls (upper and lower rolls) for the X direction.	118
Figure 14. The tonnage on the web rolls (upper and lower rolls) and the tonnage on the edging rolls (upper and lower conical rolls).	119
 SECTION	
Figure 3.1. Sampling for hot rolled specimens and testing orientation.	123
Figure 3.2. Experimental hot rolling procedures based on the isothermal rolling conditions.	124
Figure 3.3. Included in this diagram are KCU (J/cm^2) values for the TMP trials described in Figure 3.2.	124

LIST OF TABLES

SECTION	Page
Table 1.1. Composition of rail steel from Association of American Railroads (AAR) specification for rail wheels. ¹	3
Table 1.2. Composition of rail steel from Association of American Railroads (AAR) specification for rail wheels. ²¹	4
Table 1.3. Alloy compositions of American Associate of Railroads M-107/M-208 Class C and GOST 10791 Steel 2 and Steel T. ³	5
Table 1.4. Impact strength in terms of KCU (J/cm ²) at 20°C and -60°C for the rim and “disk” referring to the web section in Figure 1.1a. ³	5
Table 1.5. Alloy specifications from BS 5892 standard for C48, C56, and C64 grade steel. ⁵	7
Table 1.6. Charpy specifications for three plain carbon steels.	7
Table 2.1. Summary of the material and results by Zhang et al. ¹⁹	22
Table 2.2. The pearlitic rail steel composition by Boonsukachote et al. ²⁰	23
 PAPER I	
Table 1. Composition of the AISI 1070 as-cast steel in weight percent.....	37
Table 2. Notch toughness results and corresponding microstructural feature quantitative analysis.....	57
 PAPER II	
Table 1. Composition of the AISI 1070 as-cast steel in weight percent.....	68
Table 2. Nearest neighbor distance calculation for the particles in each porosity scan.	74
Table 3. Summary of the Aspex PICA-1020 and micro-X-Ray CT-scans results including mean diameter (μm) and volume (μm^3) x 10 ⁵	78
Table 4. Image analysis of mean diameter (μm) and mean volume (μm^3) x 10 ⁵	79

Table 5. Summary of the area fraction in ppm of NMIs in each condition in the T-L orientation.....	85
Table 6. Summary of the area fraction in ppm of NMIs in each condition in the L-S orientation.....	85
Table 7. The average inclusion compositions for classified particles averaged for the as-cast and as-rolled conditions which includes MnS, Al ₂ O ₃ , complex inclusions of MnS and Al ₂ O ₃ , mixed silicates, and CaAl ₂ O ₄	86
Table 8. Average nearest neighbor distance (μm) in each condition.	92
 PAPER III	
Table 1. Composition of the Association of American Railroads (AAR) grade steel.	106
Table 2. A summary of the tensile properties for each temperature condition under each strain rate (s ⁻¹).....	112
Table 3. Johnson Cook Parameters determined between 830°C and 1200°C at 0.1 to 10 s ⁻¹ through 10 iterative runs of a Genetic Algorithm programmed in Matlab.	113

1. INTRODUCTION

1.1. OVERVIEW

The governing standard for railway wheel specifications in the United States is the Association of American Railroads (AAR) M-107/M-208 specification.¹ Each steel class in Table 1.1 is a plain carbon steel of varied C content. Class L and A have C contents between 0.47 and 0.57 wt. % which can be classified as medium carbon steels. These grades are only used for passenger trains with low wheel loads. This can be explained by the correlation between hardness and C content with the amount of cementite (Fe_3C) increasing proportionally which induces the strength. Figure 1.1a gives a cross section of a wheel with terminology that will be used herein. The AAR M-107/M-208 standard focuses primarily on the tread hardness and specifications to ensure service durability at the rail-wheel interface as seen in Figure 1.1a with the only requirement for the web being that it should be less than 280 HB.¹ Increasing hardness and wear resistance is necessary to prevent rolling contact fatigue (RCF) at the rail-wheel interface. The resulting increase in cementite forming as pearlite and reduced proeutectoid ferrite result in reduced impact toughness for higher C rail specifications (0.57 wt. % to 0.77 wt. %). Figure 1.1b details a classic failure mode of railway wheels in heavy braking environments which includes overheating at the tread which causes both a reverse in the residual stresses at the surface and in many cases formation of martensite which makes the wheels highly susceptible to brittle failure which can cause derailing.⁴ While not solving the problem, it has been shown that increased C content in the range of 0.67 to 0.77 wt. % resulted in reduced weight losses due to the increased hardenability making

the service life of higher C steels higher than that of medium C steels.² Hardenability is also a function of C content and therefore the ability to harden the tread to induce better service conditions is a function of the C content. The increase in hardness has also been shown to increase wear resistance and fatigue properties making it valuable for heavy loading service conditions. Therefore, the standard requires Class B or C wheels for freight trains where high wheel loads with light or heavier braking conditions are expected. Typical mechanical properties for Class C and C+ steels indicating the lower (0.67 wt. % C) and higher (0.77 wt. % C) carbon contents are displayed in Table 1.2. The decrease in mechanical properties between the rim and web in Table 1.2 indicates the surface treatment performed at the tread to harden the rims which is accomplished through rim quenching to enhance local hardness and strength. While hypereutectoid steels (0.8 to 1.5 wt. % C) provide additional strength and an increase in tensile properties the formation of cementite on grain boundaries embrittles these steels and makes them highly susceptible to fracture increasing the risk of failure as in Figure 1.1b. Therefore, hypoeutectoid steels (>0.77 wt. % C) are preferred to prevent grain boundary cementite and allow some proeutectoid ferrite on grain boundaries and inclusions to maintain sufficient levels of impact toughness.

A study of forged versus cast properties was investigated by Getmanova et al³ which compared AAR M-107/M-208 Class C steel to State Standard Gosudarstvennyy Standart (GOST) 10791 steels, Steel 2, and Steel T.³ The compositions of these steel are given in Table 1.3. Steel 2 has a similar composition to AAR Class B steel with a C range of 0.55 to 0.65 wt. % and Steel T is the most similar to AAR Class C steel with a C range of 0.62 to 0.70 wt. %. Impact strength reported in J/cm² is reported in Table 1.4 for the

AAR Class C and GOST 10791 steels. Temperatures of 20°C and -60°C are examined to mimic the service conditions in Russian climates but for the North Americas 20°C and -20°C are selected due to milder overall climate. At 20°C the difference in AAR Class C impact strength and GOST Steel 2 and Steel T are both over twofold with a value of 8 J/cm² for AAR Class C steel and 20 J/cm² and 18 J/cm² for Steel 2 and Steel T respectively. The goal of the proposed work is to investigate the use of a modified wheel rolling operation on as-cast preforms to induce localized deformation in the wheel hub also referred to as the “plate” and rim to increase the impact toughness with the ultimate goal of competing with and entering the market where forged wheels are primarily used (i.e. Europe, Russia).

Table 1.1. Composition of rail steel from Association of American Railroads (AAR) specification for rail wheels.¹

Element	Ladle Analysis (%)			
	Class L	Class A	Class B	Class C
Carbon	0.47 max.	0.47–0.57	0.57–0.67	0.67–0.77
Manganese	0.60–0.90	0.60–0.90	0.60–0.90	0.60–0.90
Phosphorous	0.030 max.	0.030 max.	0.030 max.	0.030 max.
Sulfur	0.005–0.040	0.005–0.040	0.005–0.040	0.005–0.040
Silicon	0.15–1.00	0.15–1.00	0.15–1.00	0.15–1.00
Residual Elements				
Nickel	0.25 max. ^{a/}	0.25 max. ^{a/}	0.25 max. ^{a/}	0.25 max. ^{a/}
Chromium	0.25 max. ^{a/}	0.25 max. ^{a/}	0.25 max. ^{a/}	0.25 max. ^{a/}
Molybdenum	0.10 max. ^{a/}	0.10 max. ^{a/}	0.10 max. ^{a/}	0.10 max. ^{a/}
Vanadium	0.040 max. ^{a/}	0.040 max. ^{a/}	0.040 max. ^{a/}	0.040 max. ^{a/}
Copper	0.35 max.	0.35 max.	0.35 max.	0.35 max.
Aluminum	0.060 max.	0.060 max.	0.060 max.	0.060 max.
Titanium	0.03 max.	0.03 max.	0.03 max.	0.03 max.
Columbium (niobium)	0.05 max.	0.05 max.	0.05 max.	0.05 max.

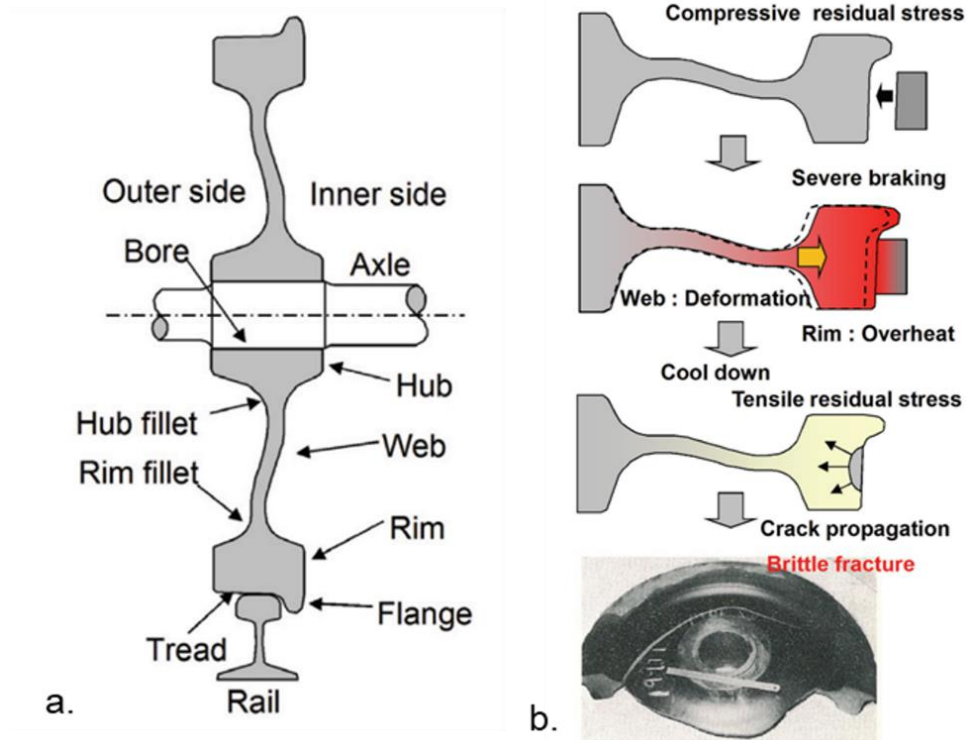


Figure 1.1. A schematic drawing of the contour of train wheels and nomenclature for relevant areas (a) and a principal failure mode of freight wheels during severe braking conditions resulting in brittle fracture (b).⁴

Table 1.2. Composition of rail steel from Association of American Railroads (AAR) specification for rail wheels.²¹

Mechanical characteristics		Class C	Class C+
Rim	HB*	350	380
	YS (MPa)	770	900
	UTS (MPa)	1220	1310
Web	YS (MPa)	470	480
	UTS (MPa)	940	990

Table 1.3. Alloy compositions of American Associate of Railroads M-107/M-208 Class C and GOST 10791 Steel 2 and Steel T.³

Specification	C	Mn	Si	V	S	P
AAR M-107/M-208: Class C	0.67-0.77	0.60-0.90	0.15-1.00	<0.040	0.005-0.040	≤0.030
GOST 10791: Steel 2	0.55-0.65	0.50-0.90	0.22-0.45	<0.10	≤0.025	≤0.030
GOST 10791: Steel T	0.62-0.70	0.50-1.00	0.22-0.65	≤0.15	0.005-0.025	≤0.030
Specification	Cr	Ni	Mo	Cu	Al	Fe
AAR M-107/M-208: Class C	≤0.25	≤0.25	≤0.10	≤0.35	<0.060	Bal
GOST 10791: Steel 2	≤0.30	≤0.30	≤0.08	≤0.30	---	Bal
GOST 10791: Steel T	≤0.30	≤0.30	≤0.08	≤0.30	---	Bal

Table 1.4. Impact strength in terms of KCU (J/cm^2) at 20°C and -60°C for the rim and “disk” referring to the web section in Figure 1.1a.³

Type of wheel	Impact strength <i>KCU</i> , J/cm^2 , at test temperature		
	+20°C	+20°C	-60°C
	rim	disk	
Cast wheel, class C	12; 12; 14	8; 8; 8	10; 9; 9
Mean	13	8	9
Forged wheel			
Steel 2	20	20	15
Steel T	18	18	15

To define the region for impact testing the English standard, BS 5892,⁵ provides a standardized approach for testing the soundness of cast wheels with specified test locations for tensile and Charpy specimens given in Figure 1.2. Three grades of steel are defined in the standard whose composition is given in Figure 1.5. Grade C48 conforms to an AAR Class L steel, grade C56 conforms to an AAR Class A steel, and grade C64 conforms to an AAR Class B steel. Because the expected average and minimums are

Table 1.5. Alloy specifications from BS 5892 standard for C48, C56, and C64 grade steel.⁵

Grade	Maximum content (wt. %)				
	C	Si	Mn	P	S
C48	0.45-0.52	0.60	0.90	0.025	0.025
C56	0.52-0.60	0.60	0.90	0.025	0.025
C64	0.60-0.67	0.60	0.90	0.025	0.025

Grade	Maximum content (wt. %)				
	Cr	Cu	Mo	Ni	V
C48	0.25	0.35	0.1	0.25	0.06
C56	0.25	0.35	0.1	0.25	0.06
C64	0.25	0.35	0.1	0.25	0.06

Grade	Maximum content (wt. %)			
	Al	Ti	Nb	Cr+Mo+Ni
C48	0.06	0.03	0.05	0.5
C56	0.06	0.03	0.05	0.5
C64	0.06	0.03	0.05	0.5

Table 1.6. Charpy specifications for three plain carbon steels. Grade C48 conforms to Association of American Railroads (AAR) Class L, Class C56 conforms to Class A, and Class C64 both conform to AAR Class B steel.⁵

Grade	K_{CU} (J/cm ²) 20°C		K_{CV} (J/cm ²) 20°C	
	Average	Minimum	Average	Minimum
C48	16	12	5	3.75
C56	16	12	5	3.75
C64	16	12	5	3.75

The first thought that may come to mind in terms of improving impact toughness would be to decrease the C content and accept the use of a Class B wheel in service instead. However, decreasing the C content decreases the hardenability which results in a drop from a range of 321-363 Brinell Hardness (HBW) to 302 to 343 HBW in the rim which would result in decreased service life and is not desirable.¹ Therefore, a process is needed to optimize the impact toughness of a Class C wheel without significant alloy re-

design, although in future work the allowance for microalloy elements in the standard will be discussed in further detail. This work takes a particular focus on the impact toughness property of this material, but tensile properties are also of critical importance to the service of railway wheels as well. The AAR M-107/M-208¹ specification gives minimum hardness values for the rim and web of the Class C wheel of 301 to 363 HBW with a requirement that the web be at least 20 HBW lower than the minimum tested value, equating to roughly 280 HBW maximum. The most common process used for railway wheels in North America, Africa, China, and India is the casting process.³ It is advantageous due to the high volume of castings which can be produced from a single heat in an Electric Arc Furnace (EAF). The steelmaking practice is important when investigating mechanical properties because inclusion type, size, morphology, and distribution influence notch toughness, ductility, and fatigue. As-cast structures can have varied properties due to section size and defects in the cast structure. By hot rolling it is possible to mitigate some of these defects such as columnar solidification resulting in large grains, porosity, and even inclusion distribution and aspect ratio although caution must be taken to prevent anisotropy. Another process which is commonly used in England and Russia is the forging production process. The feedstock for the process can be obtained from continuous casting or billet produced from an EAF or basic oxygen furnace (BOF). Therefore, the billet has similar properties to that of the cast wheels, however, the blanks for forging are also rotated 90° with the hub punched through the equiaxed region of the billet to remove any segregation band, porosity, or shrinkage defects from the forged wheel which would be harmful to final properties. In the forging process, two large industrial presses are used, typically a 9 to 10-ton and 5-ton press to

form the piece into the rough shape of the wheel. The detriment of this route is that the capital cost to install and maintain a forging line is quite high as well as added cost of additional heat treatment between subsequent forging passes. Therefore, the casting process provides a cheaper alternative with higher throughput making it desirable. European regions experience temperatures as low as -60°C in winter months and must use forged wheels with improved impact toughness to prevent catastrophic failures during service. However, even in North America there is a demand for greater service life and to further improve mechanical properties at lower costs, and this leads to one of the objectives of this project. A hybrid process that combines the cost effectiveness of near-net-shape casting with the microstructural refinement of the forging process would be of great benefit. By modifying the wheel rolling mill configuration, a cast pre-form could be subjected to final stage rolling, resulting in refinement of grain size, closure of porosity, and improvements of mechanical properties in the web and rim section. This new product could open new markets for foundries and produce greater service life. The goal of this project is therefore to determine the viability of such a process. Utilizing a combination of thermodynamic modeling, hot tensile testing, and laboratory scale hot rolling experiments the wheel rolling process is simulated. The effect of hot rolling parameters on the microstructure and Charpy V- and U-notch toughness was evaluated utilizing a combination of optical and electron microscopy. The information from experimental trials was utilized for development of a Finite Element Analysis model of the modified wheel rolling process. High temperature tensile testing at multiple strain rates was utilized to determine the Johnson-Cook Strength empirical fit. The objective is to achieve the specifications for forged products with a feasible reduction ratio of the cast material.

1.2. INDUSTRIAL PROCESS OF WHEEL FABRICATION

1.2.1. Griffin Wheel Casting Process. Prior to the advent of the Griffin casting process, train wheels were produced primarily in the following ways, chilled cast iron, green sand molding, rolled steel rings affixed on iron or steel centers, centrifugally cast-iron steel rims with iron centers, and forging processes.⁶ The Griffin Wheel Process refers to counter gravity pouring technique utilized by the Amsted Rail Company which is the largest railway wheel manufacturer in the United States. The Griffin Wheel process is different from conventional casting process such as green sand mold or no-bake castings due to the use of pressurized bottom filling that utilizes a semi-permanent graphite mold. A schematic drawing of the pressure pouring technique is shown in Figure 1.3.⁶

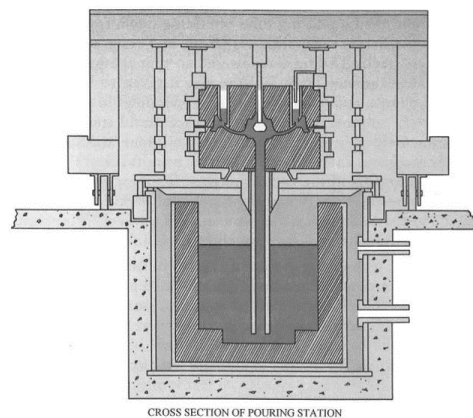


Figure 1.3. In the Griffin process, the graphite mold is positioned over the ladle and a ceramic pouring tube extends into the melt below. Positive pressure maintained over the melt forces the molten steel to fill the alumina (Al_2O_3) pouring tube and cavity.⁶

This technique revolutionized the way cast wheels were produced. The use of a permanent graphite mold which could withstand the liquid steel temperature allows for

high throughput, reducing the time and cost compared to traditional green sand or no-bake sand molding processes. The system is pressurized allowing the metal to flow at a uniform (but quick) rate into the mold. The action of bottom filling reduces the turbulence and decreases gas porosity and reoxidation defects as compared to conventional gravity filling. The rate of filling must be high due to the high thermal conductivity of the graphite, but the overall result is a cast product which is superior to other cast products. However, due to the chilling effect of the graphite mold, solidification occurs rapidly from the mold wall resulting in large thermal gradients. Without initiation sites for solidification in the matrix, columnar solidification occurs until impingement in the solidification of columnar networks from the opposite mold wall as shown in Figure 1.4a,b. During solidification the alloy becomes rich in the liquid region near the ends of secondary dendrite arms and primary dendrite arms. This is also controlled by superheat as shown in Figure 1.4c indicating the temperature range where there is a shift from columnar to equiaxed solidification.

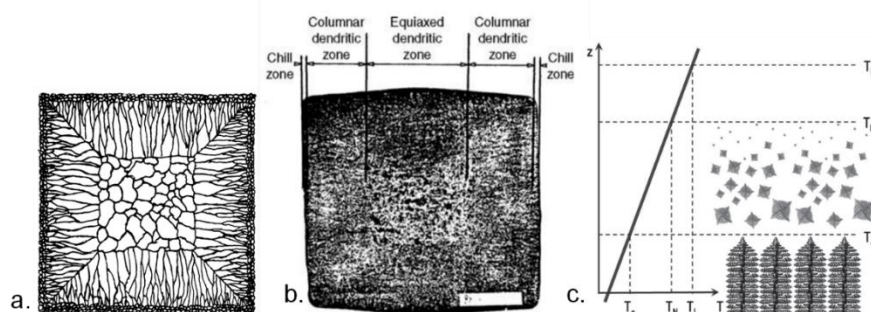


Figure 1.4. Depiction of equiaxed versus columnar solidification during billet casting. A schematic shows the transition between columnar and equiaxed solidification (a) with macroetching performed on continuously cast billet to delineate the structure (b).⁷ Lastly a diagram displays the relationship between liquidus temperature (T_L), nucleation temperature (T_N), and columnar tip temperature (T_C), illustrating the relationship between undercooling and solidification mechanism.⁸

The primary dendrites collide at the center of the sample which carries alloy elements resulting in an alloy rich region commonly referred to as centerline segregation. This can be detrimental to mechanical properties because a localized increase in alloy elements that form nonmetallic inclusions can result in higher inclusion density serving as stress concentration points during fracture. They have also been shown to nucleate cracks through decohesion known as void sheet coalescence.⁹ Inclusions of sufficient size float out during steelmaking and are removed from the slag typically composed of lime (CaO) and dolomite (MgO). While the time to tap does not allow for all inclusions to be removed the remaining inclusions are typically small enough to not significantly influence mechanical properties in the bulk casting but should be carefully monitored.

The discussion will now shift to the subsequent stages of the casting process. After casting the wheels are subsequently dished to give the web their final contour optimized for service life which is accomplished through reduction of peak stresses in the hub fillet (where the hub adjoins the web).⁴ The geometry of the cast wheel under investigation in this study is given in Figure 1.5 prior to the dishing operation. The heat treatment for wheels after being cast consists of austenitizing in a recirculating furnace at 1200°C for 2 hours, followed by spray quenching the rim region to induce local hardening in the tread, and pearlitic microstructure in the web and hub. After spray rim quenching, the wheel is then taken to another recirculating furnace for tempering which is performed at 482°C for 2 hours to reduce internal residual stresses. The wheels are then allowed to furnace cool.

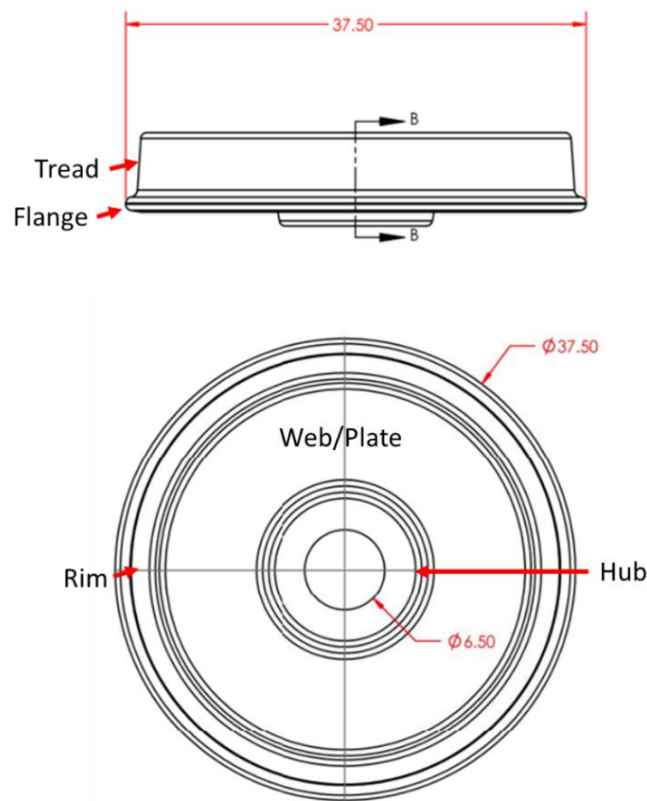


Figure 1.5. As-cast wheel geometry prior to dishing operation. This is the target specification for final dimensions in the modified wheel rolling process. Dimensions are given in inches.

1.2.2. Forging Process. As mentioned, the forging process begins with billet feedstock. The billet is sectioned into the appropriate size, heated to 1200°C, and then rotated so as to put any centerline segregation in the direction for boring the hub. The blank is then subjected to compression by the 9 to 10-ton press as shown in Figure 1.6. This process induces a large amount of plastic deformation in the material which at the temperatures of around ~1200°C is above the recrystallization temperature meaning that when the grains are sufficiently strained, dynamic recrystallization (DRX) is initiated which forms very small grains at preferential sites such as grain boundaries or grain

corners relaxing the previously strained prior austenite grain structure as shown in Figure 1.7.¹⁰

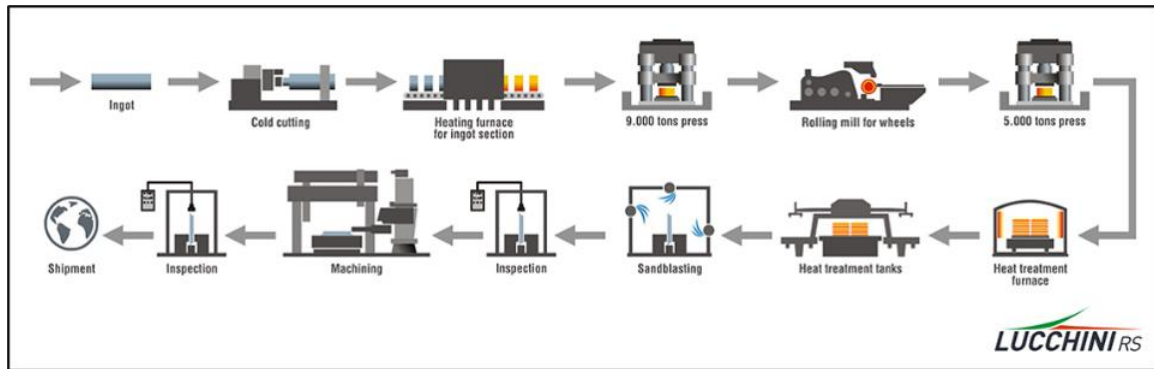


Figure 1.6. Depiction of the forging process of industrially produced railway wheels.¹²

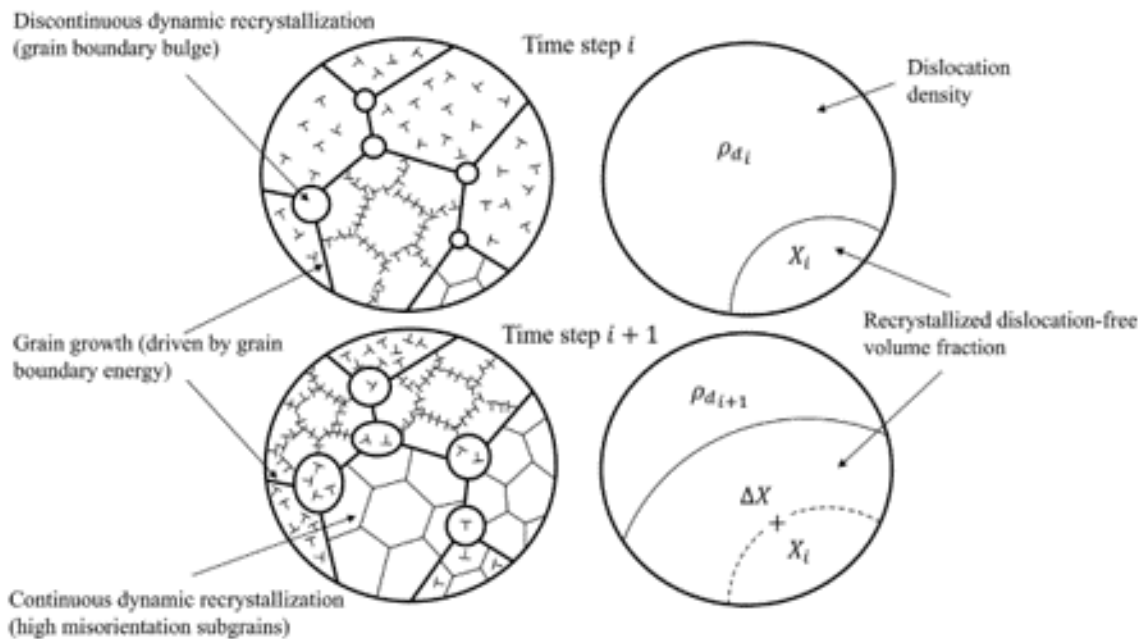


Figure 1.7. “A schematic diagram illustrating the main recrystallization mechanisms during deformation. The dislocation density decreases as the re-crystallized dislocation-free volume fraction increases over time (or strain)”.¹⁰

Static recrystallization will also take place during the reheat cycles prior to both hot rolling and the second forging process. High angle grain boundaries are formed during the reheat cycle which results in rapid growth of recrystallized grains due to the high mobility of high-angle grain boundaries.¹¹ The material is then placed in a rolling mill to reduce the rim profile slightly and expand the wheel diameter. The wheel rolling mill is a complex geometry version of a traditional ring rolling mill designed to produce large rings through uniform expansion during mild deformation. This process is repeated with a 5-ton press to get closer to the final shape and to further refine the structure prior to dishing into the final shape. In both production processes there are subsequent heat treatments and finishing operations such as peening or machining to induce compressive surface residual stresses and improve fatigue properties respectively. The benefits of the forged process come from the large plastic deformation of the billet into the wheel shape. The reduction in grain size through DRX and static recrystallization after being pressed results in a uniform and fine grain structure which is favorable for impact toughness.

One stage during the forging process is of particular interest with respect to this work. An adaption of the simple ring rolling process called wheel rolling is the operation during forging that takes place just before deformation in the 5-ton press in the flowchart in Figure 1.6. In the forged process, the wheel rolling stage induces minimal plastic deformation, primarily in the wheel rim, which induces expansion of the overall wheel diameter through use of complicated combination of web rolls, support rolls, and a back roll. This step in the forged process is primarily for shaping the wheel and is not the primary step used to induce deformation. This is due to the fact that the stages just

proceeding it, the hydraulic press, involve large amounts of plastic deformation initiating DRX which results in a fine grain structure.

Although the mechanical properties suffer as a result of the casting process when compared to the forging process, the factor of cost is quite strong when determining the best production route leading the casting process to be popular in the United States where winter temperatures are milder compared to Europe and Asia which generally use the forging process. The interest on this project, however, is to examine the potential for alterations to the conventional casting process by combining certain concepts from the forging process to mitigate the negative microstructural features of the cast wheels. The hydraulic presses are both expensive and require feedstock of billet which do are not conducive for implementation in the casting process and were therefore not the target of investigation. As discussed above, the wheel rolling process works with material which is fairly close to the final specifications with minor adjustments to the rim profile and increases the overall diameter of the material. To improve material performance of the cast product, inducing more plastic deformation during the wheel rolling process on locally important regions of the wheel on a cast pre-form slightly larger thickness may allow for mitigation of the detrimental effects of the cast microstructure.

2. LITERATURE REVIEW

2.1. INFLUENCE OF MICROSTRUCTURE ON MECHANICAL PROPERTIES OF EUTECTOID STEELS

This section is broken into three primary sections. To begin the influence of microstructure on the mechanical properties of steel castings will be examined to detail the specific microstructural features pertinent to influencing impact toughness and tensile properties. Next, the effect of forging on microstructure and mechanical properties will be discussed to detail the methods used to influence the microstructure in a way that leads to improved impact toughness and the mechanisms by which the microstructure is influenced. Lastly, the influence of inclusions and porosity on impact toughness will be explained to identify defects in cast products which influence toughness and the literature regarding deformation and these features.

2.1.1. Influence of Microstructure on the Mechanical Properties of Steel

Castings. The plain carbon steel used in commercial processing of railway steels is a low alloy high C steel with a content of 0.71% C shown in Figure 2.1. In the Fe-C phase diagram this steel is hypoeutectoid which means that the equilibrium microstructure is composed of free ferrite, or proeutectoid ferrite and a lamellar pearlite which forms from a cementite thin film, meaning the ferrite lamellae initiate first followed by C lean and C rich areas causing continued driving force for cementite and ferrite lamellae formation.

After the wheels are subjected to heat treatment, they are allowed to cool to room temperature at a slow cooling rate through furnace cooling to transform to the equilibrium microstructure consisting of primarily pearlite with a small amount of proeutectoid ferrite. The proeutectoid ferrite content forms on preferential nucleation

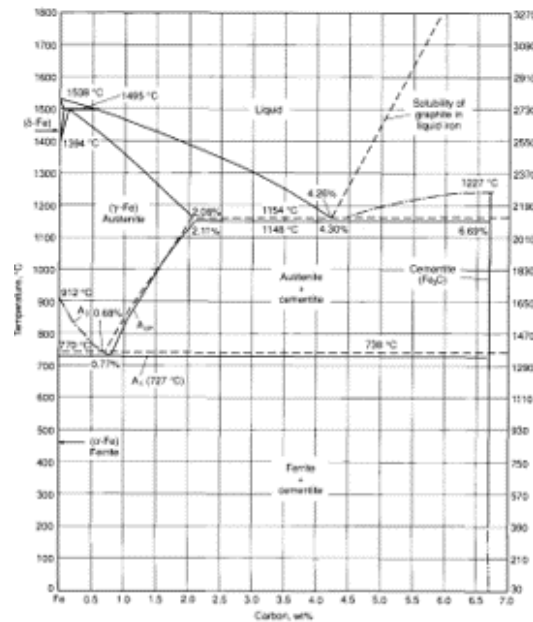


Figure 2.1. The Fe-C phase diagram which shows that the eutectoid composition is 0.8 % C. Therefore, this steel is a hypoeutectoid.¹³

sites which include prior austenite grain boundaries and nonmetallic inclusions, particularly manganese sulfide (MnS) due to the Mn lean region surrounding them in the metal matrix. The alloy composition also includes small amounts of various alloy elements including Mn, Mo, Cr, Ni, Si, and Cu. High C along with all alloys listed promote higher hardenability with Mn, Cr, and Mo being used most commonly for this purpose.¹⁴ This relationship is further illustrated in Figure 2.2. This diagram indicates the depth of hardening for a steel of the same C content is a function of the alloy. This explains the rim quench performed during the heat treatment process of cast wheels. Localized hardness is induced, and the inclusion of Mn, Cr, and Mo allow for higher hardenability allowing for a robust wheel tread that can withstand rolling contact fatigue (RCF) which has been shown to be a critical factor for predicting railway steel life in the

literature.^{14,15} However, as shown this does result in a hardness gradient which is associated with changes in the microstructure.

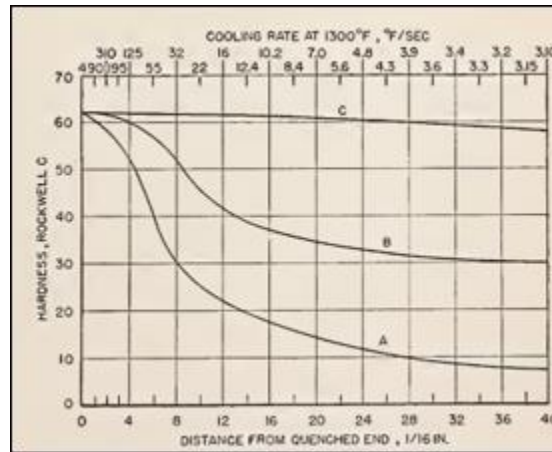


Figure 2.2. Standard end-quench (Jominy) test displaying the relationship between C and alloy additions on the relationship with hardenability with peak hardness being controlled by C content.¹⁴

2.1.2. Effect of Forging on Microstructure and Mechanical Properties. The following work is to explain the primary microstructural parameters which dictate fracture behavior in high carbon steels. Importantly this will be distinguished for hypoeutectoid, eutectoid, and hypereutectoid steels. While the expectation from the Fe-C binary phase diagram that AAR Class C material is strictly hypo-eutectoid there are minor shifts in the eutectoid point as a function of alloy additions. Therefore, it is necessary to describe each system to prevent design complications especially considering the upper limit for C content of the AAR Class C wheel is 0.77% C which could behave in a different manner than a 0.67% C steel depending on the alloy concentration. Historically there have been some disagreements in literature stemming from specifying the exact parameters which effect impact toughness. As mentioned previously it is well

established in the literature that pearlite interlamellar spacing (ILS) and PAG size influence hypoeutectoid, eutectoid, and hypereutectoid steel strength with pearlite interlamellar spacing highly contributing to the yield strength which is controlled by the cementite (Fe_3C) phase in the lamellae.¹⁵⁻¹⁷ The relationship between yield strength (YS) and pearlite ILS has been shown to follow the Hall-Petch relationship by multiple literature sources as shown in Figure 2.3.^{15,17} It has also been shown that both PAG size and proeutectoid ferrite content play significant roles in impact toughness.^{8,9}

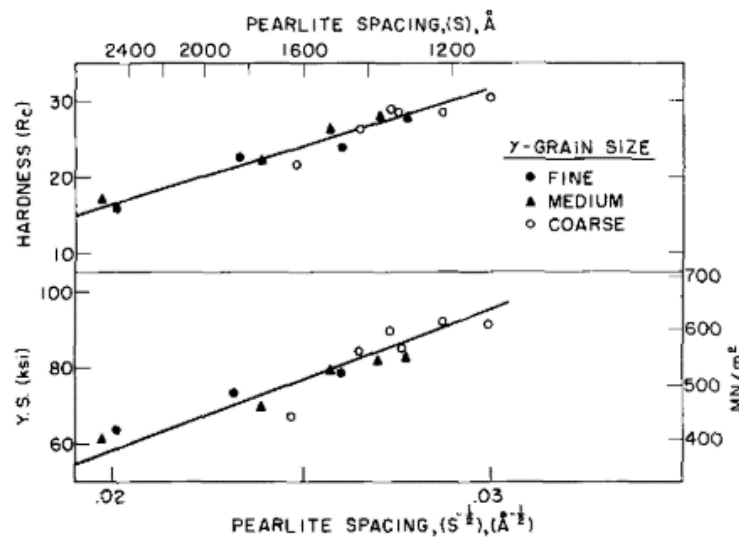


Figure 2.3. Hyzak & Bernstein demonstrated that the yield strength and hardness of pearlitic steels follow a Hall-Petch relationship.¹⁵

Hyzak & Bernstein¹⁵ established that PAG size was the primary factor influencing impact toughness for a C – 0.81 wt. %, Mn - 0.87 wt. %, P – 0.018 wt. %, S – 0.013 wt. %, and Si – 0.17 wt. % alloy showing that pearlite colony size did not vary with different austenitization temperatures (800°C to 1200°C) and times as well as salt pot tempering (550°C to 675°C). This was shown in full ductile to brittle transition temperature (DBTT)

curves, indicating the shift in the curves as a function of grain size and explaining the change in impact toughness with reduced grain size. Since this study other authors have found more evidence to support the notion that pearlite colony size plays a more critical role in fracture initiation than previously thought with differences being observed in hypoeutectoid, eutectoid, and hypereutectoid steels which likely cause the confusion in literature in the first place. Work by Zhang and Gu¹⁸ clarified the relationship between pearlite colony size and impact toughness for plain carbon steels of varied C content. Summarized in Table 2.1, varied austenitization temperature resulted in varied PAG size but the impact energy and pearlite colony size are observed to remain constant in each condition. The impact toughness is seen increasing at 1300°C with slightly decreased colony size. A study was performed to determine the mechanism for this relationship by holding isothermally at 550°C in a salt pot for 5, 10, 15, and 20 seconds and quenching afterwards to preserve the structure during nucleation of pearlite. The results showed that for an increased grain size the tendency for nucleation sites within the grain increases with particles such as NMI serving as points that reduce the energy barrier for nucleation. This result is in line with the results of Hyzak and Bernstein¹⁵ with respect to pearlite colony size although the proposed mechanism for impact toughness is conflicting. However, the authors stated that previous researchers have shown that in hypo and hypereutectoid steels that grain size does have an effect on pearlite colony size and is therefore not austenitization temperature independent which validates the approach taken in this study to reduce grain size for improvements in impact toughness through hot rolling for the hypoeutectoid steel being investigated.

Table 2.1. Summary of the material and results by Zhang et al.¹⁹

	C	Si	Mn	P	Cr	Fe
	0.810	0.180	0.840	0.014	0.272	Bal.

Austenitizing Temperature/°C	Prior Austenite Grain Diameter/μm	Pearlite Colony Diameter/μm	Interlamellar Spacing/μm	Impact Energy/J	Yield Strength/MPa	Tensile Strength/MPa
880	43.39 ± 3	6.11 ± 0.4	0.1548	10 ± 0.5	743	1154
950	61.29 ± 5	5.85 ± 0.5	0.1357	10 ± 1	704	1091
1020	80.14 ± 8	6.04 ± 0.7	0.1310	11 ± 1	702	1086
1100	102.75 ± 10	6.10 ± 0.4	0.1341	10 ± 1	650	1005
1200	142.48 ± 15	5.79 ± 0.5	0.1188	11 ± 0.5	626	976
1300	227.26 ± 25	5.67 ± 0.4	0.1326	12 ± 1	611	959

Thus far the discussion has been for eutectoid steels, however there is literature involving C contents within the specification for the Class C specification, Boonsukachote et al²⁰ modeled the mechanical properties of a pearlitic rail steel with the following composition (Table 2.2). Charpy specimens were prepared for testing at room temperature, however a V-notch orientation was observed which does not follow the specification for the BS 58921 for testing at 20°C which is pertinent to our corporate sponsor. The impact toughness obtained for this material was 13.11 J, however, once converted the K_{CV} has a value of 16.25 J/cm². Diener & Ghidini²¹ reporting values of ~10 J for AAR Class C+ (~0.77% C) indicating KCU of 20 J/cm² which is in line with the values reported by Getmanova et al³ for forged products insinuating that it is possible to obtain forged toughness in cast AAR Class C steel. They also indicated that AAR Class C steel has a tendency to spall and crack during service. These values are also not given with respect to microstructure or treatment but are expected to be as-cast.

Table 2.2. The pearlitic rail steel composition by Boonsukachote et al.²⁰

Steel	C	Si	Mn	P	S	Cr	Ni
Grade 900A	0.747	0.298	0.782	0.021	0.015	0.026	0.005

2.1.3. Role of Inclusions and Porosity on Impact Toughness. Along with the equilibrium phases in the microstructure during cooling of the specimens, it is also important to examine the effects of steel cleanliness on mechanical properties. Work performed by Tanaka et al.²² nicely described the formation kinetics and preferential morphology of formation of MnS during solidification using in-situ High Temperature Confocal Scanning Laser Microscope (HTCSLM).²² The formation has also been simulated kinetically by Shu et al.²³ They detailed three cases of formation, including primary MnS formation, formation at oxide inclusions, or MnS crystallization in solid steel. It has been shown that a large number of alumina (Al_2O_3) inclusions can act as nucleation sites for MnS during solidification.²⁴ This has also been shown to produce Mn lean regions surrounding the complex formed inclusion of MnS and Al_2O_3 that can initiate the formation of α -ferrite during solid state cooling.²⁵ MnS inclusions are not well bonded with the metal matrix and can serve as stress concentration sites, forming micro voids during deformation.⁹ Therefore, MnS inclusions can decrease impact toughness, fatigue properties, and lead to failure of components. However, they are necessary for a number of reasons. The primary two are that MnS inclusions increase machinability of steels by acting as self-lubricant during machining and, more importantly, it prevents the preferential formation of FeS inclusions which form on grain boundaries causing hot shortness in Fe-S steels without Mn which causes wheels to be scrapped.¹⁸ The issue is also complicated by the introduction of hot rolling to the metal matrix. Nonmetallic

inclusions can either be brittle or deformable in typical hot rolling windows (900-1200°C). Brittle compounds may fragment during hot rolling which are very detrimental to material properties while deformable inclusions such as MnS can elongate along the rolling orientation leading to anisotropy in the transverse orientation with respect to the rolling direction.²⁶ It is desirable to keep type and amount of inclusions at a minimum for improved mechanical properties.²⁶ Some authors have detailed the effects of overall inclusion content on mechanical properties for different systems. However, understanding the effects within specific materials are still up to individual researchers. It is common for routine automated analyses such as those performed in this body of work to examine overall steel cleanliness and is performed quarterly in an industrially setting as a part of the AAR specifications according to ASTM E1245.²⁷ However, some new technologies have been shown to limit the elongation of inclusions such as MnS inclusions through the addition of rare earth alloy or Ca to reduce the plastic nature of these inclusions at hot rolling temperatures.^{28,29} It is also important to take the deoxidation practice into consideration which at Griffin Wheel includes fully killed steel meaning that Mn, Si, Al are used to deoxidize to greatly reduce the overall dissolved O content of the steel in the final casting. The resulting inclusions are MnS, Al₂O₃, and complex inclusions of Al₂O₃ with MnS shells and trace amounts of mixed silicates of Mn and Al, and calcium aluminates (CaAl₂O₄). Sulfide morphology in the as-cast structure is strongly tied to the deoxidation practice and can result in Type I, Type II, Type III, or Type IV morphology. Because the dissolved O content (~30 ppm) and residual Al content (~20 ppm) are both low the preferred MnS morphology is Type II which

corresponds to fine intergranular chains on grain boundaries as shown in Figure 2.4. This has been shown to be detrimental for impact toughness.⁹

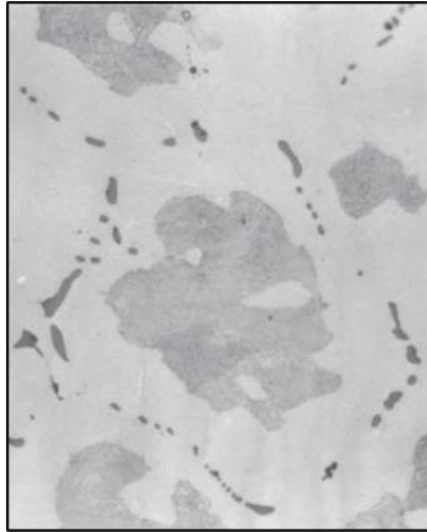


Figure 2.4. An example of Type II MnS sulfide formation in an as-cast 0.25 wt. % C steel.³⁰

Along with nonmetallic inclusions, voids may also form through trapped O and N content in the steel which results in points of nucleation for cracking lowering impact toughness. Although the described deoxidation practice results in a very low O content which correlates to low porosity content, solidification shrinkage can also be responsible for void nucleation during casting which can be detrimental for impact toughness.

Solidification shrinkage is caused by inadequate feeding during solidification (Figure 2.5b) while porosity or microporosity are caused by gas evolution (Figure 2.5a).³¹ A study was performed for AAR Yokes for railway freight cars by Sarkar et al³² which absorbs impact loading during service, the purpose to investigate the root cause of a batch of castings with particularly low impact toughness of 12-16 J at -40°C as compared to the

AAR requirement of 27 J at -40°C . The alloy in question is a 0.3 wt. % C steel explaining the impact toughness requirement. Fractography analysis of the fracture surfaces indicated that the gas porosity of the batch with low toughness had a particularly high amount of gas porosity as a result of the casting process. Porosity acts as a stress raiser during crack propagation and therefore decreases the resistance to crack propagation as shown in Figure 2.6.³²

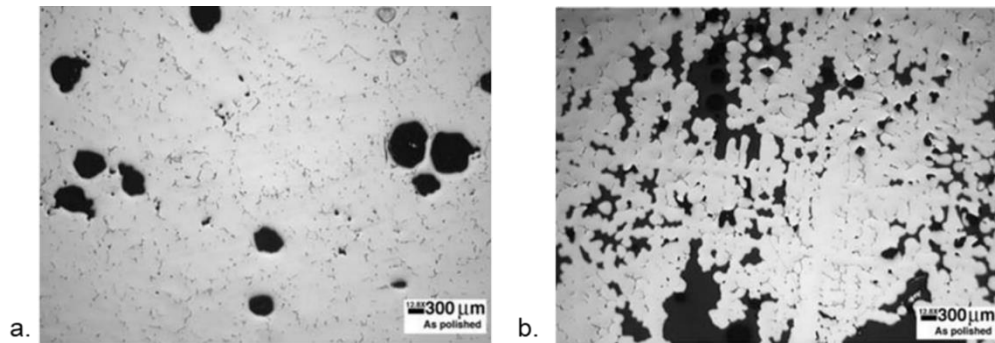


Figure 2.5. Unpolished images showing example of gas porosity (a) and shrinkage porosity (b) in an AA 5182 remelt secondary ingot.³¹

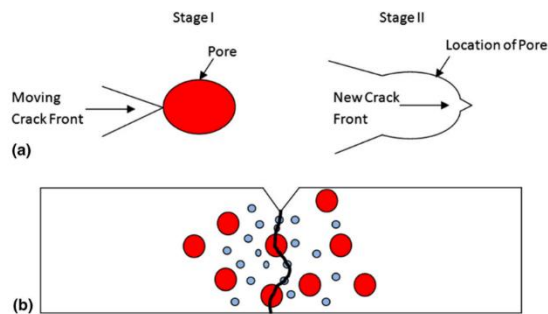


Figure 2.6. A drawing outlining the effects of gas porosity on fracture during impact testing. The pore acts as a stress raiser (a) and the crack path follows porosity as it provides an energy preferential path for failure that results in decreased impact toughness (b).³²

2.2. MODELING THE INDUSTRIAL RING ROLLING PROCESS

Industrial wheel rolling is a geometrically complex version of a simple ring rolling operation as shown in Figure 2.7.³³ It is conventionally a part of the forging process for train wheel production as mentioned previously taking place in between the forge press stages of the production process. The typical blank shape prior to rolling and then after wheel rolling depicted in Figure 2.8.³⁴ The traditional wheel rolling process as modeled by Shen et al³⁵ defined the total rim reduction as 3.6 mm with expansion of the wheel being 54 mm. The modified wheel rolling process to be simulated in this project involves intentional displacement of 33.3 mm in the web to induce increased deformation to promote grain refinement in the web and improve impact toughness.

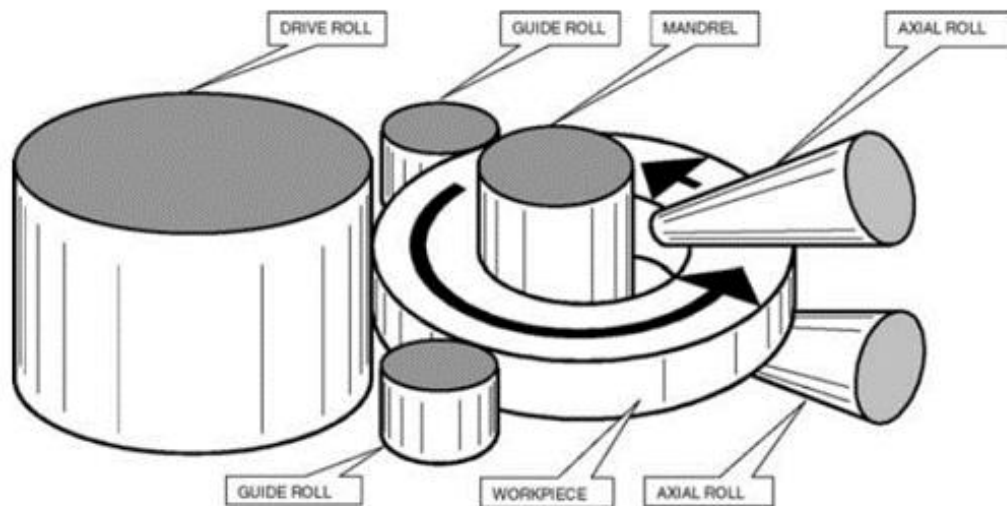


Figure 2.7. A schematic drawing of the ring rolling process including the mandrel and drive roll which are driven and induce the deformation of the ring and the expansion and the guide roll and axial rolls which guide the expansion.³³



Figure 2.8. Schematic diagram indicating the wheel blank shape prior to wheel rolling, and after wheel rolling. The main difference being a slight reduction in the rim thickness and an elongation in the plate with a slight reduction in web thickness.³⁴

2.2.1. Experimental Modeling of the Ring Rolling Process. In traditional wheel rolling processes the application of plane strain hot rolling would not be appropriate, but because of the similarity in the web roller interaction with the web and traditional hot rolling it is an appropriate comparison. By completing plane strain hot rolling at similar rolling pressures and cumulative percent reductions and determining the response of different rolling parameters on impact toughness it is possible to predict the behavior of the web material during the wheel rolling process. The Johnson-Cook Strength model for plastic behavior has also been shown to be highly effective at determining material behavior for a variety of hot working industrial problems. To begin, the Johnson-Cook Strength model has been used to model simple hot to produce a 3D FEM for plane strain hot rolling of a variety of carbon steels by Buchely et al³⁶ which effectively predicts the rolling pressures exerted on the rollers, Von Mises stress, equivalent plastic strain, and strain rates of the plate during hot rolling in the temperature range of 900°C to 1200°C. The use of the Johnson-Cook Strength model can be applied from 1D problems such as this to more complicated industrial problems such as modeling wheel rolling.

2.2.2. Finite Element Analysis Modeling of the Ring Rolling Process. Wheel rolling, a more complicated form of ring rolling for complex geometry products, is the forging process of railway wheels resulting in large increases in the overall diameter of the wheel while rim profile is also formed gradually.³⁵ Figure 2.9 depicts a schematic drawing of the components involved in the wheel rolling process. The guide rolls, centering rolls, and edging rolls all act to stabilize the wheel in the vertical rolling configuration and contour the rim profile.³⁵ The web roll and back roll are driven, and therefore induce deformation and expansion of the material. The wheel is deformed by the web roll and the material expands in overall diameter in all directions away from the back roll which along with the pressure exerted from the web rolls induces the motion of expansion. The centering rolls to displace to allow the expansion and the edging rolls guide the wheel through the expansion. Because of the complex motion and the dependence on material flow behavior, the problem of modeling the process of wheel rolling is fairly difficult and has been observed by a host of different researchers.

Along with elements of simple ring rolling, the process of wheel rolling also has attributes of multi-pass asynchronous rolling and complicated interactions of rollers and the wheel.³⁵ A few different mathematical systems have been used to attempt to simulate this process, starting with more simplified 2D simplification but resulted in oversimplifications which prevented the process from being modeled efficiently for industrial application.^{37,38} For 3D modeling which is more attractive for industrial application, the two methods Lagrangian FE and Euler FE have been examined individually but both result in inefficient simulations either due to high density meshes or inaccuracy with determining evolving geometry respectively.³⁹ Therefore, combining

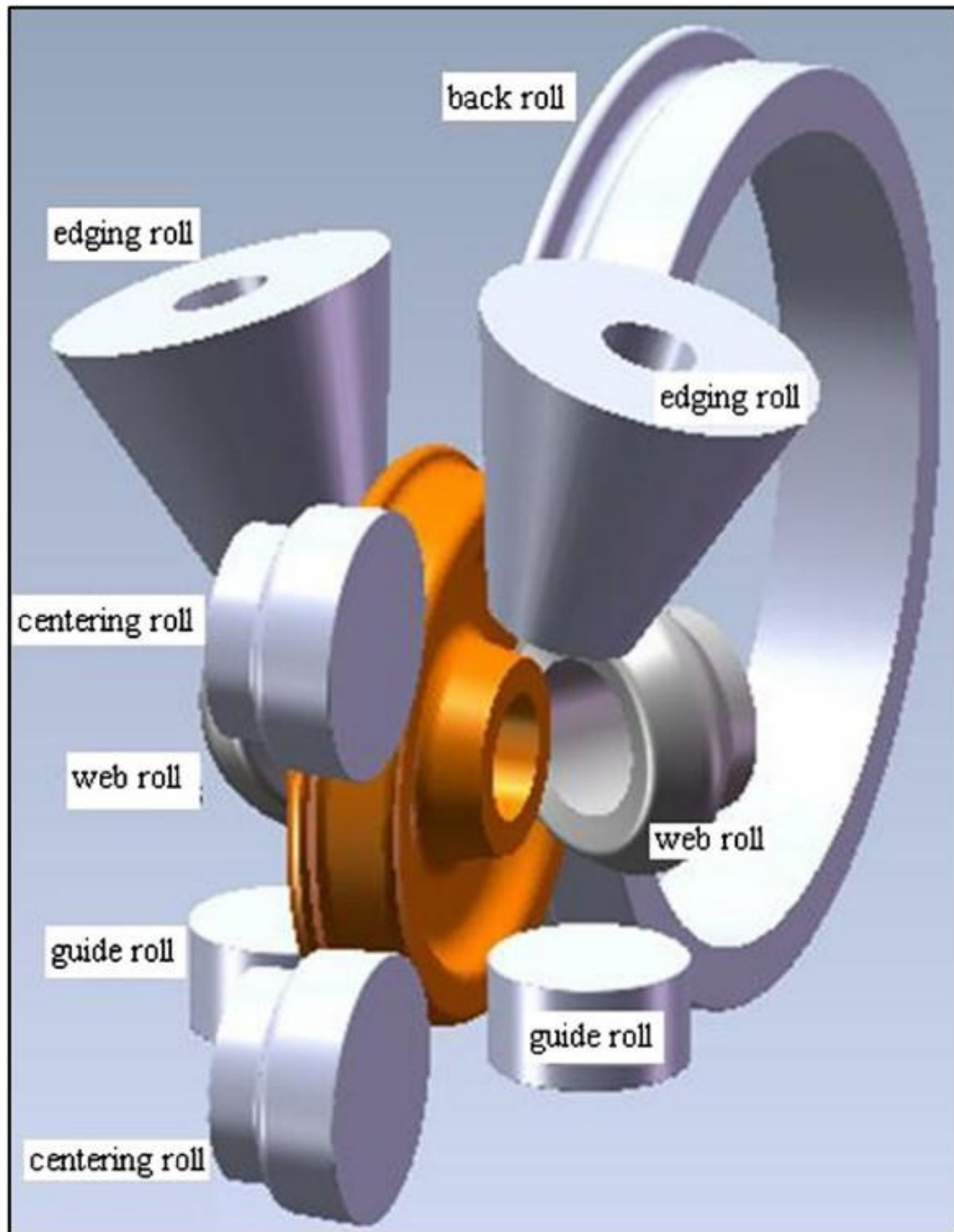


Figure 2.9. Schematic illustration of a vertical wheel mill.³⁵

Lagrangian and Euler in a randomized fashion, also known as arbitrary Lagrangian-Euler (ALE) method is considered the most effective technique and is employed in most

simulation packages. Davey and Ward³⁹ made use of this technique to mesh wheels during wheel rolling with non-uniform meshing which allows for more complex meshing in regions effected by the web roll and back roll and simpler meshing during the expansion which is dependent more on material flow behavior. The results of their work were that they were able to predict flow in the radial and axial direction and ring growth with high accuracy for application to complex industrial applications including traditional wheel rolling.³⁹

While there have been extensive studies conducted to optimize the mill itself and stabilize the wheel during simulation there are issues applying these concepts directly to this particular work.³⁶⁻⁴⁰ With the use of ALE, the ability to simulate industrial ring rolling operations has become more accessible and a number of software packages such as Simufact Forging, ABAQUS, and FORGE are used industrially to tackle these problems. The difficulty in applying the concepts from previous literature to this work involves the differences in the process with that of traditional wheel rolling as performed in the forging process. The wheel rolling operation in the traditional forged process is primarily concerned with increasing the wheel diameter after forge pressing the rough shape as well as finishing the rim profile. By taking a cast product and inducing localized deformation through the wheel rolling operation, the intended result is a new problem compared to that in literature. The goal of the work performed is to use an industrial software, knowledge from literature and objectives from the corporate sponsor to create a simulation for the cast pre-form wheel rolling process with minimal engineering trial and error.

PAPER**I. EVALUATION OF NOTCH TOUGHNESS AFTER SIMULATED RING-ROLLING OF AISI 1070 STEEL WHEEL CASTINGS**

Jacob M. Summers, Laura N. Bartlett, Ronald J. O'Malley, Mario F. Buchely, Richard Pilon

Department of Metallurgical Engineering, Missouri University of Science and Technology, Rolla, MO 65409

ABSTRACT

The goal of this work is to compare the mechanical properties of AISI 1070 grade steel castings during a simulated ring-rolling process. Multiple markets require minimum levels of notch toughness in their specifications as measured by impact strengths. Ring rolling of near net shape castings can improve location specific properties by mitigating centerline segregation, closing porosity, and reducing grain size without the use of expensive forging operations. Using a pilot scale rolling mill, cast pre-forms were subjected to a 66% cumulative reduction and were subjected to Charpy impact testing with standard V and U-notch impact tests at -20°C and 20°C, respectively. By correlating microstructure and notch toughness post rolling, a thermomechanical process can be developed for industrial application. The microstructure was evaluated by optical and scanning electron microscopy. It was shown that prior austenite grain size and proeutectoid ferrite content both heavily influenced notch toughness in AISI 1070 steel.

Furthermore, lower temperatures for hot rolling resulted in finer grain size, which led to increased notch toughness.

1. INTRODUCTION

As-cast AISI 1070 grade steel is a high carbon steel that is composed of an equilibrium microstructure of primarily pearlite with small amounts of free ferrite. The ferrite forms between the A1 and A3 temperatures on prior austenite grain boundaries (PAGB) or on inclusions during cooling. AISI 1070 is used extensively for railroad applications, including cast and forged wheels. Industrial ring rolling operations are typically the final stage in the wheel forging process before dishing, which narrows the dimensional tolerances of an as-forged product. Forgings are preferred for some wheel applications, however, the cost and energy consumption are significant for forging of billet. Near net shape cast products are attractive due to their lower cost and production efficiency. Issues with cast products when compared to forged products relate to the final microstructure. Centerline segregation and porosity occurs during dendritic solidification of castings, and this can be detrimental to notch toughness.¹ The goal of the following work is to investigate the use of ring rolling operations on cast near net shape products to induce localized deformation to improve mechanical properties at specific locations and at a lower cost than forging.

Along with high amounts of alloy segregation, it is also known that prior austenite grain size (PAG size) is also large in cast products.² This is an important consideration because the deformation in the forged process results in recrystallization and a fine,

equiaxed grain size, which is typically correlated with increased notch toughness. AISI 1070 grade steel has a high C content (~0.70 wt. %) and this results in higher strength and hardness and lower notch toughness and ductility, which is attributed to pearlitic cementite (Fe₃C) in the microstructure.^{3,4,5,6} Hyzak and Bernstein and Elwazri et. al. have shown conclusively that the distance between adjacent cementite plates, also known as pearlite interlamellar spacing (ILS), follows a Hall-Petch type relationship with strength and hardness in pearlitic steels.^{3,5} The Hall-Petch relationship is defined by the Equation (1):

$$\sigma_y = \sigma_i + k_y S^{-\frac{1}{2}} \quad (1)$$

The increase in yield strength, σ_y is related to the intrinsic yield stress, (σ_i), and the pearlite interlamellar spacing (S). K is a material constant which is related to grain boundary hardening.^{3,5} Some authors have also shown experimentally that PAG size plays a minor role in tensile properties but is a point of conflict in literature as Karlsson and Linden concluded that pearlite ILS is the primary contributing factor to tensile properties.^{3,7}

In circumstances where high wear resistance is desired such as for automotive, railroad, and agricultural industries, this material is desirable. Increased strength has been shown to reduce weight loss during service of parts and this has been found to result from a fine pearlite ILS, on the order of 60 nanometers.⁹ The influences of microstructure in eutectoid steels on toughness involve more conflict in literature. The primary features in question are PAG size, pearlite nodule size (collections of pearlite colonies), pearlite colony size, and proeutectoid ferrite for the equilibrium microstructure. Hyzak & Bernstein concluded that PAG size primarily influences toughness through a shift in the

shelf energy, which indicates a change in the transition temperature, with pearlite colony size having a secondary impact at best.³ However, they did not investigate the pearlite nodule size or proeutectoid ferrite effects. Zeng et al showed that for a given PAG size that proeutectoid ferrite content could be varied through alloy design to influence toughness.⁴ Pearlite nodule size has not been extensively correlated in literature to toughness but work by Elwazri et al showed the influence of PAG size and transformation temperature on pearlite nodule size and correlated the results to tensile properties.⁵ Since the pearlite transformation initiates from PAGB and grows until impinging on other pearlite nodules, it makes sense that PAG size and pearlite nodule size are proportional. Further study is needed to conclusively compare pearlite nodule size and toughness but general relationships between PAG size and pearlite nodule size can be examined qualitatively. It is also supported in literature that strength and toughness in hypoeutectoid and eutectoid steels are decoupled and can be influenced independently through careful heat treatment. For example, cooling rate after processing strongly affects pearlite ILS while the grain size can be influenced during processing through either heat treatment as shown by Hyzak and Bernstein and Gladman et. al or in this case of this work by deformation processing.^{3,4,5,7,10} Correlations have been made between reduced PAG size and larger pearlite ILS, but this has not been thoroughly tested, which conflicts with the notion of fully decoupled mechanical properties.^{3,4,5} The relationship between toughness and microstructure in hypoeutectoid and eutectoid steels in literature has been shown to be strongly tied to PAG size and proeutectoid ferrite content. The relationship between toughness and heat treatment are fairly well understood

from the literature but the relationship between toughness and deformation processing for hypoeutectoid steels to optimize mechanical properties is not as well documented.

The goal of the present work is to simulate industrial ring-rolling process using experimental hot rolling with the intent of refining the PAG size and increasing the proeutectoid ferrite content to improve toughness of AISI 1070 steel. An understanding of the effect of hot deformation at isothermal rolling conditions will aid in developing a thermomechanical process controlled route that can be implemented during ring rolling processing of industrial castings. In this study, the effect of hot rolling at isothermal temperatures of 830 to 1200°C on the microstructure and mechanical properties of an as-cast AISI 1070 wheel casting was investigated to determine process parameters for future ring rolling operations.

2. DESIGN OF EXPERIMENTS

A steel heat with a target chemistry conforming to AISI 1070 was melted using the electric arc furnace, EAF, process in a commercial foundry. The steel was Mn-Si killed and the resulting melt was transferred to a ladle. The steel was cast into semi-permanent graphite molds using pressure pouring technology. The graphite molds were specifically machined to generate thicker section sizes than what is done in production, thus generating a near-net-shape preform that could be forged into final shape. Figure 1 shows a quarter section of the as-cast preform. Characterization of the as-cast steel was performed by optical emission spectroscopy (OES) for primary alloy elements. An average of 10 measurements are depicted in Table 1. Carbon (C) and sulfur (S) were

measured by LECO combustometric analysis and are also depicted in Table 1.

Macroetching was performed to observe the dendritic growth and observe the degree of segregation in the cross-section of the casting. The sample was surface ground (80 grit zirconia) and then subjected to a 1:1 ratio of 37% HCl to H₂O bath was used to macroetch the surface which included a bath of 700 mL of HCl, and 700 mL of H₂O held at 60°C for 15 minutes. Centerline segregation was observed which will be discussed in further detail in the next section. To simulate the ring rolling process, a STANAT rolling mill was utilized to hot roll rectangular specimens (43.5× 55×100 mm) which were sectioned to include the centerline segregation, schematically shown in Figure 1.

Table 1. Composition of the AISI 1070 as-cast steel in weight percent.

C*	Si	Mn	Cu	Cr	Mo	Ni	P	S*	Nb	Ti	Fe
0.706	0.53	0.73	0.168	0.130	0.025	0.048	0.004	0.021	0.004	0.0008	Bal.

*Concentrations of sulfur and carbon were determined utilizing LECO combustometric analysis

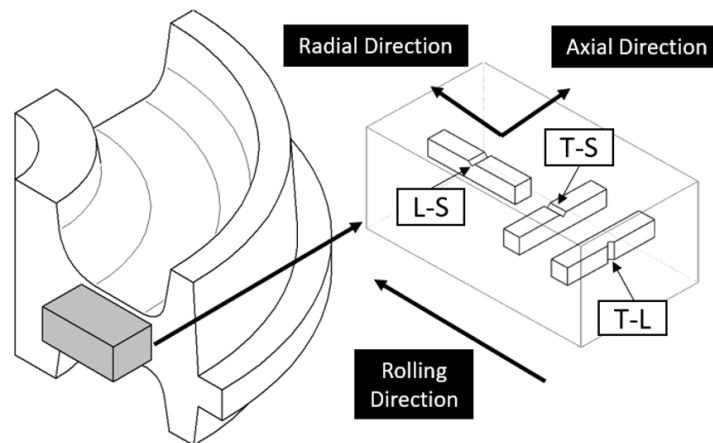


Figure 1. Sectioning methodology adopted for rolling samples as well as Charpy testing orientations used for as-cast and as-rolled material for comparison.

To examine the effect of hot rolling on toughness at the varied isothermal soak temperatures, many variables were held constant to ensure they would not affect the results. The treatment profile is shown schematically in Figure 2.

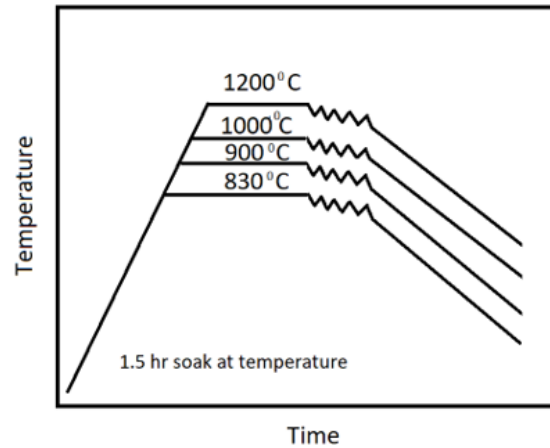


Figure 2. The steel casting was soaked in an electric box furnace with SiC elements for 1.5 hours at the process temperature before hot rolling and subsequent slow cooling ($\sim 0.1\text{s}^{-1}$) in a refractory blanket.

The isothermal temperatures selected were identified based on the austenite phase field for AISI 1070 steel. Using JMatPro, the equilibrium phases were determined versus temperature as shown in Figure 3. To safely hot roll above the A3 temperature, the lowest rolling temperature was determined to be 830°C, which is approximately 50°C above the A3 temperature. An upper limit rolling temperature of 1200°C was selected to be well below the melting point and still simulate common commercial rolling/forging temperatures. The initial thickness of the samples was held constant (43.5 mm) so that the pass schedule was held consistent between trials at a given temperature, and the starting volume of each sample was within 5% of each other. The percent reduction per pass was

between 5 and 25% for all samples. Each sample was subjected to a 66% cumulative reduction or 3:1 reduction ratio resulting in a final thickness of ~14.5 mm after ~8 passes with 5 minute reheat cycles. Mechanical test specimens were machined from the center of the as-rolled specimens which allowed removal of any decarburization layer. Standard ASTM E23 Charpy V and U notch specimens were extracted from the as-cast material from the centerline segregation and from the centerline of the as-rolled material.

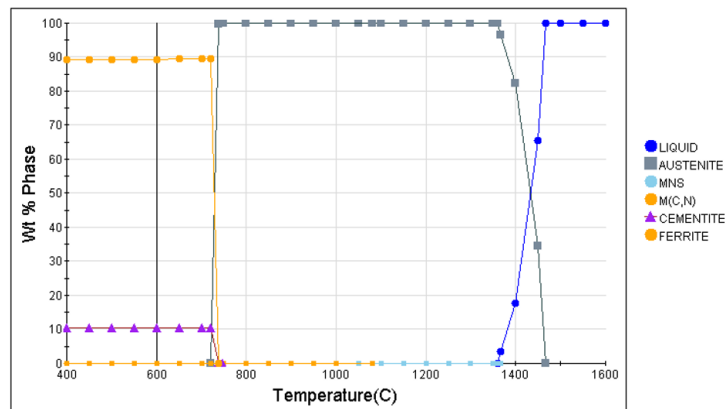


Figure 3. Phase transformations during equilibrium solidification and cooling as predicted for AISI 1070 steel in JMatPro.

Figure 1 also shows schematically different orientations sectioned from the blocks, and they were labeled L-S, T-S and T-L samples in accordance with the longitudinal and transverse conventions and notch orientations.⁸ The authors understand the S-T orientation is conventionally tested but limited material delays its evaluation until a future investigation. Charpy specimens were prepared using a Blacks Charpy CNM Machine. Specimens were then notched in a Blacks Charpy CNB. The notch depths were evaluated using an optical microscope to validate the notch requirements. V-notch

specimens were tested at -20°C and U-notch specimens were tested at 20°C . A Tinius Olson Pendulum Model 84 Impact Tester was used for Charpy testing. Fracture toughness values were recorded, the samples were collected, and rinsed with water with the surface being subsequently coated with ethanol and dried to preserve the fracture surfaces for SEM analysis. A slow saw with coolant was then used to remove the fracture surface which was preserved for SEM fractography. A specimen was then prepared in the plane directly below the fracture surface for a direct comparison of the fracture surface to a flat polished and etched specimen.

Scanning electron microscope (SEM) via Tescan Vega3 was utilized using an accelerating voltage of 20 kV. Secondary electron (SE) imaging was used to show the features of the fracture surface although backscatter electron mode was investigated to examine the contours in the fractured surfaces and subsequent EDS was performed on flat polished surfaces to investigate the inclusion composition.

For optical observation, specimens were etched with 4% Picral at room temperature to reveal the microstructure of pearlite and proeutectoid ferrite. Microstructural features such as PAG size and proeutectoid ferrite content were quantified. To reveal PAG size, the material was solution treated for 1.5 hours and then quenched in water and tempered at 470°C for 8 hours. This allowed the P and other tramp elements to diffuse to the PAGB.^{11,12,13} Material was then sectioned and metallographically prepared. 50 mL of saturated aqueous picric acid solution (premixed with wetting agent) with 6 pipette drops of HCl (0.3 mL) was heated to 70°C and used as an etchant to reveal the PAGB. The proeutectoid ferrite content was measured at different locations in the microstructure using ImageJ. By investigating samples, two samples per

chemistry in the same orientation and average of 10 random locations were used to report proeutectoid ferrite content for the as-rolled samples.

3. RESULTS AND DISCUSSION

The results of macroetching of the cross section of the casting is depicted in Figure 4a which shows the columnar structure of the section as dendritic solidification which occurred from the outer walls of the casting. Notable centerline segregation was observed in the center of the casting which would indicate a locally high solute content. Quantitative measurements of chemical segregation were obtained utilizing OES as a function of position as shown in Figure 4b. Figure 5a-f shows the average compositions of alloying elements and impurities as a function of depth from the top surface. The results of this analysis verified that the dark etching region in the center of the casting was indeed centerline segregation, which shows an increase in Mn, Si, P, Cr, and S in the center of the casting. The alloying percentage increase displayed on the graph represents percent difference calculations between the outside and centerline and shows a notable increase in these elements. All elements were determined by OES, but only major alloy elements are depicted in Figure 5a-f. Importantly, the Mn and S content increase in the segregation region which correlates to increased nonmetallic inclusions, particularly MnS. Carbon is not included as it tends to have lower accuracy during OES readings but would be expected to have a similar trend. While this is true of sulfur as well, it was important to report due to the effect on inclusions in the material.

Sections from the wheel casting were prepared and hot rolled as described in Figures 1 and 2 to include the centerline segregation band. Specimens for metallography and mechanical properties were prepared from the centerline segregation area of the casting for comparison to the as-rolled condition.

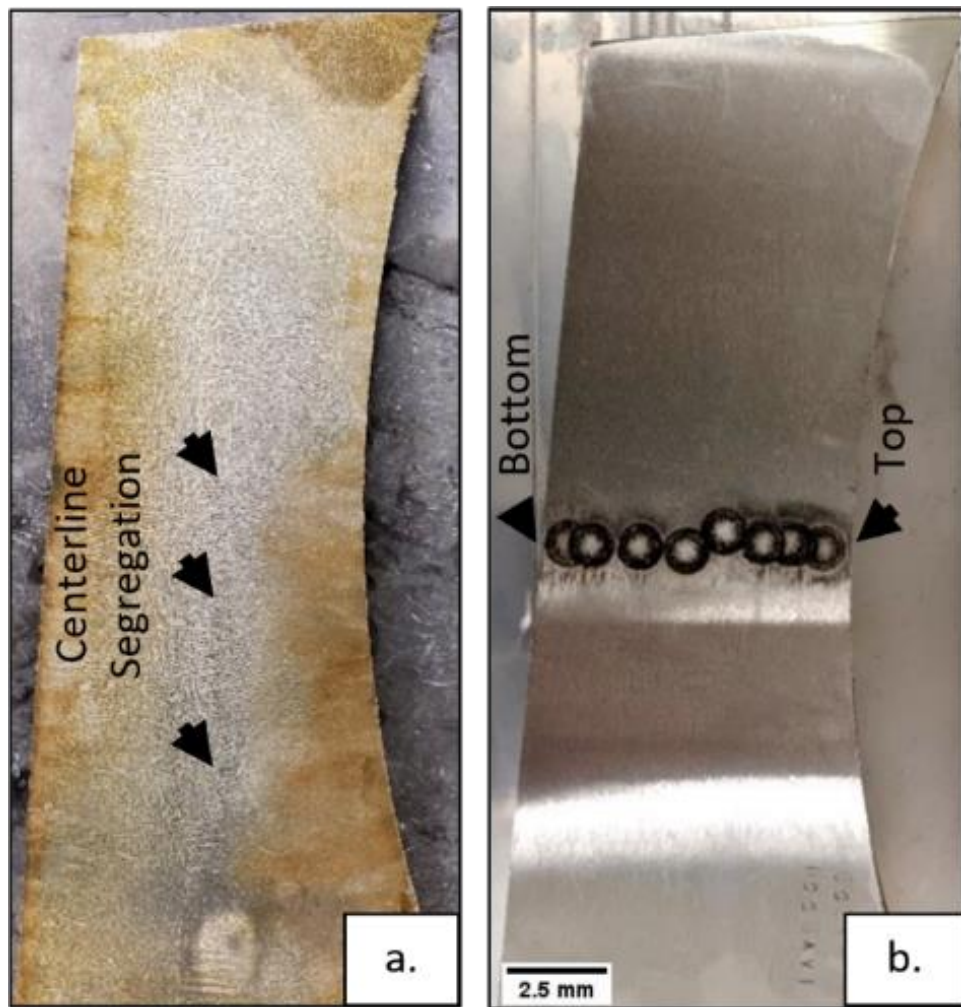


Figure 4. (a) Macroetch showing segregation in the web section of the wheel casting as shown in Figure 1. (b) Quantitative chemistry measurements at locations through the thickness of the casting.

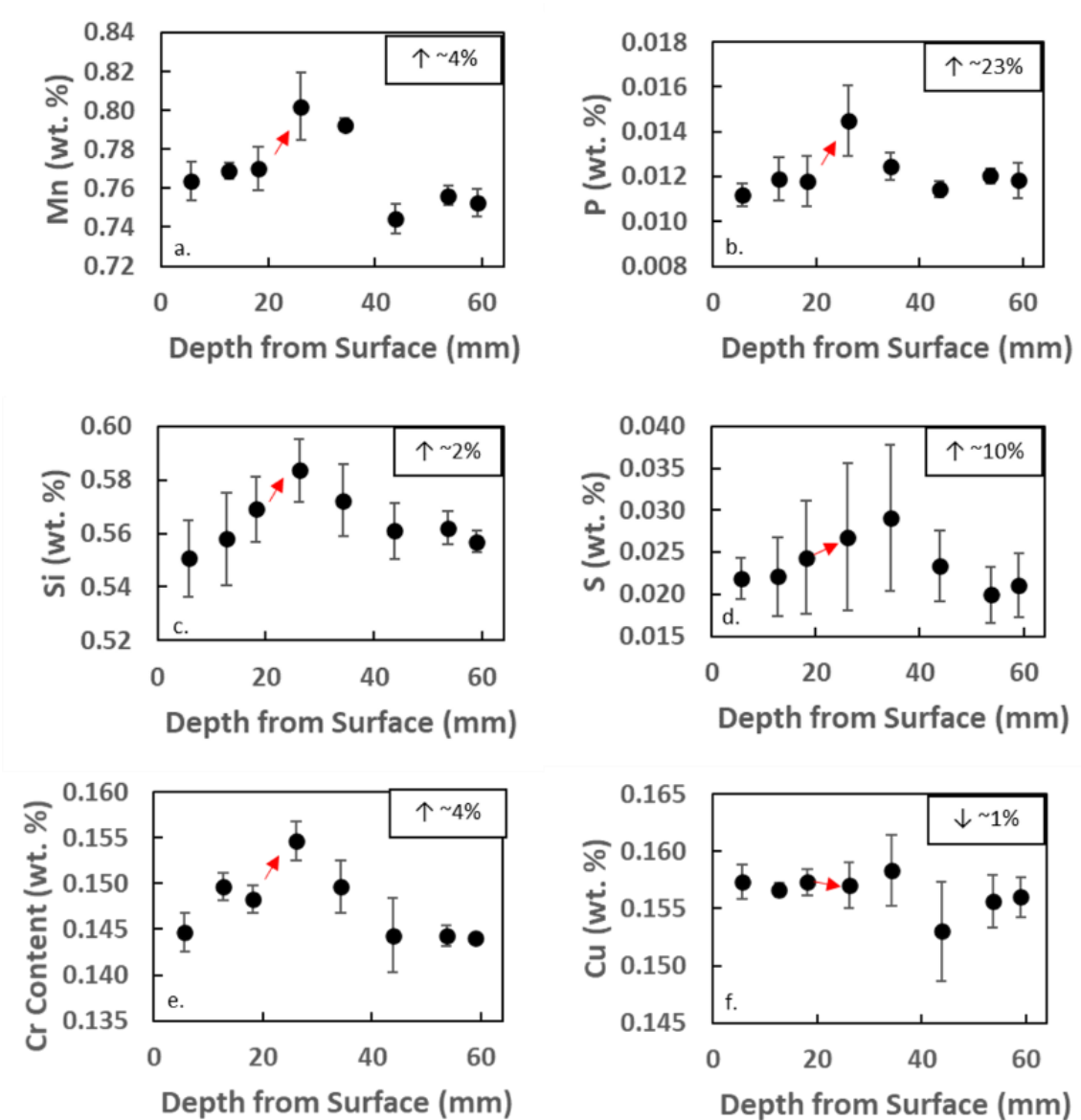


Figure 5. Increases in the alloying elements and impurities are observed at the casting center line (red arrow), confirming centerline segregation. Cu is the only alloy element which is not segregated based on the OES results. The exact regions of observation are depicted in Figure 4b where “0” mm depth represents the top surface. Alloy partitioning can result in locally higher concentration of inclusions which can be detrimental to fracture toughness.

The grain size was measured for each isothermal condition. ImageJ was utilized to measure at least 80 grains per specimen and the average diameter in microns is

reported in Figure 6a. As shown in Figure 6a, increasing the isothermal rolling temperature generally increased PAG size. While the material experiences static and dynamic recrystallization and healing during rolling and interpass stages, recovery and grain growth compete with those mechanisms at higher temperatures thus preventing fine grains at higher temperatures at the same equivalent cumulative reduction. To verify the validity of these results, histograms of the PAG size for each isothermal rolling temperature are shown in Figure 6b-e against a normal distribution for each condition which was calculated based on the mean, standard sample deviation, and bin size used in the plot (separated based on ASTM Grain Size Number). Comparing the results of the grain size measurements to the normal distributions at 830°C (Figure 6b), 900°C (Figure 6c), and 1200°C (Figure 6e), the data appear to be skewed. This may be attributed to the small sample size. Optical imaging was performed in the L-S orientation of the as-cast and as-rolled samples for comparison of the microstructure. In Figure 7, high and low magnification image are included that represent the as-cast structure in the centerline segregation region.

Optical imaging was performed in the L-S orientation of the as-cast and as-rolled samples for comparison of the microstructure. In Figure 7, high and low magnification image are included that represent the as-cast structure in the centerline segregation region. The microstructure is composed primarily of pearlite with only trace amounts of free ferrite. Present at both magnifications are notable sized porosity in the material. In the higher magnification image (Figure 7b), the porosity length is over 50 μm which can be detrimental to impact properties, as it serves as a large discontinuity that can nucleate crack formation and subsequent propagation.

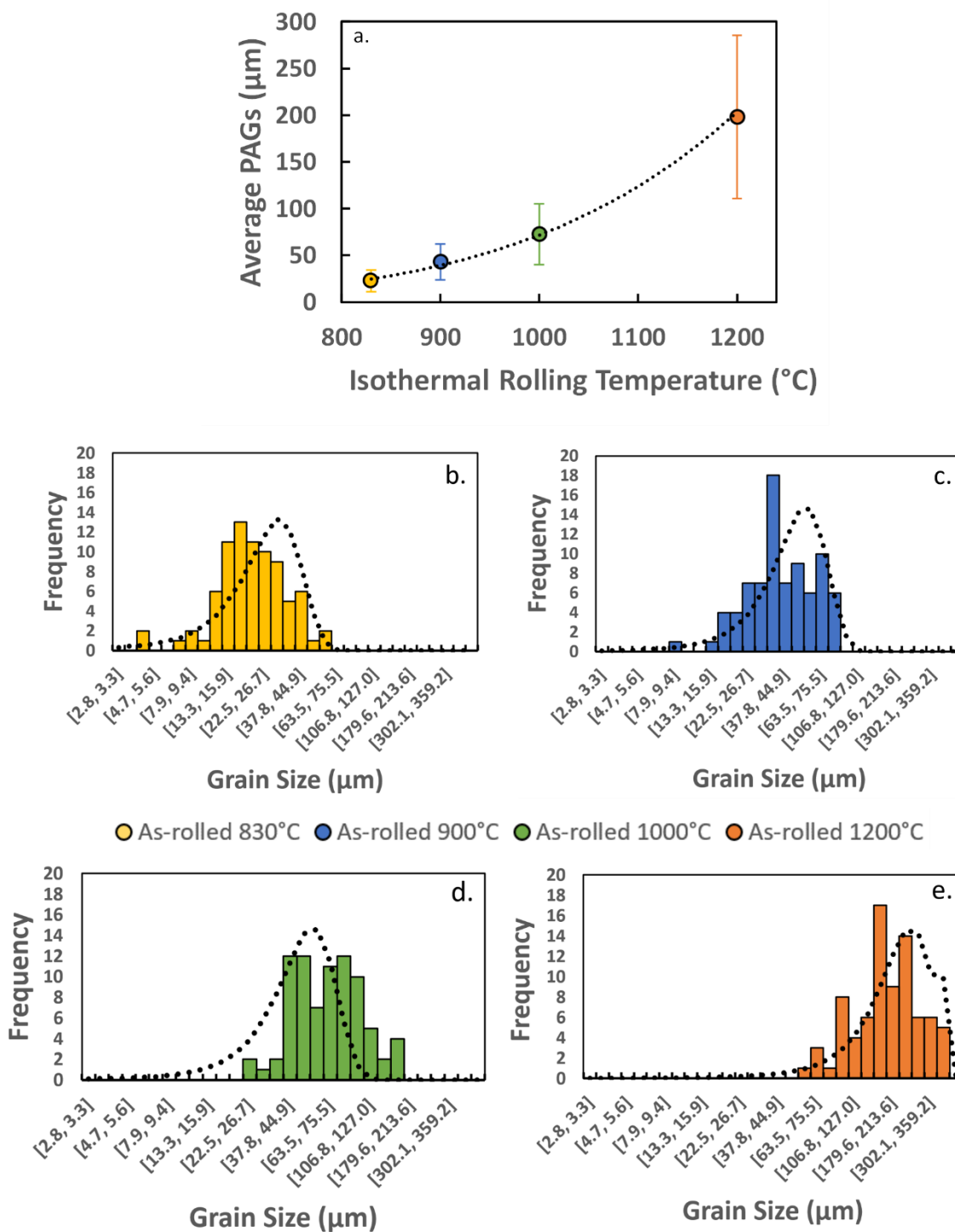


Figure 6. Average PAG size vs. isothermal rolling temperature is depicted with the standard sample deviation (a). Histograms per isothermal rolling temperatures at 830 $^{\circ}\text{C}$ (b), 900 $^{\circ}\text{C}$ (c), 1000 $^{\circ}\text{C}$ (d), and 1200 $^{\circ}\text{C}$ (e). The normal distributions were calculated based on the mean, deviation, and bin size, and is not cumulative and are plotted as the black dotted line in each figure.

From the as-cast microstructure in 7a, it can be seen that the microstructure is fairly coarse. While most pearlite nodules are fairly difficult to resolve optically, some orientations etch preferentially to others revealing the pearlite nodule labelled as “N” in Figure 7a.^{5,18} As mentioned previously, it has been shown in literature that the pearlite nodule size is a function of the PAG size because the transformation of austenite to pearlite originates on the PAGB and grows until impingement on other nodules.⁵

In Figure 8, the as-rolled microstructures are compared for each isothermal condition in the L-S orientation. In comparison to the pearlite nodule size in the as-cast condition in Figure 7a, the pearlite nodule size for all as-rolled conditions is much finer which indicates a decrease in the PAG size. Hot rolling was successful at closing the as-cast porosity as shown in Figure 8 and 9. The as-rolled pearlite nodule size is larger with an isothermal rolling temperature of 1200°C (Figure 8d) as compared to the specimen rolled at 830°C (Figure 8a). In Figure 9, the higher magnification images of each isothermal rolling condition reveal a mixture of fine and coarse pearlite combined with various amounts of proeutectoid ferrite, PF, on PAGB. An example of PF is shown for the specimen that was rolled at 1200°C (Figure 9d). The amount of proeutectoid ferrite at 830°C (Figure 9a) and 900°C (Figure 9b) appears to be higher than that of 1200°C rolled specimen (Figure 9d), and this may be correlated to a larger PAG size with higher rolling temperatures and thus a decreased amount of nucleation sites for ferrite and pearlite. After rolling at 1000°C (Figure 9c), it is evident that nonmetallic inclusions also serve as nucleation sites for ferrite. Because cementite is a hard and brittle phase, the percentage of proeutectoid ferrite in the matrix has been shown to correlate with higher fracture toughness due to crack tip “blunting” and ductile tearing instead of brittle

cleavage fracture when precipitated on PAGB. This is represented in each isothermal rolling condition but highlighted at 1200°C (Figure 9d).

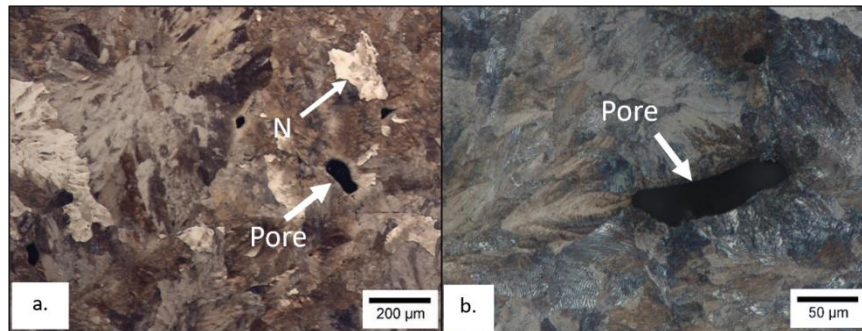


Figure 7. Optical micrograph of the as-cast material which represents the longitudinal orientation and is sectioned from centerline segregation region of the casting as depicted in Figure 4a. A coarse-grained structure of fine pearlite with inclusions and porosity can be observed.

Charpy V and U notch toughness results are presented in Figure 10 as a function of rolling temperature and orientation. The L-S orientation is examined in Figure 10a and shows the largest increase in toughness between as-cast and hot rolled specimens which can be attributed to the effect of hot rolling on the microstructure. In Figure 10b, the T-S orientation shows that hot rolling has little effect in this orientation. While the toughness values are typically higher than that of the as-cast material even in this orientation there is an observable decrease between the L-S and this orientation. When examining the T-L orientation in Figure 10c this relationship is reinforced as there is little difference in toughness between the rolled conditions and as-cast condition. The anisotropy in the hot

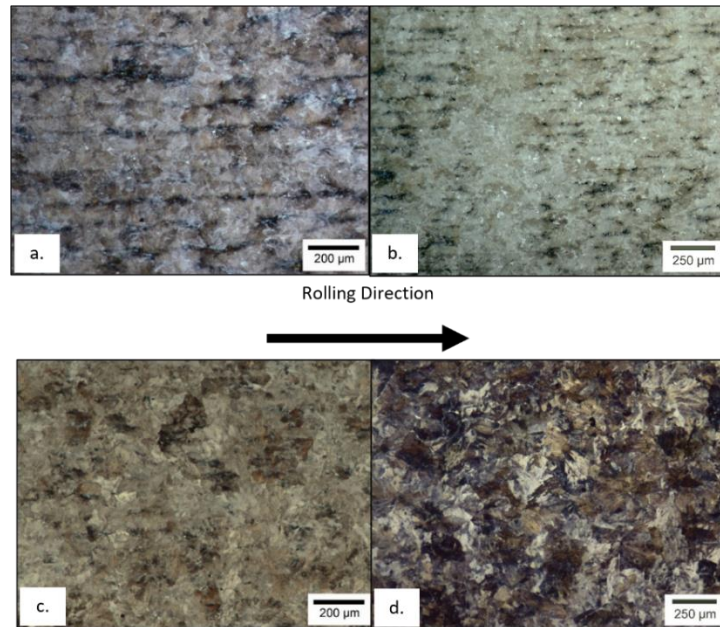


Figure 8. Optical micrographs of as-rolled specimens in the longitudinal orientation showing mainly a microstructure of pearlite. (a) as-rolled 830°C (b) as-rolled 900°C (c) as-rolled 1000°C and (d) as-rolled 1000°C.

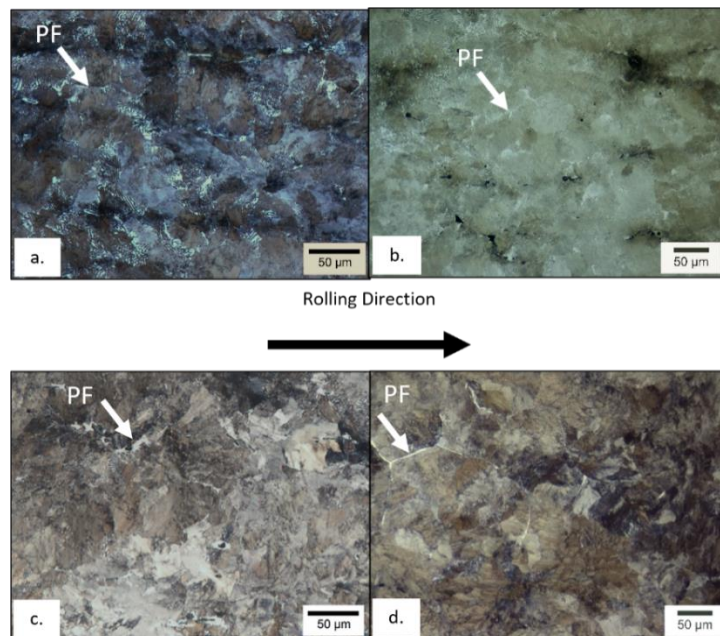


Figure 9. Optical micrographs of as-rolled specimens in the longitudinal orientation showing mainly a microstructure of pearlite with some proeutectoid ferrite, PF. (a) as-rolled 830°C (b) as-rolled 900°C (c) as-rolled 1000°C and (d) as-rolled 1000°C.

rolled material can be attributed to a few factors. One of the most common effects that causes anisotropy is preferred crystallographic orientation or texture.¹⁴ Toughness generally increases with a decrease in the grain size because during failure, the crack must constantly reorientate as it propagates through grains of different texture. The pancaking of austenite grains during uni-axial rolling promotes elongated grains of the same texture in the longitudinal orientation making the crack path less torturous. Along with elongated grains of the same texture, nonmetallic inclusions can also be elongated in the rolling direction which can also be deleterious to toughness.^{16,17} In the L-S orientation, the crack path is perpendicular to elongated grains and inclusion stringer networks. Lower toughness is expected in the T-L and T-S orientations as crack propagation along stringer networks produces either a debonding effect or a brittle fracture.

Fractographs of the as-cast fracture surface are presented in Figure 11. Samples tested at room temperature showed only a slight increase in breaking energy as well as the same fracture mode as compared with specimens tested at -20°C and were selected for comparison of different rolling conditions on the fracture characteristics. The fracture surface of the as-cast specimen (Figure 11a) shows the brittle and, transgranular cleavage fracture facets. Brittle fracture in pearlitic steels are known to occur even at room temperature.¹⁸⁻²²

Miller et al. explored fracture in carbon steels and proposed that fracture in pearlitic steel is initiated by shear cracking in cementite plates followed by tearing of adjoining ferrite lamellae producing transgranular cleavage fracture.²³ Because the

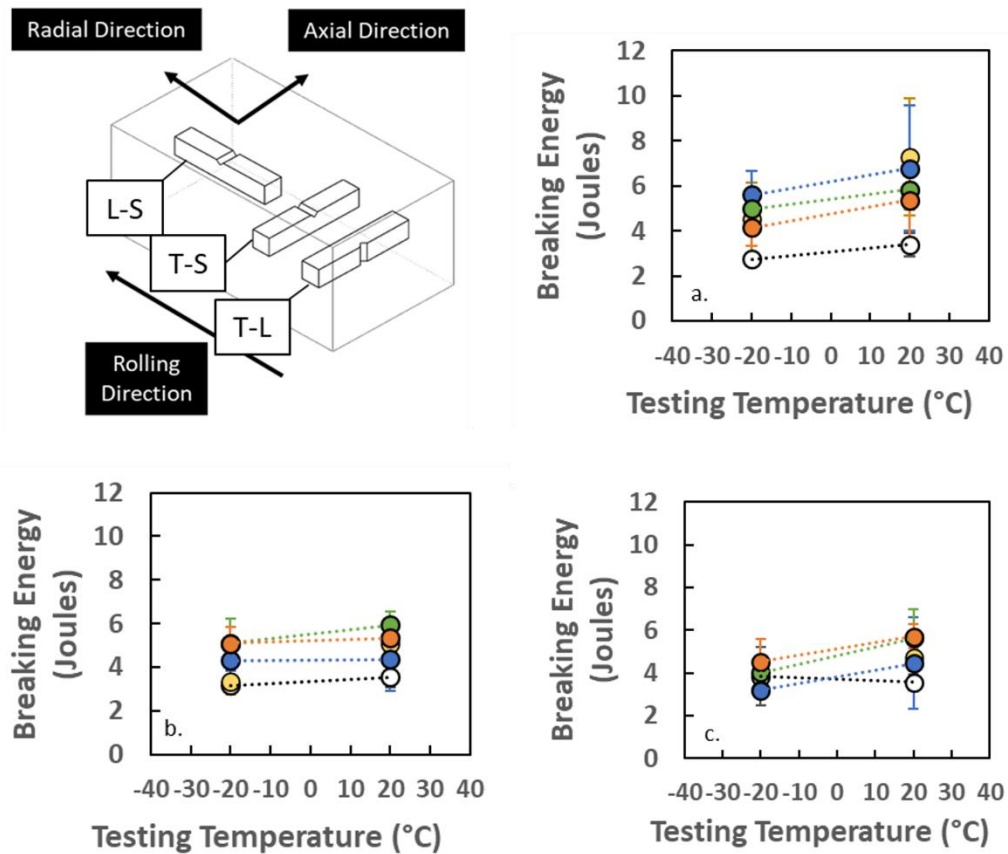


Figure 10. Charpy V- and U-notch impact results at -20°C and 20°C , respectively and in different orientations with the rolling direction (a) L-S orientation, (b) T-S orientation, and (c) T-L orientation.

material is slightly hypoeutectoid, the ferrite content which preferentially forms on PAGB, exists in the fracture surfaces as “DT” or ductile tearing ridges. The “F” in the image refers to the cleavage facet which is a unit of fracture along the lowest-packing-density plane and reorients as it reaches the next facet.²⁴ The image in Figure 11b illustrates a few additional features which may influence the fracture including porosity and MnS inclusions. The optical imaging of the porosity in the as-cast specimen shows that the pores are quite large in comparison to the as-rolled fracture surfaces, and this can cause localized fracture initiation and lower toughness.

In Figure 12a-d the as-rolled fracture surfaces are displayed for comparison. After hot rolling, the specimens still behave in a brittle fashion with transgranular cleavage fracture but when comparing isothermal rolling temperatures of 830°C (Figure 12a) and 1200°C (Figure 12d), differences in the cleavage facet size are observed. The size of facets as well as the amount of fracture crack re-orientation at 830°C is higher than 1200°C which can be correlated to the grain sizes in Figure 6a. The reduction in facet size correlates to a difference in pearlite nodule size in Figure 9a and 9d and the quantifiable difference in PAG size of an average of 198 μm at 1200°C and 23 μm at 830°C. Quantifiable differences in cleavage facet size are difficult to attain due to the nature of imaging 3D surfaces in 2D but comparison of Figure 12a and Figure 12b or the 830°C and 900°C rolled specimens, respectively, seem to have very little difference in cleavage facet size.

Therefore, the quantitative measurement of grain size is necessary to differentiate the conditions which show a slightly higher average grain size at 900°C of 43 μm and 22 μm at 830°C. The proeutectoid ferrite contents in the samples appear to correlate to ductile tearing regions that are present in each isothermal rolling condition. Unfortunately, the area fraction of ductile fracture cannot be quantified from fractography. The proeutectoid ferrite content was instead quantified using optical metallography. Figure 13 shows a flat and etched metallographic specimen that was prepared directly below the fracture surface and observed in the SEM with the surfaces oriented the same as the fracture surfaces presented in Figure 11 for the as-cast sample in the L-S orientation with an impact energy of 2.8 J.

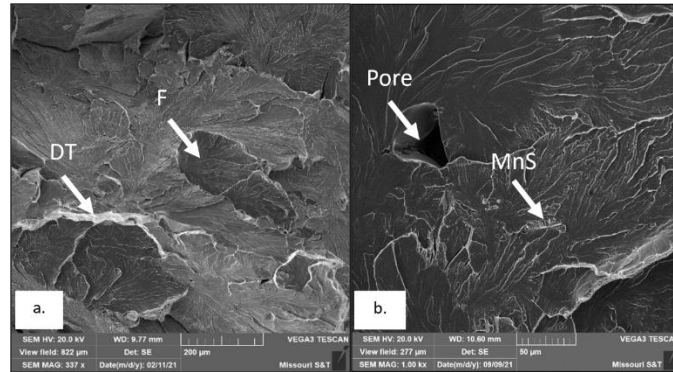


Figure 11. SEM fractography of fracture surfaces of the as-cast material (BE=2.8 J). (a) “F” shows an example of a cleavage facet and “DT” refers to isolated areas of ductile tearing. (b) Porosity and MnS inclusions were shown to produce local fracture initiation in the as-cast material.

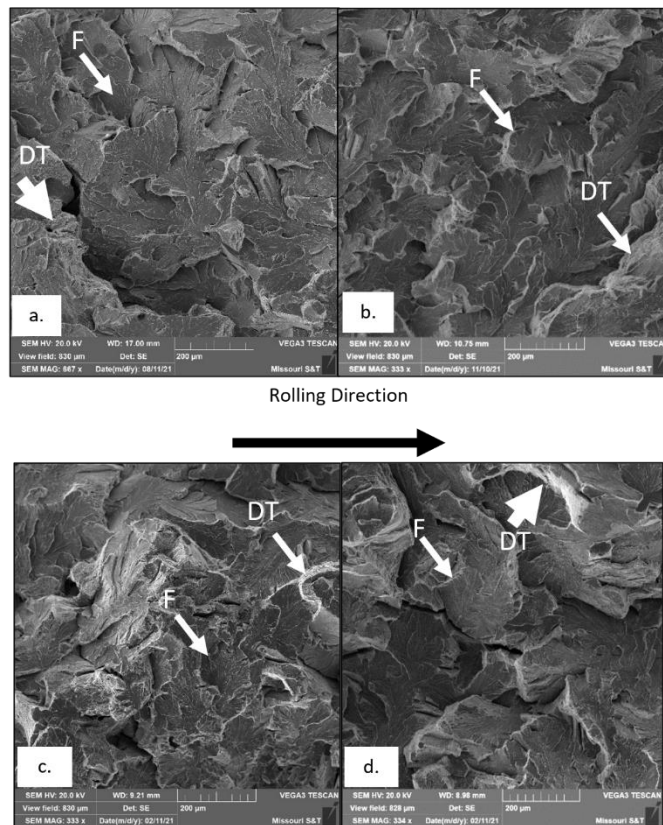


Figure 12. SEM fractography images of the as-rolled specimens in the L-S orientation. (a) As-rolled 830°C (b) as-rolled 900°C (c) as-rolled 1000°C (d) and as-rolled 1200°C. A finer cleavage facet size is observed in (a and b) Labeled are “DT” or ductile tearing ridge and “F” represents a cleavage facet.

As observed in Figure 13a, the presence of porosity in the centerline segregation region is illustrated more clearly. These pores are greater than 100 μm in size. A higher magnification image of a single pore is shown in Figure 13b, which shows that the pore has a size of around 50 μm in length. In comparison, the isothermal rolling samples are shown in Figure 14a-d. The samples were prepared in the same way the as-cast samples were described with the surfaces oriented the same as the fracture surfaces presented in Figure 14a-d for the as-rolled samples in the L-S orientation. The higher magnification was selected to validate the existence of proeutectoid ferrite forming on PAGB (Figure 14c at 1000°C) and nonmetallic inclusions (Figure 14a at 830°C, Figure 14b at 900°C, and Figure 14d at 1200°C). Additionally, at 1000°C porosity is present inside the proeutectoid ferrite. The pore is on the order of 2 μm , which is fine compared to the porosity observed in Figure 13 in the as-cast condition. This difference in porosity is qualitatively significant and likely plays a role in the improvement in toughness between the as-cast and as-rolled conditions.

Thus far, the microstructure has been discussed in terms of the microstructural constituents including pearlite and proeutectoid ferrite. Brief comments have been made to explain the effect of nonmetallic inclusions and steel cleanliness, which also influence toughness. The typical inclusions found in the specimens are shown in Figure 14. The primary inclusions present were large MnS stringer inclusions that formed due to the presence of fairly high S content (~200 ppm) in this steel. The Mn and S peaks in the EDS spectrograph are depicted in Figure 15. The full results for Charpy testing at -20°C and 20°C and quantitative investigation of relevant microstructural features are summarized in Table 2. The results show that at 20°C the L-S orientation shows an

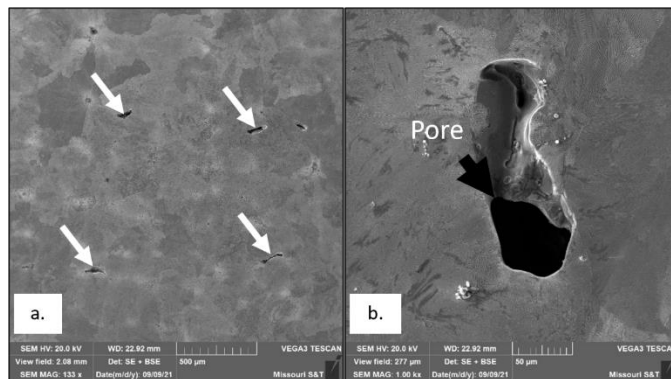


Figure 13. SE images (etched with 4% Picral) just below the fracture surfaces of the as-cast specimen show that porosity is prevalent.

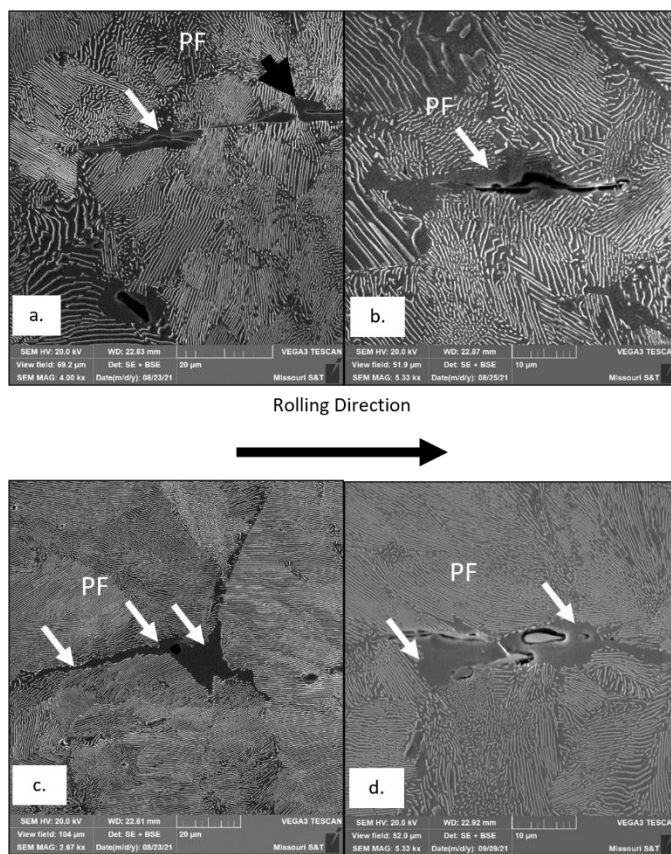


Figure 14. SE images just below the fracture surface of hot rolled specimens tested at 20°C in the L-S orientation. Micrographs correspond to specimens hot rolled at 830°C (a), 900°C (b), 1000°C (c), and 1200°C (d). Pearlite carbide/ferrite lamellae are resolved as well as proeutectoid ferrite or “PF” and MnS inclusions.

increase in all rolling conditions with respect to the as-cast condition and the average breaking energy increases from 5.4 J to 7.3 J as the isothermal rolling temperature is dropped from 1200°C to 830°C. This increase can be directly correlated with both the decrease in PAG size and an increase in proeutectoid ferrite content although the relationship with proeutectoid ferrite content is not as strong as the relationship with PAG size. The T-L orientation appears to illustrate the point where recrystallization and pancaking occur during hot rolling as the 1000 and 1200°C exhibit isotropic behavior, while at 830 and 900°C a significant drop between the L-S orientation and T-L orientation is observable. This observation is evidence for the preferred crystallographic orientation and thus anisotropy in those samples. Depending on material requirements an argument may be made about the value of isotropic properties as opposed to increased toughness in the L-S orientation with anisotropy. However, despite the anisotropy experienced at 830°C the T-L orientation at 20°C exhibits a higher toughness than the as-cast condition. All rolled conditions have similar or slightly lower toughness in the T-L orientation at -20°C. At -20°C the L-S orientation shows a similar trend although the comparison between the 1200 and 830°C is not as compelling in this condition with an increase from 4.2 J to 4.5 J. When reviewing the graphical results (Figure 10a), it can be seen that this is partly due to fairly large standard deviation which may be due to variation in strain throughout the rolled plate during hot rolling which has been simulated by Buchely et. al for the Missouri S&T STANAT mill.²⁵ A drop at -20°C is also expected due to the influence of varied grain size on the transition temperature being narrower at lower temperatures. Regardless, an increase in toughness is seen in the rolled conditions versus the as-cast condition.

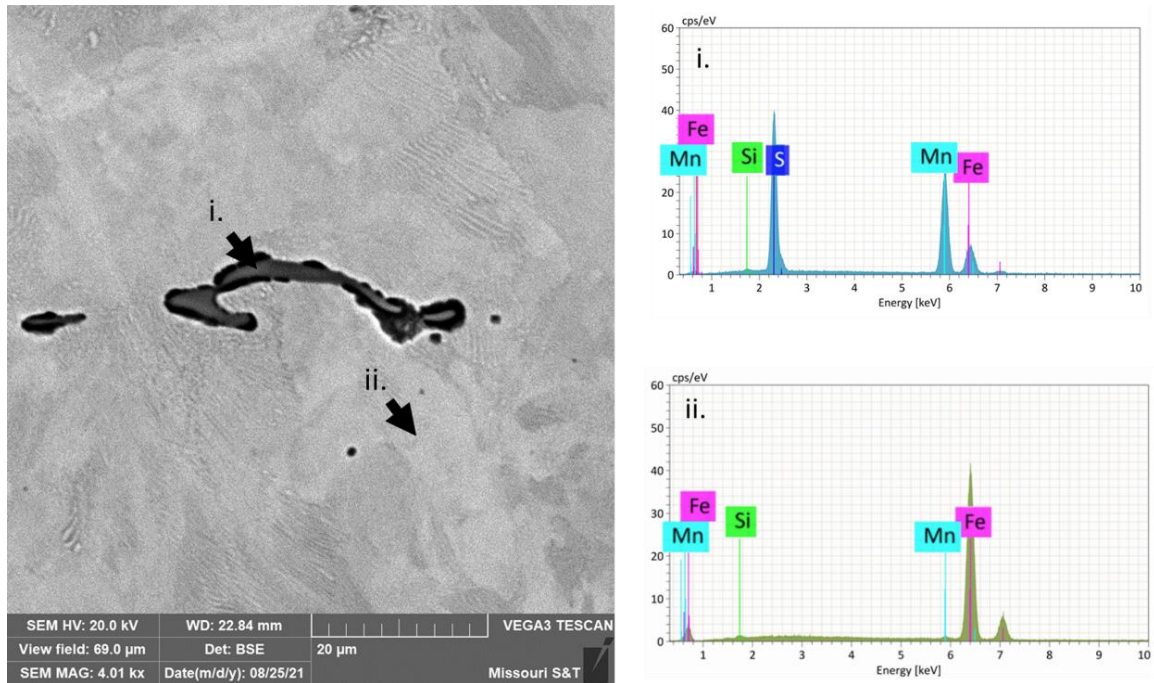


Figure 15. EDS measurements obtained for comparison of MnS to matrix material in the L-S orientation of the as-rolled sample held isothermally at 1200°C.

4. CONCLUSIONS

The notch toughness of AISI 1070 steel wheel castings was evaluated in comparison to hot rolled plates to simulate the ring-rolling process on near net shape preforms and adjudicate any microstructural or mechanical property benefits. Hot rolling isothermally at a temperature of 830°C led to a decrease in the prior austenite grain size during hot deformation which in turn is suggested to increased nucleation sites for ferrite during hot deformation which in turn is suggested to increased nucleation sites for ferrite during controlled cooling ($\sim 0.1 \text{ s}^{-1}$) thus increasing proeutectoid ferrite content and increasing toughness. In comparison to the as-cast condition, the notch toughness in the L-S orientation was increased from 3.4 J to 7.3 J in the as-rolled 830°C condition. Future

Table 2. Notch toughness results and corresponding microstructural feature quantitative analysis.

Tested Sample	Orientation	Charpy Impact Results (J)		PAGs (μm)	Pro-eutectoid Ferrite Content (wt. %)
		U-notch	V-notch		
Cast Segregate Region	L-S	3.4	2.7	930.5* \pm 250.7	0.1 \pm 0.1
	T-S	3.6	3.2		
	T-L	3.6	3.8		
As-rolled 830°C	L-S	7.3	4.5	22.8 \pm 11.5	1.1 \pm 0.6
	T-S	5.1	3.3		
	T-L	4.8	3.2		
As-rolled 900°C	L-S	6.8	5.6	43.2 \pm 19.1	3.2 \pm 2.0
	T-S	4.4	4.3		
	T-L	4.5	3.2		
As-rolled 1000°C	L-S	5.8	5.0	72.7 \pm 32.5	0.9 \pm 0.6
	T-S	5.9	5.1		
	T-L	5.6	4.0		
As-rolled 1200°C	L-S	5.4	4.2	198.1 \pm 87.4	0.2 \pm 0.2
	T-S	5.3	5.1		
	T-L	5.7	4.5		

work could be conducted to further refine the grain size and examine adding microalloying elements (Ti, V, Nb) to improve the toughness of AISI 1070 steel during deformation processing.

ACKNOWLEDGMENTS

This work was supported by Amsted Rail Company and the Peaslee Steel Manufacturing Research Center (PSMRC) at Missouri S&T and the authors would like to thank them for sponsorship and support for the Cast Pre-Form Forging project.

REFERENCES

1. Guo, F., Wang, X., Liu, W., Shang, C., Misra, R. D. K., Wang, H., Zhao, T., & Peng, C. (2018). The Influence of Centerline Segregation on the Mechanical Performance and Microstructure of X70 Pipeline Steel. *Steel Research International*, 89(12), 1–8. <https://doi.org/10.1002/srin.201800407>
2. Kundu, A., Davis, C. L., & Strangwood, M. (2008). Grain structure development during reheating and deformation of niobium-microalloyed steels. 3rd International Conference on Thermomechanical Processing of Steels, TMP 2008, March.
3. Hyzak, J. M., & Bernstein, I. M. (1976). The role of microstructure on the strength and toughness of fully pearlitic steels. *Metallurgical Transactions A*, 7(8), 1217–1224. <https://doi.org/10.1007/BF02656606>
4. Zeng, D., Lu, L., Gong, Y., Zhang, N., & Gong, Y. (2016). Optimization of strength and toughness of railway wheel steel by alloy design. *Materials and Design*, 92, 998–1006. <https://doi.org/10.1016/j.matdes.2015.12.096>
5. Elwazri, A. M., Wanjara, P., & Yue, S. (2005, July 11). The effect of microstructural characteristics of pearlite on the mechanical properties of hypereutectoid steel. *Materials Science and Engineering: A*. <https://www.sciencedirect.com/science/article/pii/S0921509305005459>.

6. Krauss, G. (2018). Microstructures, Processing, and Properties of Steels[1]. Properties and Selection: Irons, Steels, and High-Performance Alloys, 1, 126–139. <https://doi.org/10.31399/asm.hb.v01.a0001008>
7. B. Karlsson, G. Linden, Mater. Sci. Eng. 17 (1975) 153.
8. Bramfitt, B. L., & Corporation, B. S. (2018). Structure/Property Relationships in Irons and Steels. Metals Handbook Desk Edition, 153–173. <https://doi.org/10.31399/asm.hb.mhde2.a0003090>
9. ASTM E 23-12c. (2018). Standard test methods for notched bar impact testing of metallic materials. Standards, 1–25. <https://doi.org/10.1520/E0023-18>.
10. T. Gladman, I. McIvor, F.B. Pickering, J. Iron Steel Inst. 210 (1972) 916.
11. Handbook, M. (2018). Impact Toughness Testing. Mechanical Testing and Evaluation, 8, 596–611. <https://doi.org/10.31399/asm.hb.v08.a0003308>
12. Practice, S. (2016). Standard Practice for Microetching Metals and Alloys ASTM E-407. 07(Reapproved 2015), 1–22. <https://doi.org/10.1520/E0407-07R15E01.2>
13. INTERNATIONAL, A. (2010). Standard Test Methods for Determining Average Grain Size. Astm E112-10, 1–27.
14. Hutchinson, B. (2015). Critical assessment 16: Anisotropy in metals. Materials Science and Technology (United Kingdom), 31(12), 1393–1401. <https://doi.org/10.1179/1743284715Y.0000000118>
15. Thackray, R., Palmiere, E. J., & Khalid, O. (2020). Novel etching technique for delineation of prior-austenite grain boundaries in low, medium and high carbon steels. Materials, 13(15). <https://doi.org/10.3390/MA13153296>
16. Khzouz, E. (2011). Grain Growth Kinetics in Steels. A Major Qualifying Project Report Submitted to the Faculty of the WORCESTER POLYTECHNIC INSTITUTE, 5–6. https://www.wpi.edu/Pubs/E-project/Available/E-project-042211-104204/unrestricted/MQP_-_Grain_Growth_Kinetics_in_Steels.pdf
17. Romaniv, O. N., Cherepanova, G. I., & Yarygina, L. M. (1966). ORIENTED THERMOMECHANICAL HARDENING AND RECRYSTALLIZATION OF HIGH-CARBON STEELS. 459–463.
18. Y.J. Park, I.M. Bernstein, The process of crack initiation and effective grain size for cleavage fracture in pearlitic eutectoid steel. Metall. Mater. Trans. A, 10 (11) (1979), pp. 1653-1664

19. B. Strnadel, P. Haušild, M. Karlik. Quasistatic and dynamic fracture of pearlitic steel, *Fract. Nano Eng. Mater. Struct.* (2006), pp. 495-496
20. D.A. Porter, K.E. Easterling, G.D.W. Smith Dynamic studies of the tensile deformation and fracture of pearlite, *Acta Metall.*, 26 (9) (1978), pp. 1405-1422
21. J.J. Lewandowski, A.W. Thompson. Microstructural effects on the cleavage fracture stress of fully pearlitic eutectoid steel *Metall. Mater. Trans. A*, 17 (10) (1986), pp. 1769-1786
22. E.M. Taleff, J.J. Lewandowski, B. Poursadian. Microstructure-property relationships in pearlitic eutectoid and hypereutectoid carbon steels *JOM J. Miner. Met. Mater. Soc.*, 54 (7) (2002) (25-3)
23. L.E. Miller, G.C. Smith Tensile fractures in carbon steels *J. Iron Steel Inst.*, 208 (11) (1970)
24. Fernandino, D. O., & Boeri, R. E. (2018). Fracture Analysis. *Cast Iron Science and Technology*, 1, 399–410. <https://doi.org/10.31399/asm.hb.v01a.a0006323>
25. Buchely, M., Aken, D., O'Malley, R., Lekakh, S., & Chandrashekhara, K. (2018). Hot Rolling Effect upon the High Temperature Johnson-Cook Strength and Failure Models for a 15V38 Grade Steel. 1045–1053. https://doi.org/10.7449/2017/mst_2017_1045_1053

II. ON THE EFFECT OF HOT ROLLING ON INCLUSION SIZE AND DISTRIBUTION IN AN AISI 1070 STEEL

Jacob M. Summers, Soumava Chakraborty, Laura N. Bartlett, Ronald J. O'Malley, Mario F. Buchely

Department of Metallurgical Engineering, Missouri University of Science and Technology, Rolla, MO 65409

Richard Pilon

Amsted Rail Company, Overland Park, KS, USA.

ABSTRACT

The goal of this work is to examine the effect of hot deformation on shrinkage porosity and non-metallic inclusions in an AISI 1070 grade steel industrially produced wheel casting. Steel cleanliness is an important consideration as it influences the mechanical properties of the final product. A high density of porosity and inclusions have been shown to be detrimental for mechanical properties, especially during hot rolling. Using a laboratory scale rolling mill, cast pre-forms were subjected to a 66% cumulative reduction to determine the effect of thermomechanical processing on void closure and inclusions that may produce anisotropy in mechanical properties. Quantitative Automated Feature Analysis, AFA, of inclusion type, size, morphology, and distribution was conducted utilizing an Aspex PICA-1020 scanning electron microscope to determine differences in inclusions and shrinkage porosity in the as-cast and as-rolled conditions. The results were compared with previously reported notch toughness values. Reduction in shrinkage porosity was also verified utilizing 3D micro-X-Ray CT-scans. The AFA

results showed a decrease in shrinkage porosity from 176.6 ppm in the as-cast condition to less than 34.7 ppm after rolling. Pores were in general much smaller and widely distributed after hot rolling and this would suggest improved impact properties. Analysis of nonmetallic inclusions revealed three primary categories of inclusions that included MnS, Al₂O₃, and complex inclusions that mainly consisted of MnS with an Al₂O₃ core, with small quantities of mixed silicates of Mn and Al and calcium aluminates (CaAl₂O₄).

1. BACKGROUND

Inclusions and shrinkage porosity have previously been associated with rail failures and have been reported by the American Railway Engineering Association (AREA) Committee on Rails in numerous AREA Bulletins as early as 1947.¹ Porosity has been shown by Hardin and Beckermann² to reduce the elastic modulus during fatigue testing of an AISI 8630 steel (Figure 1) measured by radiography. With a drop from 200 GPa to 150 GPa with a porosity fraction of just 0.2. Hot rolling has been shown by a variety of researchers to induce porosity closure due to the plastic compressive strain. Higher temperatures have been shown to close porosity more effectively through ease of welding of the matrix.³ In a study by Ganguly et al⁴ Johnson-Cook parameters were determined and applied for material flow predictions during plane strain hot rolling which were utilized to predict the effects of different rolling parameters on void closure. For the same reduction ratio temperature was directly proportional to increases in equivalent plastic strain from 0.3 at 1100°C to 0.45 at 1300°C for the same pass in the rolling

schedule. These modeling results are in agreement with experimental testing and modeling performed by Kukuryk⁵.

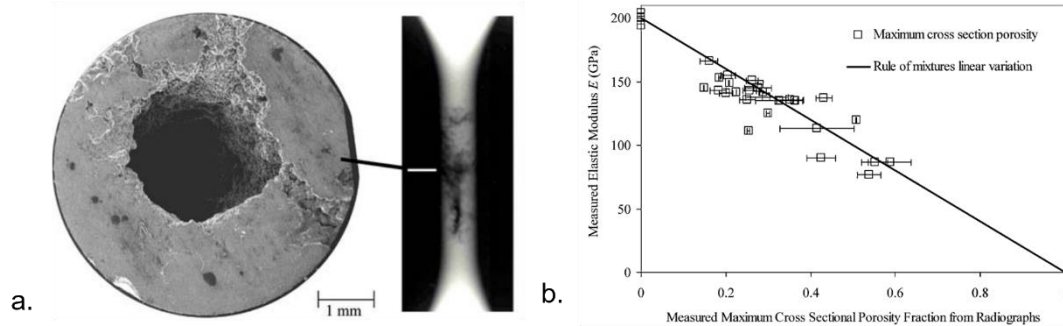


Figure 1. Radiography measurements of porosity in fatigue specimens and correlated results to measured modulus in GPa showing the detrimental effects of porosity on stiffness.⁶

Dhua et al investigated the effect of NMI on mechanical properties for commercial heats of pearlitic steel for application to the railway industry. Their work primarily focused on examining the effects of NMI on fracture toughness (K_{IQ}) and high-cycle fatigue limit. Reducing the volume fraction of inclusions from 0.45 wt. % to less than 0.19 wt. % increased fracture toughness, K_{IQ} from 42.33 MPa \sqrt{m} to 49.88 MPa \sqrt{m} . Increasing steel cleanliness also resulted in an increase in the fatigue limit from 319 to 355 MPa.⁷ Grigorovich et al⁸ examined mechanical properties across multiple rail producers in Europe and Asia and concluded that the volume fraction of coarse NMI could be used to characterize the sensitivity of the metal to contact-fatigue-crack nucleation. They showed the relationship between volume fraction of brittle oxide inclusions and their size correlated strongly with service durability (Figure 2) particularly with inclusions larger than 8 μm . It is well known that aspect ratio of NMI effects

mechanical properties and that hot rolling can cause elongated NMI which are detrimental for impact toughness.⁹ This is generally correlated to overall S content although at sufficiently low levels the S content is less impactful as shown in a study of a 0.3 wt. % C, Ni-Mo-Cr steel which had an anisotropy ratio, defined as the longitudinal toughness over the transverse toughness, of 3.5 for all hot rolled steel samples with sulfur contents in the range of 0.005 to 0.017 wt. %.⁹ Hot working effects brittle and plastic inclusions differently and can introduce directionality into the inclusion population as shown in Figure 3. Inclusions primarily act in three primary ways in response to hot rolling as shown in Figure 3a. The aspect ratio of plastic inclusions are most significantly effected by hot rolling as shown in Figure 3a which was correlated with upper shelf energies of a low C steel (Figure 3b) which detailed the detrimental effect of elongated plastic inclusions on toughness.¹⁰

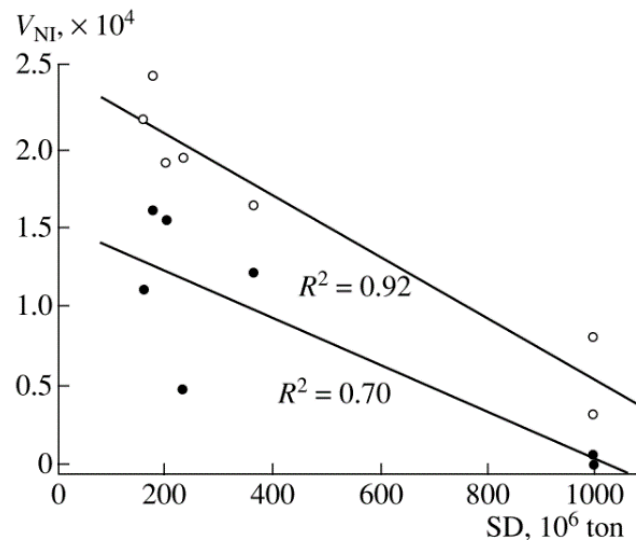


Figure 2. Relationship between oxide inclusion volume and service durability (SD) in tons during experimental ARIRT ring testing of oxide inclusions smaller than 8 μm (open circles, $R^2=0.92$), and oxide inclusions greater than 8 μm (closed circles, $R^2=0.70$).⁸

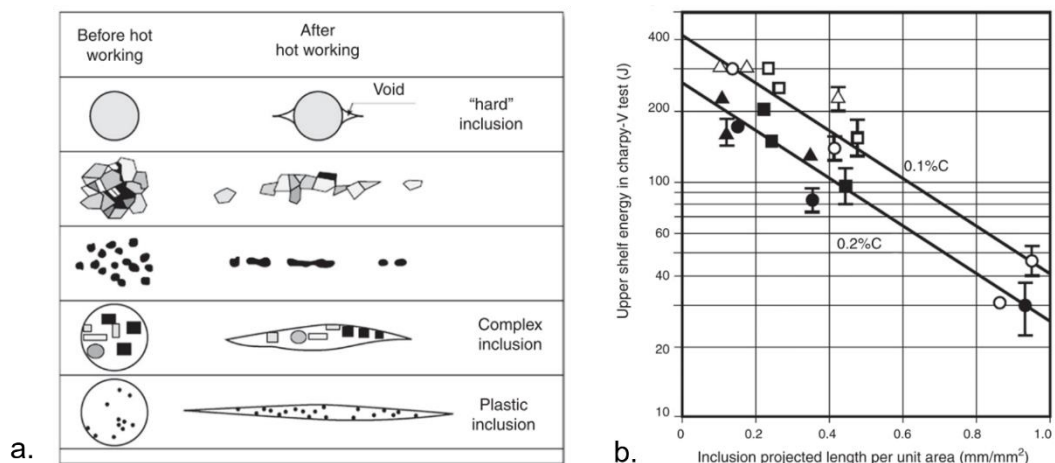


Figure 3. Depicted is a schematic of the effects of hot rolling on different types of inclusions (a) and the effect of projected length per unit area on upper shelf energy in a low C steel (b).^{10,11}

2. INTRODUCTION

While nonmetallic inclusions (NMI) are inevitable as a result of the steel refining and casting process, it is necessary to examine their effect on final microstructure and attempt to minimize the detrimental effects on mechanical properties. Sulfide and oxy-sulfides have inherent morphology related to the deoxidation practice and include Type I, Type II, Type III, and Type IV. Deoxidation practices involving Al involve preferential formation of Al_2O_3 from dissolved O due to the high O affinity of Al with compared to Fe. This also influences the morphology of sulfide inclusions. Type I morphology is produced by incomplete deoxidation resulting in random large globules with high residual O. If there is high residual Al content from deoxidation and low O, large angular and random, Type III formation is favored. If complete deoxidation is achieved there is low residual Al content and low O content favoring intergranular fine Type II sulfides.¹²

This type of MnS has been shown to be detrimental for impact toughness.¹³ Type IV is a modified globular morphology typically achieved through rare earth additions or calcium treatment. Therefore, this morphology is usually achieved as a part of inclusion engineering to form favorable inclusion morphology with desirable Al and O contents. It is well established in literature that hot worked NMI such as MnS result in anisotropic properties relating to decreases in transverse properties such as ductility, fatigue life, and impact toughness.¹⁴ In this work the deoxidation practice leads to very low dissolve Al content (~20 ppm) and low O (~30 ppm) leading to Type II being the expected morphology of sulfide inclusions. Hot working is desirable however to break down macrosegregation, minimize shrinkage porosity, and refine the grain structure of cast products. Macrosegregation results from the solidification during casting which is a function of the superheat of the melt.

In the casting process for train wheels, it is not traditionally possible to hot roll the material, and the traditional wheel rolling process in a forging line would not induce ample deformation to significantly alter mechanical properties. However, through the use of cast preforms subjected to a modified wheel rolling mill with greater localized deformation, such as in the web and rim section of the wheel, localized dynamic recrystallization (DRX) and location specific mechanical property improvement can be achieved through refinement of grain size. Understanding the effect of the simulated process on NMI and porosity will ensure the proposed process is viable and determine what level of impurity is allowable without excess anisotropy. Therefore, in an attempt to optimize mechanical properties for a high carbon steel through hot rolling, the NMI aspect ratio will be examined to determine if there is a correlation with aspect ratio and

anisotropy for previous experimental work. The goal of this work is to explain, if any, the discontinuities such as shrinkage porosity and NMI have on fracture in the investigated steels. This work will investigate the influence of isothermal rolling temperature on nonmetallic inclusions for a high carbon steel and the relationship between NMI and anisotropy.

3. PROCEDURE

The steel in question was cast industrially and sampled for examination. The average composition of the samples is given in Table 1. The samples were cast in an Electric Arc Furnace (EAF) with a fully killed deoxidation practice including Mn, Si, and Al. The steel was cast into semi-permanent graphite molds using pressure pouring technology resulting in columnar, dendritic solidification of the castings due to the high thermal gradient. The molds are oversized from the traditional final product to allow for the cast pre-form to be subjected to a modified wheel rolling mill. To simulate this process in a laboratory setting, isothermal hot rolling trials were conducted for an AISI 1070 steel at a 66% cumulative reduction. As a short summary of the treatment condition, samples were held for 1.5 hours at temperature to allow uniform heating and then were hot rolled from an initial thickness of ~43.5 mm to ~14.5 mm as described in Figure 4 and then prepared for Charpy testing by ASTM E23.

The L-S and T-L orientations were prepared for automated feature analysis (AFA) to analyze porosity and NMI and their effect on anisotropy in previous experimental results. Fracture surfaces were removed from Charpy specimens after testing at 20°C and

Table 1. Composition of the AISI 1070 as-cast steel in weight percent.

C*	Si	Mn	Cu	Cr	Mo	Ni	P	S*	Nb	Al	Ti	Fe
0.706	0.53	0.73	0.168	0.13	0.025	0.048	0.004	0.021	0.004	0.002	0.0008	Bal.

* Concentrations of sulfur and carbon were determined using LECO combustometric analysis

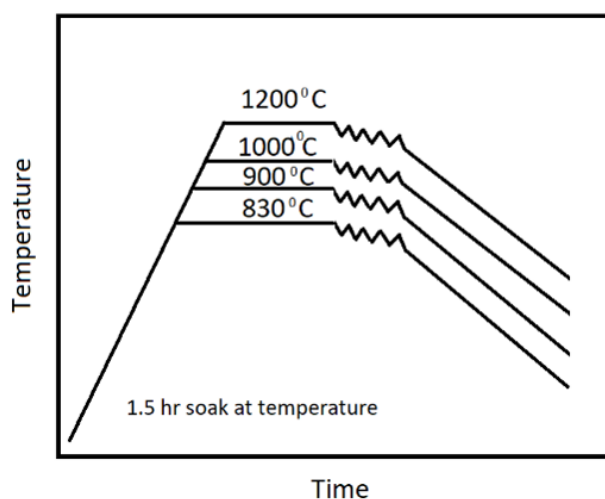


Figure 4. The steel casting was soaked in an electric box furnace with SiC elements for 1.5 hrs at the process temperature before hot rolling and subsequent slow cooling ($\sim 0.1 \text{ s}^{-1}$) in a refractory blanket.

the surface beneath was polished to $0.1 \mu\text{m}$. AFA was performed on an Aspx Scanning Electron Microscope (SEM) with an accelerating voltage of 20 kV. Two scans were combined for each flat polish surfaces, one focused on micro porosity and shrinkage porosity and the other for NMI. To ensure that the results are representative of the sample, Aspx PICA-1020 (Particle Identification and Characterization Analyzer) is utilized as shown in Figure 5. During this analysis a region is selected and broken down into multiple fields selected for analysis at random (Figure 5b,c). The fields are selected at random and broken down into 9 smaller fields (Figure 5d) which are then

systematically analyzed for differences in contrast from the metal matrix flagging in the system that an inclusion or pore is present. The center of such a feature is identified and EDS analysis is performed quickly to collect chemistry information of the particles for later classification along with measurement of diameter and area of each feature. A large number of inclusions for an effective comparison are obtained through Aspex PICA-1020 (3527-4082 dependent on number density). The location for analysis with respect to the industrially cast railway blank is shown in Figure 6 which is sectioned to include the centerline segregation region. Charpy specimens with a standard U-notch were tested at 20°C and prepared for analysis (Figure 5a) with the samples being sectioned directly below the fracture surface (~2 to 3 mm). The stitch scan is performed at a magnification of 1000x for the inclusion analysis and 200x for the porosity analysis to ensure proper measurement of coarse pores. Along with AFA, degree of porosity closure was also investigated through micro-X-Ray CT scans of the as-cast and as-rolled 1000°C material using a Xradia 510 Versa X-ray microscope. A stitched scan method was employed where an initial scan was run at 160 V and a second at 140 V and the two were overlaid to minimize artifacts and enhance the ability to post-process the samples. The CT results were processed into slices of ~10.66 μm which were then thresholded manually in Matlab, converted to a stack in Fiji and rendered in a 3D volume using the 3D viewer plugin. Particles were also measured in terms of volume and mean radius using the 3D Object Counter tool in Fiji. In the AFA and CT-scan, the particle information is obtained relating to the size and amount of the particles related to the overall scanned region which were analyzed and compared. Finally, to better understand the interaction between NMIs and shrinkage porosity on fracture in the as-cast and as-rolled samples, the fracture

surfaces from the L-S and T-L orientation were sectioned in half to reveal a cross section of the fracture surface and examine the relationship between the matrix and the primary crack as shown in Figure 7. Samples were polished to $0.05\ \mu\text{m}$ finish and etched with 4% Picral and then examined in the Tescan Vega3 scanning electron microscope (SEM) using an accelerating voltage of 20 kV. Back Scatter Electron (BSE) and Secondary Electron (SE) images were captured of relevant features.

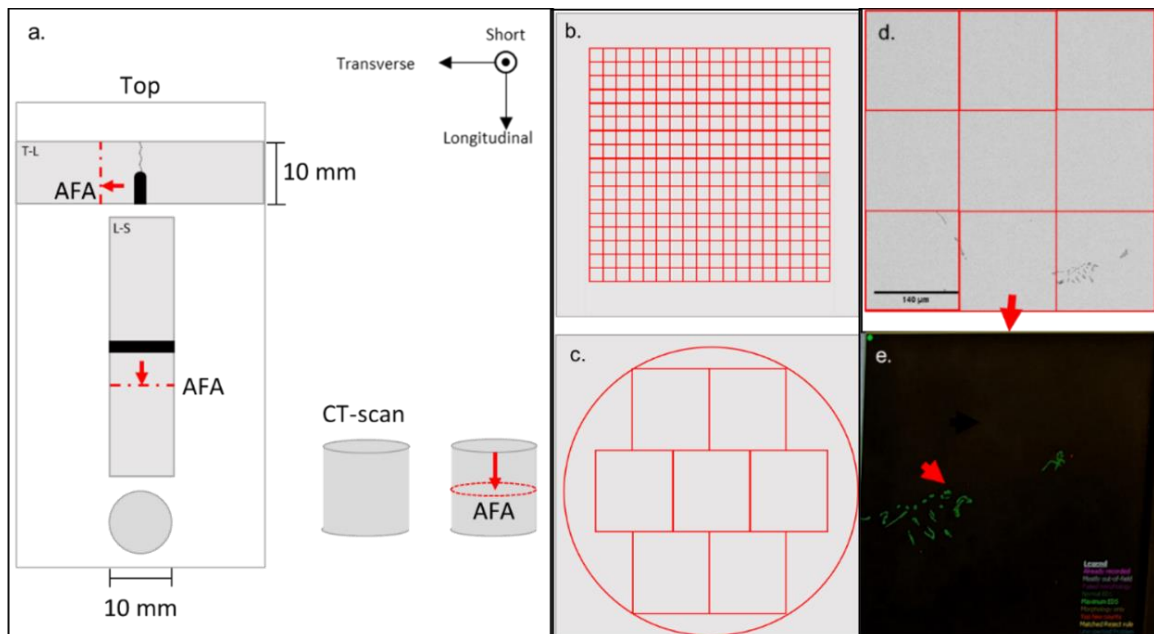


Figure 5. Aspex PICA-1020 performed in a stitched scan for shrinkage porosity and NMIs. Charpy specimens were prepared below the fracture surface for L-S and T-L samples and the CT-scan sample (10x10 mm cylinder) was removed from the as-cast and as-rolled 1000°C sample (a). The scan regions at 1000x for NMIs (b) and 200x for shrinkage porosity (c). A single field of the NMI scan is displayed in (d) which is split into 9 regions that are analyzed systematically for size, distribution, and chemistry (e).

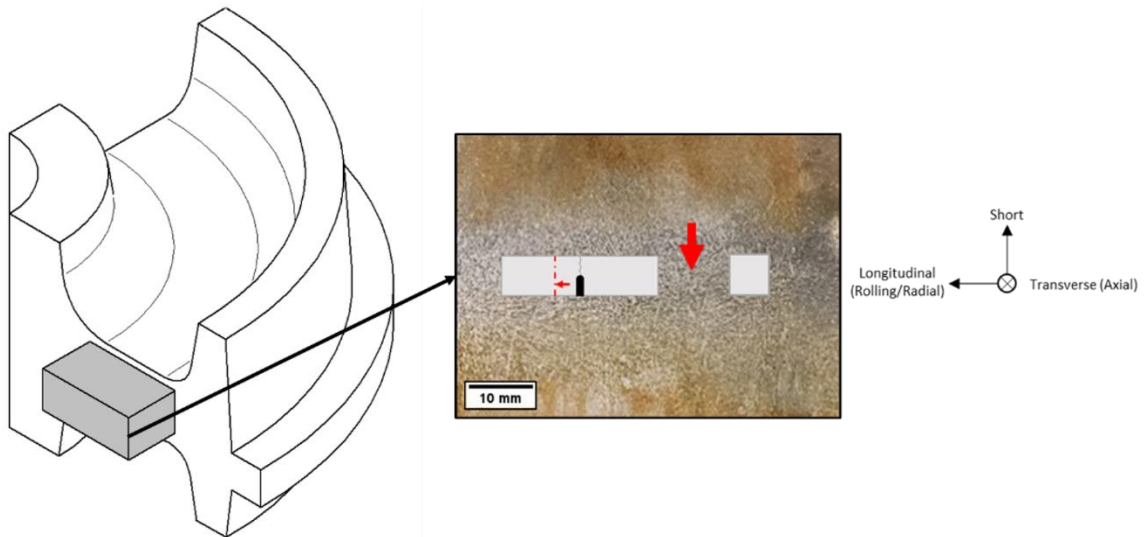


Figure 6. The location of the rolled samples as well as the sampling location is in the equiaxed region including the centerline segregation region for the as-cast and as-rolled samples.

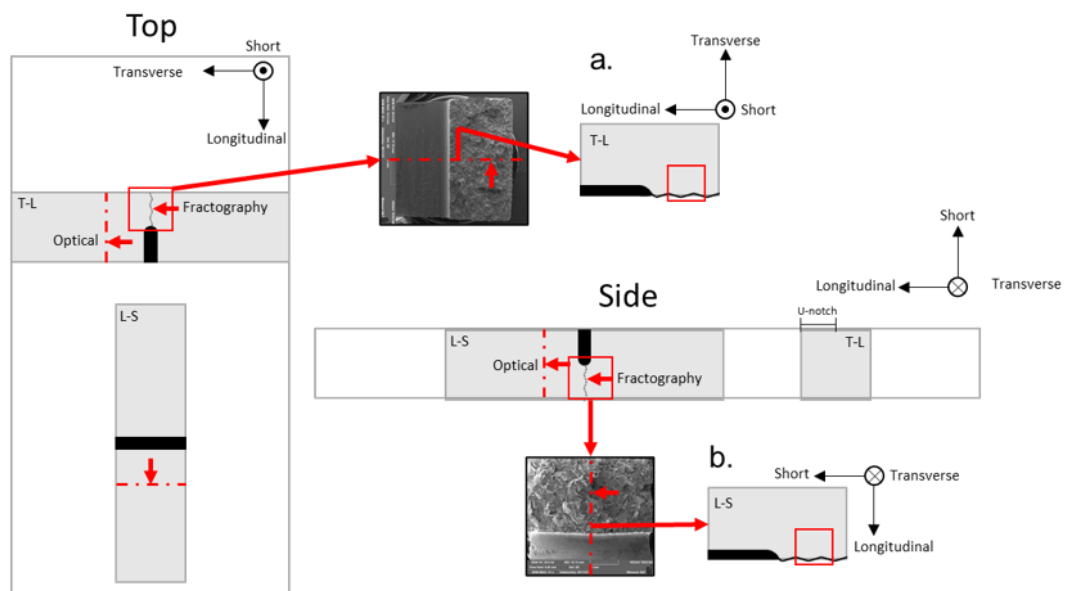


Figure 7. Depiction of the sectioning method used to prepare cross sections of fracture area to determine NMI and shrinkage porosity interaction with the primary crack. Etched with 4% Picral and the red box indicates the location for comparative BSE images. T-L (a) and L-S (b) are shown with relevant coordinate systems where the rolling direction and longitudinal are synonymous. Fracture surfaces in the chart are the as-cast segregate region sample at 20°C in the L-S orientation and as-rolled 830°C at a 66% cumulative reduction in the T-L orientation tested at 20°C.

4. RESULTS AND DISCUSSION

4.1. AFA POROSITY RESULTS

The AFA results for the porosity scan are plotted in Figure 8. The majority of the area fraction of all conditions is concentrated in the 5 to 40 μm which will be considered the beginning of the range of detrimental porosity size. The as-cast condition has the largest area fraction of pores greater than 5 μm at 159.4 ppm. Because of the deoxidation practice the expected content of dissolved porosity is expected to be ~30 ppm total porosity. The high content of coarse porosity indicates centerline shrinkage is present in the as-cast condition. The content of each as-rolled condition that is between 5 and 40 μm is between 0.4 and 34.1 ppm which indicates a significant reduction in shrinkage porosity at all temperatures. From 900°C to 1200°C there is also an apparent decrease from 34.1 to 0.4 ppm of porosity between 5 and 40 μm providing some evidence of temperature dependence. Porosity between 2 and 5 μm is also reduced in the as-rolled conditions from 11.7 ppm in the as-cast to the range 0.5 to 2.4 ppm at all rolling temperatures. In the as-cast condition 20.7 ppm is contributed to pores larger than 40 μm which is not observed in any of the rolled conditions. Along with size the nearest neighbor distance (NND) quantifies the distance between pores serving as an indicator of the likelihood to participate in crack initiation. The results of the NND calculation for each sample is shown in Table 2. The result of the decreased content of porosity in the as-rolled samples is a steady increase in the NND which illustrates the temperature dependence more readily with an increase in the NND from 542 μm at 830°C to 1246 μm at 1200°C. The trend is not directly supported by the area fraction versus mean diameter trends for the

rolled conditions, but this can be explained by the limitations of the Aspex PICA-1020 approach to measuring porosity. While all locations were held constant and were sampled from the region displayed in Figure 6 the porosity will still be randomly distributed throughout the samples which in the case of lowered overall content produces even more propensity for error with respect to single cross sections. Despite this the results still indicate that greater porosity closure was experienced at 1200°C which agrees with the results from Ganguly et al⁴.

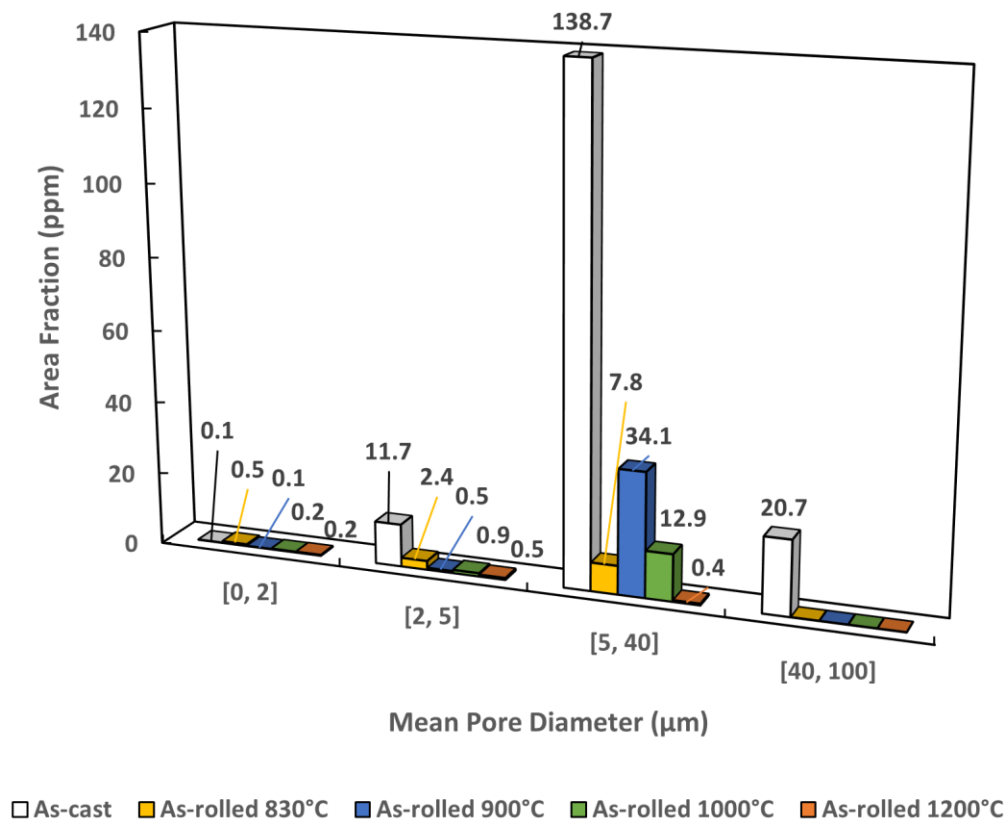


Figure 8. Area fraction (ppm) versus mean pore diameter (μm) in the as-cast and as-rolled conditions.

Table 2. Nearest neighbor distance (NND) calculation for the particles in each porosity scan.

Condition	Average NND (μm)	Standard Deviation (μm)
As-cast	219.3	248.8
As-rolled 830°C	542.2	421.5
As-rolled 900°C	712.7	825.8
As-rolled 1000°C	817.4	599.0
As-rolled 1200°C	1245.6	709.3

In an attempt to verify the results of the Aspex PICA-1020 and determine a more time efficient method for determining shrinkage porosity content the as-cast and as-rolled 1000°C sample being sectioned for micro-X-ray CT analysis. The results of scanning a 10x10 mm cylinder are shown in Figure 9. A qualitative comparison of the as-cast (Figure 9a) and as-rolled 1000°C (Figure 9b) shows that the large shrinkage porosity present in the as-cast condition is largely closed at a 66% cumulative reduction at 1000°C which agrees with the Aspex AFA results. A central slice with a height of 3.2 mm was investigated separately using the 3D Objects Counter in Fiji to determine the volume, surface area, centroid, and mean radius of each pore as shown in Figure 10. The sample is rendered three dimensional for the as-cast sample (Figure 10a) and as-rolled 1000°C (Figure 10c) with the central cross section displayed in Figure 10b and 10d for the as-cast and as-rolled 1000°C sample respectively. Red arrows indicate the thresholded porosity analyzed. By taking the relationship between mean volume and mean diameter in the analysis of this region, relationships in a log-log plot between the volume and diameter

were used to estimate the volume from the cross section analyzed in the AFA for comparison. Additional information on these calculations can be found in the Appendix.

The predicted volume for the as-cast and as-rolled 1000°C condition are compared to the mean volume from the CT-scan results along with a comparison of the mean diameter of the shrinkage porosity in Table 3. The mean diameter and mean volume reflect the same relationship between the AFA and the CT-scans. The scanned region in the AFA represents an area with smaller pores than that represented in the CT-scans. This is expected due to the variation in apparent shrinkage porosity content throughout the cast sample. The smallest pore measured in both samples is a mean diameter of 15.73 μm which explains the inconsistencies between the automated feature analysis and the CT-scans. The AFA has a minimum resolution of 0.5 μm . Therefore, by combining the techniques, it is possible to verify the closure of shrinkage porosity but not that of micro voids. However, micro voids less than eight microns are not expected to be as detrimental to mechanical properties.⁸ Area and volume fraction in ppm reported by mean pore size is plotted in Figure 11 to compare the results of the AFA and CT-scans further. It is of note that 92 to 93% of the porosity in the as-cast condition and as-rolled 1000°C is comprised of porosity larger than 5 μm . The peak porosity size shifts in the as-cast condition when comparing the AFA and CT-scan results. With a larger sample volume, it is likely that the peak shift to shrinkage porosity in the 40 to 100 μm is likely more representative of shrinkage porosity size than that of the cross section investigated through AFA. To further support this result, the cross section of the as-cast CT-scan sample was re-polished until shrinkage porosity was present on the surface. This feature was examined optically as shown in Figure 12 and processed in Fiji for mean diameter.

The formula obtained for the as-cast diameter-volume relationship in the central slice was applied to predict the mean volume of these features and can be seen tabulated in Table 4. This validates the existence of large shrinkage porosity in the CT-scans. Because this feature was not represented in the AFA it is likely that the mean diameter and predicted mean volume for the as-cast condition are underpredicted. To improve the prediction future work could involve mounting the full CT-scan sample, polishing to 12 iterative depths, and performing AFA on each region. Compromise of the diameter of the investigated sample for CT-scans could also improve the resolution down to 8 μm (~7 mm diameter sample) to ensure sufficient closure of detrimental voids. The time to perform the analysis of the central slice of the CT-scan using the 3D Object Counter allows for analysis of 300 regions per sample in 30 minutes whereas the AFA scan of 1 region per sample takes approximately 6 hours. Therefore, while the results of the automated feature analysis and CT-scan are difficult to correlate the micro-X-ray CT-scan does provide a cost effective and time effective technique for investigating shrinkage porosity closure during hot rolling indicating that hot rolling at a 66% reduction at 1000°C closed ~98% of the shrinkage porosity with a mean diameter greater than 15.73 μm with the AFA extending the analysis to micro voids down to 0.5 μm indicating that ~92% of the total porosity was closed.

4.2. AFA INCLUSION RESULTS

Inclusion size, distribution, and aspect ratio were examined as a function of thermomechanical processing were examined utilizing backscatter scanning electron (BSE) microscopy with energy dispersive X-ray spectroscopy (EDS).

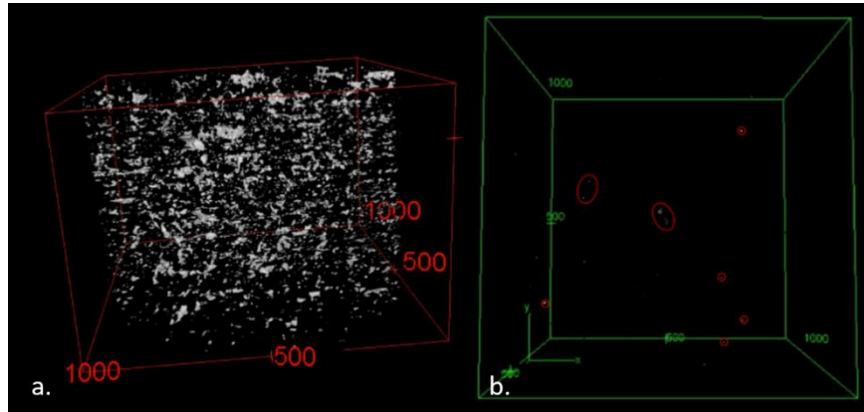


Figure 9. CT-scans of the as-cast (a) and as-rolled 1000°C (b) sample which visualizes the degree of closure of porosity at a 66% cumulative reduction.

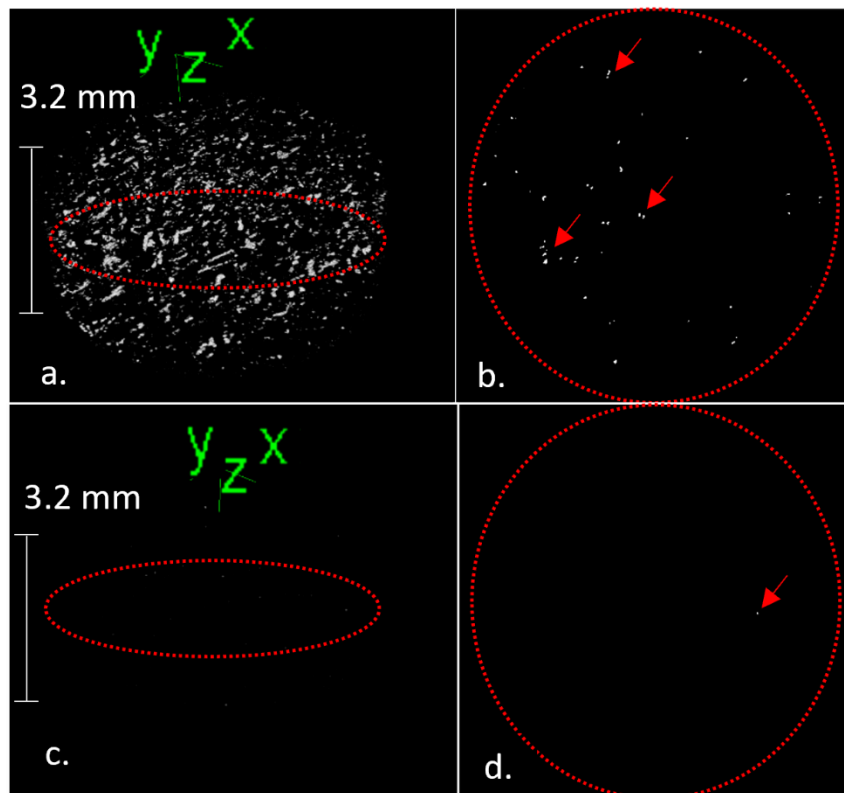


Figure 10. Central region (3.2 mm height) of the micro-X-Ray CT-scans in the as-cast (a,b) and as-rolled 1000°C (c,d) conditions. The red dotted line (a,c) represents the central cross section of each sample which is isolated for the as-cast (b) and as-rolled 1000°C (d) condition. Each individual particle thresholded had the volume, surface area, centroid, and mean radius calculated using the 3D Objects Counter in Fiji.

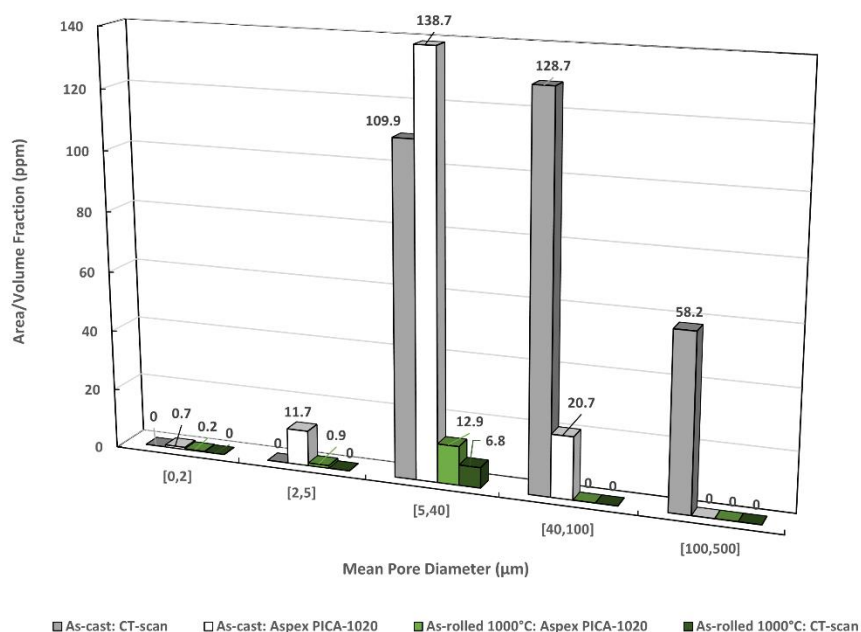


Figure 11. Area/Volume Fraction (ppm) of the as-cast and as-rolled 1000°C samples. The Aspex PICA-1020 and CT-scan methods are compared. From single cross sections the automated feature analysis results seems to underpredict the presence of shrinkage porosity for the as-cast condition.

Table 3. Summary of the Aspex PICA-1020 and micro-X-Ray CT-scans results including mean diameter (μm) and volume (μm^3) $\times 10^5$.

Condition	Mean Diameter (μm)		Mean Volume (μm^3) $\times 10^5$	
	Aspex PICA-1020	CT-scan	Aspex PICA-1020	CT-scan
As-cast	6.4	49.8	0.07	1.74
As-rolled 1000°C	4.3	24.2	0.03	0.18

The most prominent inclusions are MnS, Al_2O_3 , and complex inclusions of MnS and Al_2O_3 . Figure 13 displays the Type II MnS inclusions found in the as-cast material. MnS, Al_2O_3 , and complex inclusions of MnS and Al_2O_3 . The spectrograph shows the peaks for Mn and S along with trace amounts of C and N. Type II inclusions are the primary morphology of MnS in this steel which is expected with the fully killed

deoxidation practice with a residual content of 20 ppm Al which has been shown to be detrimental to

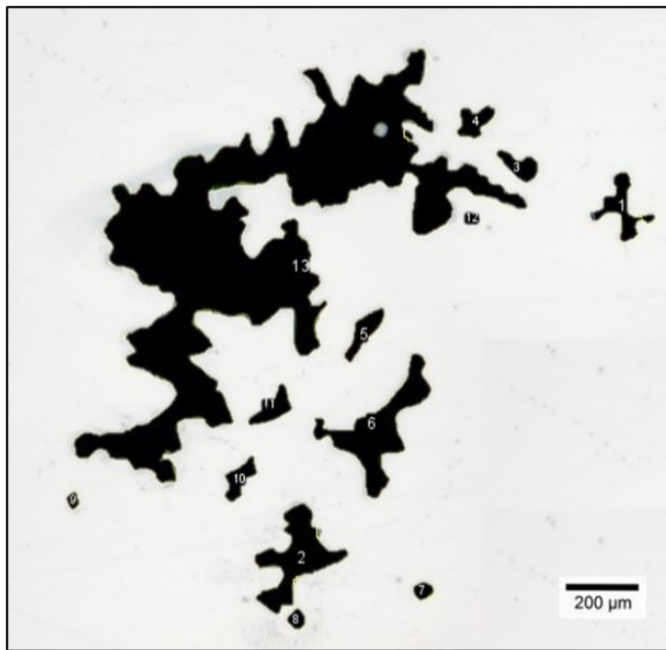


Figure 12. Optical microscopy of large shrinkage porosity (~1500 μm).

Table 4. Image analysis of mean diameter (μm) and mean volume (μm^3) $\times 10^5$.

Condition	Mean Diameter (μm)	Mean Volume (μm^3) $\times 10^5$
	Optical Sample	Optical Sample
As-cast	261.6	927.3

toughness.¹⁰ This is important because hot rolling alters the spacing and aspect ratio of deformable nonmetallic inclusions like MnS. Al_2O_3 is also seen in the cast structure as a small cluster as seen in Figure 14. The spectrograph shows a peak of Al and O as expected but also a small amount of Mn. The significance is that proper classification of NMI requires careful examination of the ternary phase diagram of primary inclusion

compositions and determining, along with verification from the images, what peak should be considered “trace”. Al_2O_3 inclusions are classified based on their Al content in the absence of scanning for O during AFA. Complex inclusions are also common in this steel which are a mixture of MnS and Al_2O_3 as seen in Figure 14. A MnS shell is observed on the Al_2O_3 inclusions which occurs due to preferential formation on the clusters which also typically maintain a round morphology, although a rodlike and round complex inclusion are seen in Figure 15. The peak for the MnS spectrograph of the inclusion has Mn and S peaks as expected with a well established Al peak. This is also true when examining the Al_2O_3 spectrograph which has Al and O peaks and discernible Mn peaks. The MnS acts as a shell for the Al_2O_3 inclusions and therefore when the center of a complex inclusion is measured the EDS map also includes the peaks from both Al_2O_3 and MnS phases making the classification discernible from pure Al_2O_3 or pure MnS inclusions.

To represent the particles in each condition, the raw results from the AFA were plotted in joint-ternary diagrams which were used to determine classifications of the inclusions. The as-cast condition is shown in the L-S orientation in Figure 16a and the T-L orientation in Figure 16b. The as-rolled 830°C and 1200°C AFA scans are represented in Figure 16c-f with 900°C and 1000°C in the T-L represented in Figure 17. The primary elements related to inclusions in this system are Mn, S, and Al. Si forms silicates with Al and Mn and trace amounts of Ca and Mg from contamination during casting from treatment and furnace refractory are also present resulting in formation of phases such as calcium aluminates. The average diameter of each inclusion is organized by size in the ranges of 0 to 2 μm , 2 to 5 μm , and 5 to 40 μm . To represent the size of inclusions present

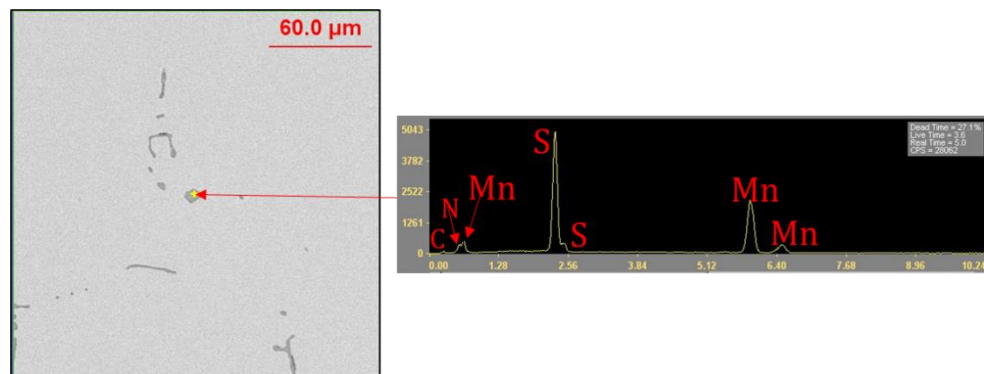


Figure 13. EDS spectrum of MnS inclusions. Type II and III MnS in as-cast material with 210 ppm S and residual Al from deoxidation of around 20 ppm.

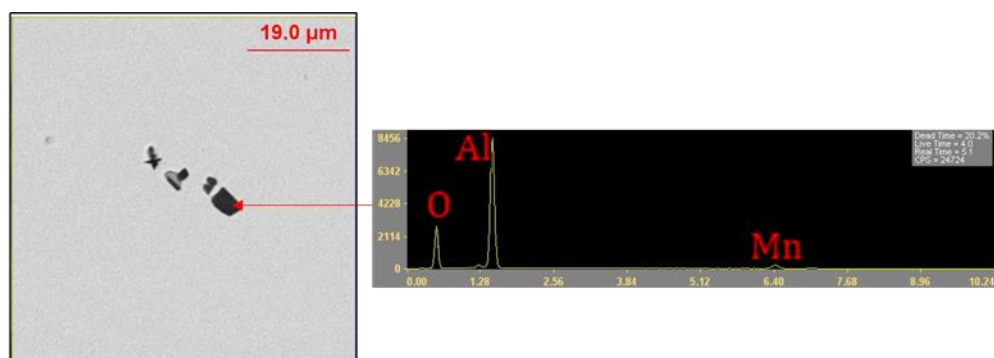


Figure 14. EDS spectrum of Al_2O_3 cluster. Al_2O_3 cluster in the as-cast material of a small enough size that it did not float out prior to solidification and became entrained in the metal as an inclusion.

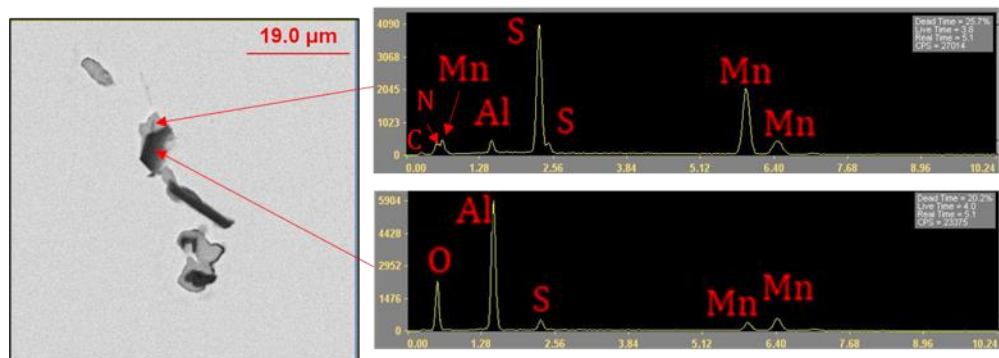


Figure 15. EDS spectrum of globular complex inclusion of Al_2O_3 and MnS inclusions.

in each condition, the percentage of each size range is displayed in a pie chart. It is of note that the as-cast (Figure 16b) and as-rolled 830°C (Figure 16d) sample both have inclusions of average diameter between 5 and 40 μm at an amount of 1% in the T-L orientation. The as-rolled 900°C (Figure 17a), 1000°C (Figure 17b), and 1200°C (Figure 16f) have no reported inclusions with an average diameter greater than 5 μm in the T-L orientation. This is the first indication that there is dependence on some factor that is controlling inclusion size that is not correlated with cumulative percent reduction. The amount of fine inclusions is similar for most conditions varying between 81 and 85% in the L-S orientation but the relationship in the T-L orientation shows some differences with the as-cast condition showing a larger percentage of particles between 2 and 5 μm (36%) compared to the as-rolled 830°C, 900°C, and 1200°C conditions with 21, 12 and 13% respectively. The as-rolled 1000°C has an especially high content of inclusion with an average diameter less than 2 μm (95%) compared to the other rolled conditions (between 78% and 88%).

The Mn-Al-S field and Mn-S-Si fields contain a large portion of the particles and were the focus when identifying the classifications of the NMIs. Based on these fields and point EDS, classification for MnS, Al_2O_3 , complex inclusions, and silicates, were determined for the raw data. The Mn-Al-S field represents the MnS, Al_2O_3 , and complex inclusions constituted by MnS and Al_2O_3 . Based on the Al content, samples were split into three regions for classification: 1) Less than 30% Al for MnS inclusions, 2) Between 30 and 70% being complex inclusions of MnS and Al_2O_3 in an agglomerate (complex), and 3) Greater than 70% Al being consistent with Al_2O_3 . Other rules include greater than 10 wt. % Mn and S correlating with MnS and less than that being necessary to classify a

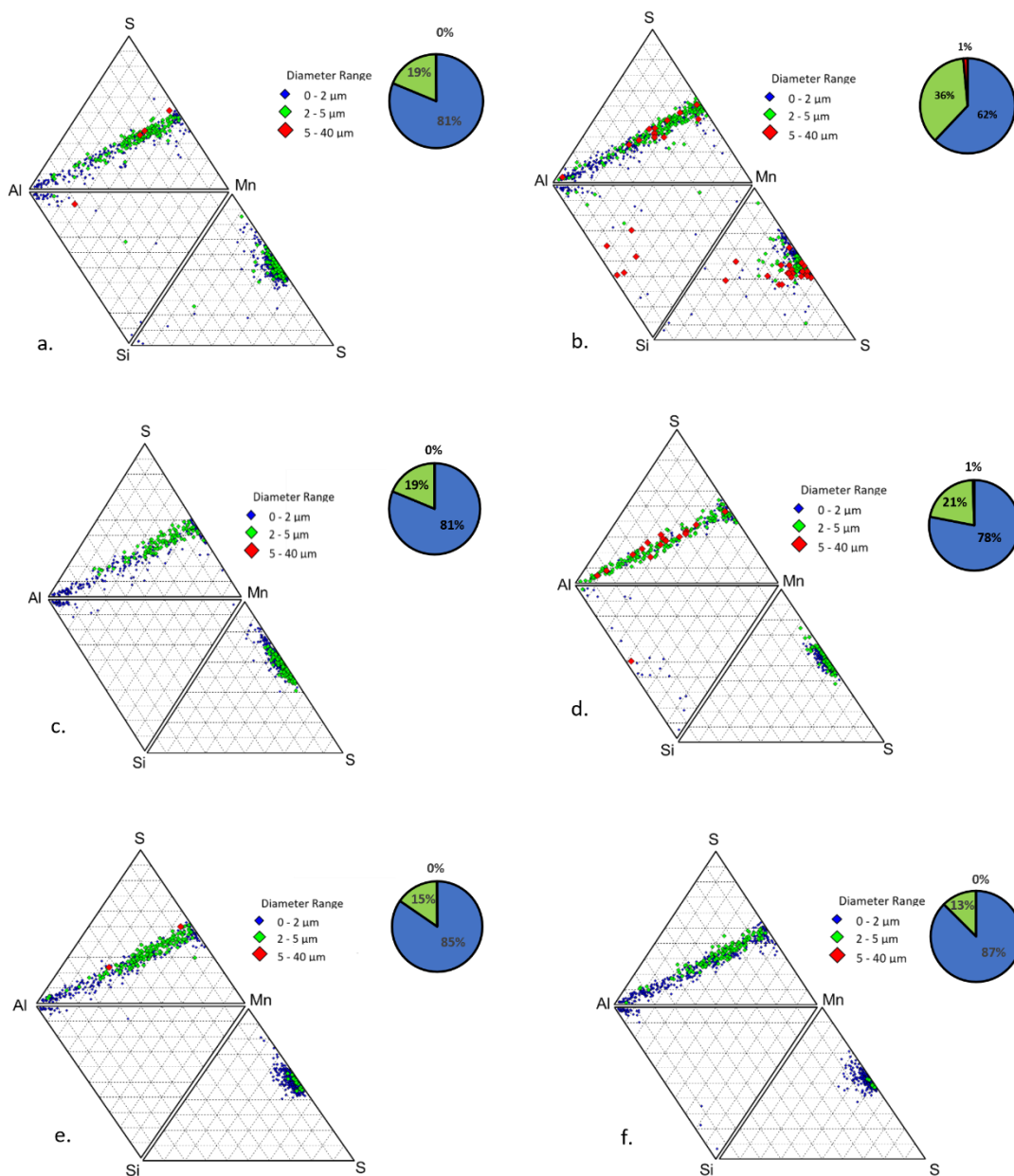


Figure 16. Ternary classification of the results from the Aspex AFA of the as-cast, as-rolled 830°C, and 1200°C along with a pie chart of the overall NMI size (%) are depicted. The as-cast condition is shown in the L-S orientation (a) and T-L orientation (b) As-rolled 830°C is compared for the L-S orientation (c) and T-L orientation (d), and the as-rolled 1200°C is compared for the L-S orientation (e) and T-L orientation (f). While it may seem insignificant the 1% of particles >5 μm in the T-L orientation at 830°C is the first indication of temperature dependence of NMI.

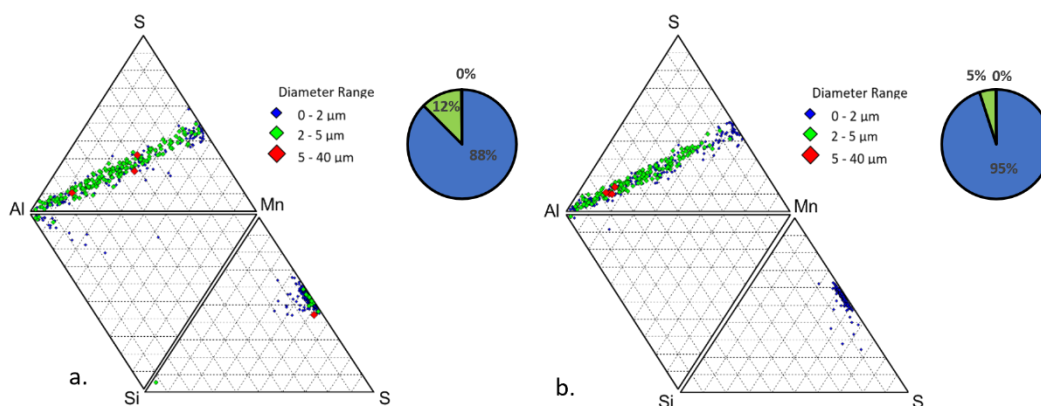


Figure 17. Ternary classification of the results from the Aspex AFA of the as-rolled conditions 900°C and 1000°C along with a pie chart of the overall NMI size (%) in the T-L direction.

particle as another phase. Silicates which are the primary phase in the Mn-S-Si phase were described as having a Si content that exceeds 10% but less than 90% and a mixture of Al, Ca, and Mn that was between 30% and 90%. CaAl_2O_4 includes greater than 10% Ca, trace amounts of Mn, S, Si, and Mg (<10%), and >30% Al. By characterizing the data in this manner, the area fraction of each NMI was determined for each condition and are represented in Table 5 for the T-L orientation and Table 6 for the L-S orientation with the shrinkage porosity content included from the previous section to represent the total steel cleanliness from the stitch scan reported as an average in previous section. The expected result is that the overall content of combined steel cleanliness should be close to equivalent for all conditions since they are of the same heat and sample location. MnS content varied 7 to 35% from the average between samples. The Al_2O_3 content varied 13 to 32% from the average and complex inclusion content varies from ~6 to 33% from the average for all samples. The biggest difference in the composition is the apparent mixed silicate of Mn and Al content in the T-L orientation and CaAl_2O_4 content in the L-S

orientation. CaAl_2O_4 was excluded from the T-L table as the contents are quite small in all conditions $>0.003\%$ and the same was done for the L-S orientation with mixed silicates of Mn and Al. Table 7 lists the average alloy composition from the EDS measurements of the classified particles in the as-cast and as-rolled conditions which were averaged over all conditions with respect to the individual orientations investigated which show good agreement. The data is also represented graphically in Figure 18 for

Table 5. Summary of the area fraction in ppm of NMIs in each condition in the T-L orientation.

Condition (T-L)	Nonmetallic inclusions and Porosity Amounts (ppm)					
	MnS	Al_2O_3	Complex	Silicates	Porosity	Total (ppm)
As-cast	466.2	14.4	30.7	38.2	225.6	775.0
As-rolled 830°C	503.2	24.2	46.6	6.1	28.4	608.5
As-rolled 900°C	337.4	22.0	42.9	0.3	56.6	459.3
As-rolled 1000°C	215.1	27.6	43.3	0.0	38.2	324.2
As-rolled 1200°C	373.4	15.4	25.7	0.0	2.6	417.1

Table 6. Summary of the area fraction in ppm of NMIs in each condition in the L-S orientation.

Condition (L-S)	Nonmetallic inclusions and Porosity Amounts (ppm)					
	MnS	Al_2O_3	Complex	CaAl_2O_4	Porosity	Total (ppm)
As-cast	567.5	9.9	27.1	0.2	178.5	783.2
As-rolled 830°C	836.1	13.8	27.7	1.8	11.8	891.3
As-rolled 1200°C	515.7	29.2	40.1	11.8	7.3	604.1

both the L-S orientation and T-L orientation. From the figures, it can be seen that MnS comprises the majority of the area fraction in both cases (75-95%) which is expected due to the bulk Mn (0.73 wt. %) and S (~210 ppm) content of the steel. Along with Al_2O_3 , complex inclusions, and silicates the deoxidation practice leads to all inclusions. The

Al_2O_3 content in each sample is similar to the result measured in OES (20 ppm). The small inclusions observed remain from steelmaking due to the inability to float to the slag layer prior to solidification. MnS form preferentially on some Al_2O_3 forming complex inclusions. While the variance in MnS content is unexpected the variance between the majority of the samples is relatively low as they are all sampled from the same heat in the

Table 7. The average inclusion compositions for classified particles averaged for the as-cast and as-rolled conditions which includes MnS, Al_2O_3 , complex inclusions of MnS and Al_2O_3 , mixed silicates, and CaAl_2O_4 .

Inclusion Classification	Average Alloy Composition from EDS					
	Mg	Al	Si	S	Ca	Mn
MnS	0.0	0.5	0.4	46.1	0.0	52.9
Al_2O_3	1.3	91.6	0.9	2.1	0.5	3.6
Complex	0.7	49.5	0.5	22.4	0.3	26.6
Mixed Silicates	1.6	44.8	33.7	2.9	6.7	10.3
	Mg	Al	Si	S	Ca	Mn
MnS	0.0	0.6	0.6	45.2	0.1	53.6
Al_2O_3	1.1	91.2	1.2	1.5	1.5	3.6
Complex	0.5	46.1	0.6	23.4	0.3	29.2
CaAl_2O_4	0.1	82.0	1.9	0.4	13.4	2.2

same location. The as-rolled 1000°C is the only sample which shows evidence of significant decrease in the MnS and thus the S level. The area fraction, number density, and aspect ratio for each major inclusion were investigated to determine if there is an effect of hot rolling on NMI evolution. MnS inclusions are displayed for the L-S and T-L orientation in Figure 19. For the upper and lower temperatures which were investigated in the L-S orientation, the dependence on hot rolling temperature for area fraction (Figure

19a), number density (Figure 19c) and aspect ratio (Figure 19e) seems to be very little if any. The MnS have a similar fraction and density to that of the as-cast material in the L-S orientation. The T-L orientation, however, shows a shift in MnS size and area fraction, when investigating the differences in the MnS content in each sample it is evident that

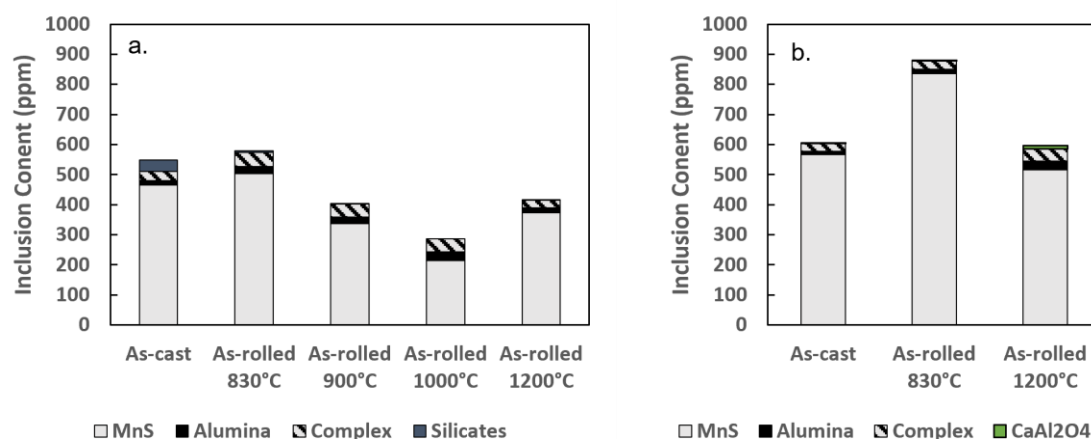


Figure 18. A graphical representation of the area fraction of the NMIs in each condition for the T-L (a) and L-S (b) orientations.

these peaks coincide with the MnS content. The aspect ratio of MnS in the as-rolled conditions shows an increase from the as-cast condition which shows some evidence that hot rolling has elongated them preferentially in the rolling direction. As mentioned this occurs due to the pliability of MnS inclusions at hot working temperatures, however, the as-rolled 830°C seems to be the only sample with appreciable size which seems to correlate with increased MnS area fraction.¹⁷ In the L-S orientation the Al₂O₃ inclusions shown in Figure 20 have a very similar size and distribution in the as-cast and as-rolled conditions (Figure 20a) which is also observable in the number density (Figure 20c). In the T-L orientation (Figure 20b) slight decreases in overall area fraction of Al₂O₃ for the

rolled conditions results in a decrease in the average size and number density with the area fraction being similar for each condition. The complex inclusions were investigated in Figure 21. From Figure 21a the area fraction of complex inclusions in the L-S orientation is fairly similar in the as-cast and as-rolled conditions. No appreciable difference should be noted in the complex inclusion population though with similar aspect ratios as well. The relationship in the T-L orientation shows that the area fraction distribution peak seems to increase with rolling temperature but is actually correlated to area fraction of complex inclusions (Figure 21b). This is also supported by the low aspect ratio for all rolling conditions regardless of size which will prevent stress concentration at complex inclusions (Figure 21f). However, the as-rolled 830°C again shows deviations from the other rolled conditions with larger sizes reported although the aspect ratio is similar to the other rolled conditions.

The nearest neighbor density (NND) averaged between all inclusions is displayed in Table 8. This includes the distance between MnS, Al₂O₃, complex, mixed silicate inclusions, and CaAl₂O₄ with 75 to 95% of the particles in each condition being constituted by MnS inclusions. The L-S orientation shows that the NND increases between the as-cast and as-rolled 830°C from 6.9 to 9.4 μm and again from 830°C to 1200°C with an increase from 9.4 to 14.8 μm. In the T-L orientation the spacing between particles is fairly similar between the as-cast sample and the material rolled at 830°C and 1000°C. However, 1200°C is different showing a NND of 14.9 μm as opposed to 12.1 μm in the as-cast condition. This seems to further support the relationship in the L-S orientation. An interesting relationship is that the NND increases from the L-S to T-L in the as-cast and as-rolled 830°C but at 1200°C is similar for both orientations.

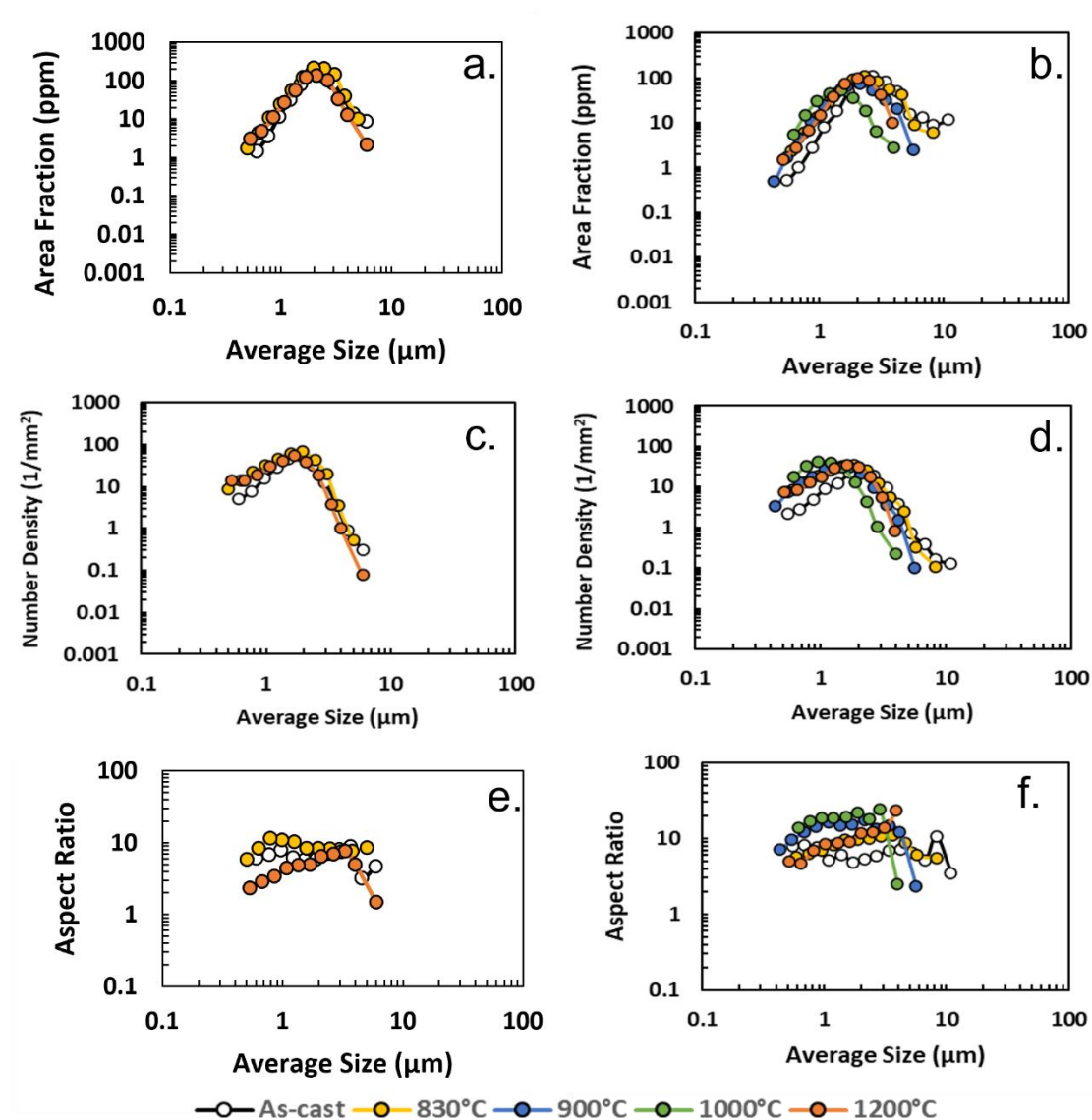


Figure 19. The average size, distribution, and aspect ratio of MnS inclusions were examined from the Aspex PICA-1020 results on log-log plots. The as-cast, as-rolled 830°C, and as-rolled 1200°C were examined in the L-S orientation for area fraction (ppm) (a), number density (1/mm²) (c) and aspect ratio (e) vs. average size. The as-cast and as-rolled isothermal temperatures of 830°C, 900°C, 1000°C, and 1200°C were also examined in the T-L orientation for area fraction (ppm) (b), number density (1/mm²) (d) and aspect ratio (f) vs. average size.

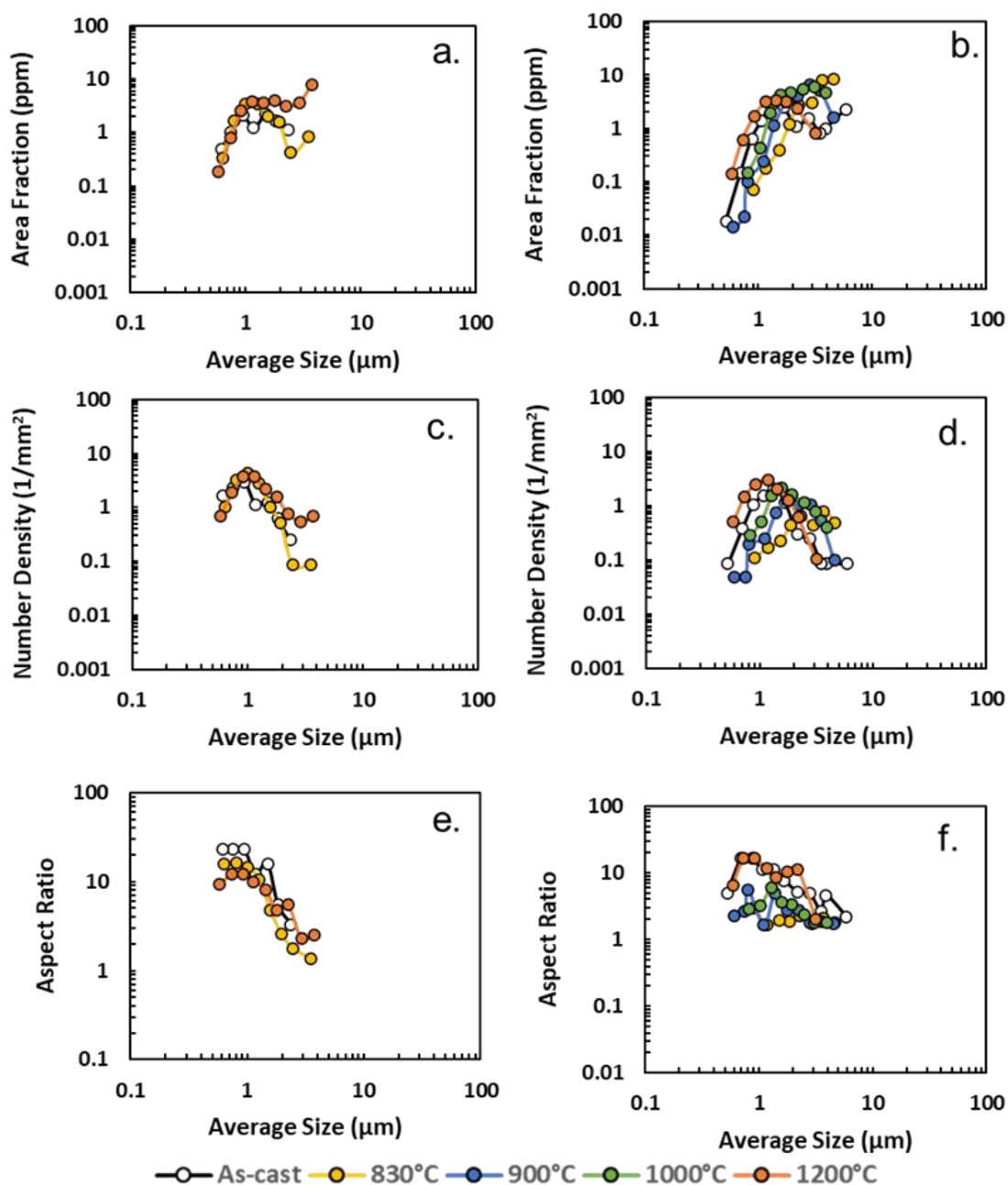


Figure 20. The average size, distribution, and aspect ratio of Al_2O_3 inclusions were examined from the Aspex PICA-1020 results on log-log plots. The as-cast, as-rolled 830°C, and as-rolled 1200°C were examined in the L-S orientation for area fraction (ppm) (a), number density (1/mm²) (c) and aspect ratio (e) vs. average size. The as-cast and as-rolled isothermal temperatures of 830°C, 900°C, 1000°C, and 1200°C were also examined in the T-L orientation for area fraction (ppm) (b), number density (1/mm²) (d) and aspect ratio (f) vs. average size.

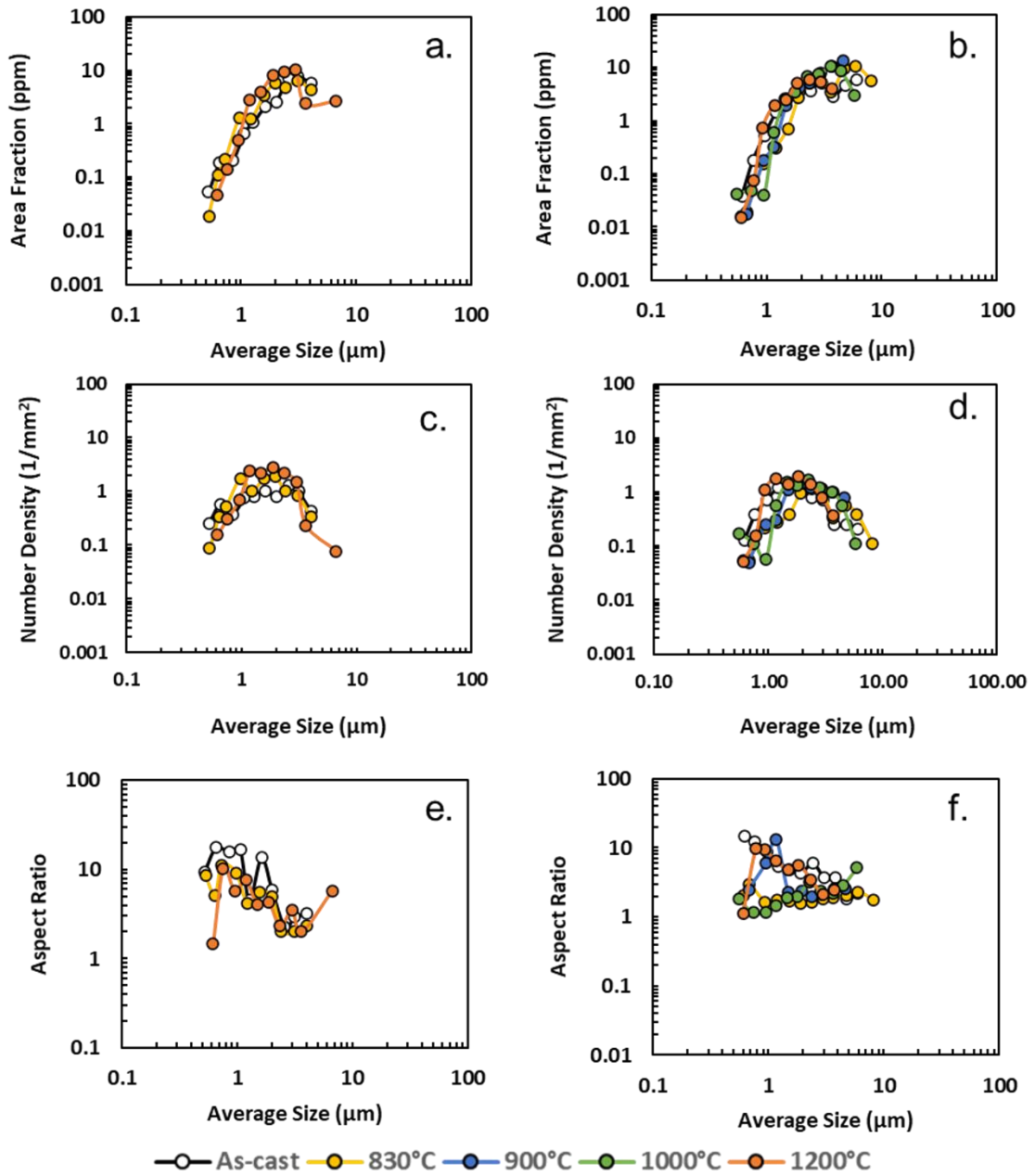


Figure 21. The average size, distribution, and aspect ratio of complex inclusions were examined from the Aspex PICA-1020 results on log-log plots. The as-cast, as-rolled 830°C, and as-rolled 1200°C were examined in the L-S orientation for area fraction (ppm) (a), number density ($1/\text{mm}^2$) (c) and aspect ratio (e) vs. average size. The as-cast and as-rolled isothermal temperatures of 830°C, 900°C, 1000°C, and 1200°C were also examined in the T-L orientation for area fraction (ppm) (b), number density ($1/\text{mm}^2$) (d) and aspect ratio (f) vs. average size.

Table 8. Average nearest neighbor distance (μm) in each condition.

Longitudinal-Short Orientation (L-S)		
Condition	Average NND (μm)	Standard Deviation (μm)
As-cast	6.9	19.4
As-rolled 830°C	9.4	17.0
As-rolled 1200°C	14.8	22.1
Transverse-Longitudinal Orientation (T-L)		
Condition	Average NND (μm)	Standard Deviation (μm)
As-cast	12.1	29.9
As-rolled 830°C	12.7	25.9
As-rolled 900°C	13.7	26.6
As-rolled 1000°C	12.1	22.4
As-rolled 1200°C	14.9	25.3

In general, an increase in the NND would be expected to be beneficial but the morphology of the inclusions can outweigh that relationship. The variation in NND between 830 and 1200 appears to be correlated with the area fraction of MnS due to the large contribution of these inclusions to the overall inclusion population. To verify the results of the AFA the cross section of the fracture surface was prepared as described in Figure 7b. BSE images of the fracture surface of the as-cast, as-rolled 830°C, and as-rolled 1200°C, are displayed in Figure 22. These 3 specimens are selected to represent the high and low temperature condition. Secondary cracking is observed in the as-cast material (Figure 22a), however it is not related to NMI from the observed image. At 830°C (Figure 22b), the MnS show strong orientation dependence in the rolling direction. The MnS shown by a red arrow near the fracture surface is quite long ($\sim 190 \mu\text{m}$), which further highlights the relationship with increased MnS content and more detrimental morphology in the 830°C sample at the same cumulative reduction. In comparison the MnS at 1200°C still show orientation dependence in the rolling direction but are finer in

comparison to the 830°C condition explained by a decrease in the MnS content. Because the recrystallization temperature is around 1000°C for this steel it is possible that the MnS morphology and anisotropy ratio is linked especially considering the material shows similar behavior at 830°C and 900°C and 1000°C and 1200°C. Perpendicular to the T-L orientation for the as-cast (Figure 22d), as-rolled 830°C (Figure 22e), and as-rolled 1200°C (Figure 22f) verify the NND results in the L-S orientation as the 1200°C sample has an observable decrease in MnS inclusions. This correlates to the decrease in area fraction of MnS at 1200°C resulting in increase in the average NND. Higher magnification images were also taken in the cross section of the L-S orientation which show the interaction between MnS inclusions and secondary cracking in the as-rolled 900°C and as-rolled 1000°C which both show evidence of initiation and propagation as a result of MnS inclusions.

At 900°C (Figure 23a) two inclusions were examined with energy dispersive spectroscopy (EDS) to verify their composition which were verified to be MnS inclusions. The secondary crack initiates at the first MnS inclusion near the fracture and propagates through the matrix transgranularly until it reaches the second MnS. The secondary crack distorts the 2nd MnS but propagation does not continue, however, the secondary cracking is perpendicular to the primary crack direction which indicates the strain induced by the MnS making it preferable for crack propagation. At 1000°C (Figure 23b) a smaller overall Type II MnS is observed, however, it has a detrimental morphology which leads to secondary crack initiation and propagation, verified through EDS. The cross section below the T-L fracture surface was also prepared as shown in

Figure 7a. The as-cast (Figure 24a) and as-rolled 1200°C (Figure 24b) show different relationships with MnS inclusions. The as-cast material shows a void that seems to have

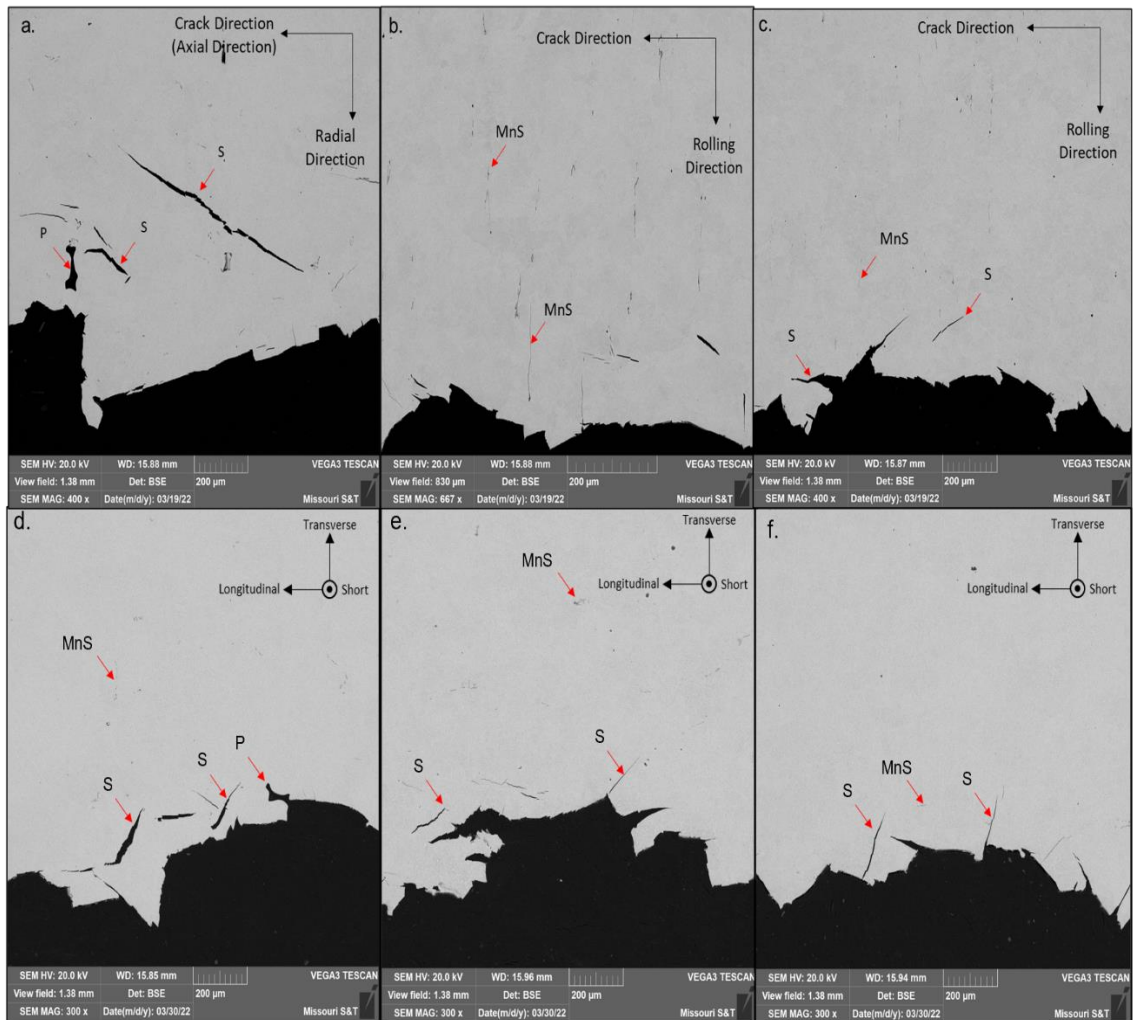


Figure 22. BSE images of a cross section of the fracture surface is depicted in Figure 2.

The as-cast imaged perpendicular to the fracture surface of the L-S (a) and T-L (d) orientation includes “S” and “P” representing secondary cracks and shrinkage pores. The as-rolled 830°C imaged perpendicular to the fracture surface of the L-S (b) and T-L (e) orientation includes “MnS” inclusions which can be seen elongated in the rolling direction. The as-rolled 1200°C imaged perpendicular to the fracture surface of the L-S (c) and T-L (f) includes “MnS” inclusions and “S” secondary cracks with elongated Type II MnS seen in the rolling direction but finer than at 830°C.

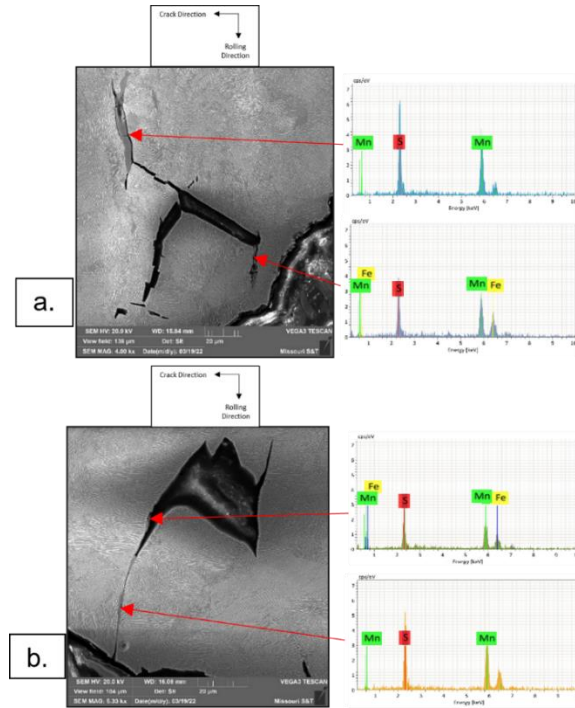


Figure 23. SE images of Type II MnS interaction with secondary cracks. The as-rolled 900°C (a) shows initiation of a secondary crack through Type II MnS which propagates transgranularly to a second MnS which cracks and debonds. The as-rolled 1000°C (b) shows initiation from Type II MnS. Of note, no evidence was observed of MnS interaction at 1200°C for the observed cross section.

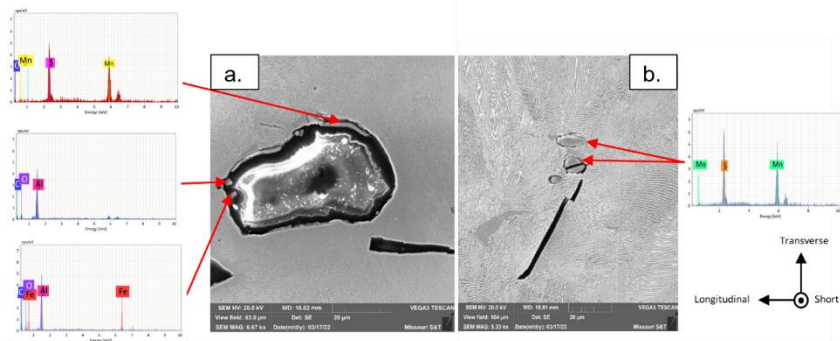


Figure 24. SE images of Type II MnS interaction with secondary cracks in the T-L cross section. The as-cast T-L bar (a) shows a large void with interaction of Type II MnS and Al₂O₃ which appear to be preferentially oriented on grain boundaries, leading to the failure. The as-rolled 1200°C (b) is depicted with secondary cracking leading to a MnS inclusion that has debonded and cracked. With respect to the orientation depicted the secondary cracking does not continue perpendicular to the crack direction as it initiated and traveled prior to interacting with the MnS.

initiated as a result of a Type II MnS inclusion and Al₂O₃ inclusions verified through EDS measurements. The as-rolled 1200°C shows the morphology of MnS inclusions which seems to have split by particle decohesion of the particle matrix. This is in line with the literature regarding void sheet coalescence.¹⁰

5. CONCLUSIONS

By examining the results of the AFA at all temperatures and comparing to NND, temperature dependence on porosity closure was evident. The trend between 830°C and 900°C in terms of pores greater than 5 µm further indicated the drawbacks of AFA for porosity analysis as the expected trend in terms of NND would indicate that the region analyzed at 830°C may have been “artificially clean” on the analyzed surface and the sample at 900°C may have been more representative for the given temperature.

Temperature dependence on coarse shrinkage porosity closure was observed from 900°C to 1200°C with 34.7 ppm decreasing to 4.5 ppm. The NND measurements further verified this relationship by indicating an increase in NND from 219.3 µm in the as-cast to 1245.6 in the as-rolled 1200°C condition. While the resolution of the CT-scan limited the correlation between the AFA and CT-scan results it was observed that ~98% of shrinkage porosity in the as-cast condition with a mean diameter greater than 15.73 µm was closed for a 66% reduction at 1000°C. The AFA extended the analysis to micro voids down to 0.5 µm indicating that ~92% of the total porosity was closed at 1000°C. Area fraction, number density, and aspect ratio were investigated for relationship with each rolling temperature. MnS inclusion average diameter seemed to be strongly

correlated with area fraction of MnS. The aspect ratio also increased proportionally with MnS content during hot rolling resulting in longer MnS stringers in the as-rolled 830°C condition verified by BSE imaging as shown in Figure 22b. Al₂O₃ had a similar composition in each sample and showed little deviation in size and distribution. Complex inclusions of MnS and Al₂O₃ displayed a dependence of aspect ratio on the area fraction of complex inclusions similar to that of MnS. Cross sections of the fracture surfaces revealed interactions between MnS inclusions and secondary cracking showing that elongated MnS inclusions initiated secondary cracks in the T-L orientation. The Type II MnS morphology was also seen to cause failure in the as-cast condition.

ACKNOWLEDGMENTS

This work was supported by Amsted Rail Company and the Peaslee Steel Manufacturing Research Center (PSMRC) at Missouri S&T and the authors would like to thank them for sponsorship and support for the Cast Pre-Form Forging project for which this publication is a part of.

APPENDIX

The volume in μm^3 versus mean diameter in μm is depicted in Figure 1 with regression analyses performed to predict their relationship. The regression formulas are represented in Equation 1 with a $R^2=0.7872$ for the as-cast condition and Equation 2 with a $R^2=0.9543$ for the as-rolled 1000°C. With “y” representing the pore volume in μm^3 and

“x” representing pore diameter in μm . Equation (1) was applied to the as-cast AFA results and Equation (2) was applied to the as-rolled 1000°C results to approximate the volume of the pores in the flat cross section. These are plotted graphically in Figure 11 where the contribution of area fraction is sorted by mean diameter.

$$y = 7.6065x^{2.3450} \quad (1)$$

$$y = 38.1091x^{2.3455} \quad (2)$$

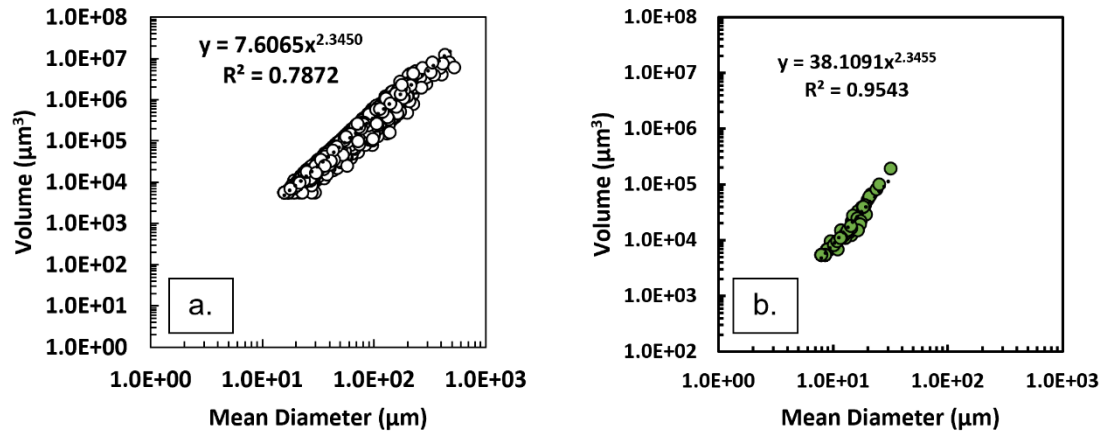


Figure 1. By plotting the mean diameter and volume of each pore from the 3D Objects Counter in Fiji for the central slice (3.2 mm height) a linear regression was fit to allow predictions of volume based on diameter.

REFERENCES

1. RAIL STEELS- DEVELOPMENTS , PROCESSING , AND USE A symposium. (2020).
2. Hardin, R. A., & Beckermann, C. (2007). Effect of porosity on the stiffness of cast steel. Metallurgical and Materials Transactions A: Physical Metallurgy and

- Materials Science, 38 A(12), 2992–3006. <https://doi.org/10.1007/s11661-007-9390-4>
3. Wang, A., Thomson, P. F., & Hodgson, P. D. (1996). A study of pore closure and welding in hot rolling process. *Journal of Materials Processing Technology*, 60(1–4), 95–102. [https://doi.org/10.1016/0924-0136\(96\)02313-8](https://doi.org/10.1016/0924-0136(96)02313-8)
 4. Ganguly, S., Wang, X., Chandrashekhara, K., Buchely, M. F., Lekakh, S., O'Malley, R. J., Bai, D., & Wang, Y. (2021). Modeling and Simulation of Void Closure during Steckel Mill Rolling for Steel Plate. *Steel Research International*, 92(2), 1–12. <https://doi.org/10.1002/srin.202000293>
 5. Kukuryk, M. (2019). Experimental and FEM analysis of void closure in the hot cogging process of tool steel. *Metals*, 9(5). <https://doi.org/10.3390/met9050538>
 6. Hardin, R. A., & Beckermann, C. (2007). Effect of porosity on the stiffness of cast steel. *Metallurgical and Materials Transactions A: Physical Metallurgy and Materials Science*, 38 A(12), 2992–3006. <https://doi.org/10.1007/s11661-007-9390-4>
 7. Dhua, S. ., Ray, A., Sen, S. K., Prasad, M. S., Mishra, K. B., & Jha, S. (1998). Influence of Nonmetallic Inclusion Characteristics on the Mechanical Properties of Rail Steel. *Journal of Allergy and Clinical Immunology*, 130(2), 556. <http://dx.doi.org/10.1016/j.jaci.2012.05.050>
 8. Grigorovich, K. V., Trushnikova, A. S., Arsenkin, A. M., Shibaev, S. S., & Garber, A. K. (2006). Structure and metallurgical quality of rail steels produced by various manufacturers. *Russian Metallurgy (Metally)*, 2006(5), 427–438. <https://doi.org/10.1134/S0036029506050107>
 9. Douglas, D., White, C. V., & McHenry, T. (2021). Failures Related to Hot Forming Processes. *Analysis and Prevention of Component and Equipment Failures*, 11, 229–240. <https://doi.org/10.31399/asm.hb.v11a.a0006835>
 10. Spitzig, W. A. (1983). EFFECT OF SULFIDES AND SULFIDE MORPHOLOGY ON ANISOTROPY OF TENSILE DUCTILITY AND TOUGHNESS OF HOT-ROLLED C-Mn STEELS. *Metallurgical Transactions. A, Physical Metallurgy and Materials Science*, 14 A(2), 471–484. <https://doi.org/10.1007/bf02644224>
 11. Da Costa E Silva, A. L. V. (2019). The effects of non-metallic inclusions on properties relevant to the performance of steel in structural and mechanical applications. *Journal of Materials Research and Technology*, 8(2), 2408–2422. <https://doi.org/10.1016/j.jmrt.2019.01.009>

12. Moore and Bodor, “Steel deoxidation practice: Special emphasis on heavy section steel castings”, AFS Transactions, 93, 99-114 (1985).
13. Singh, V., Lekakh, S., & Peaslee, K. (2008). Using Automated Inclusion Analysis for Casting Process Improvements. SFSA Technical and Operating Conference, Steel Founders’ Society of America (SFSA), May, 1–18.
http://scholarsmine.mst.edu/post_prints/pdf/TO_08_MSTInclusions_09007dcc805d93e9.
14. Tanaka, Y., Pahlevani, F., & Sahajwalla, V. (2018). Agglomeration behavior of non-metallic particles on the surface of Ca-treated high-carbon liquid steel: An in situ investigation. *Metals*, 8(3). <https://doi.org/10.3390/met8030176>
15. Hurtuk, D. J. (2018). Steel Ingot Casting. *Casting*, 911–917.
<https://doi.org/10.31399/asm.hb.v15.a0005295>
16. Jacot, A., & Gandin, C.-A. (2018). Formation of Microstructures, Grain Textures, and Defects during Solidification. *Metals Process Simulation*, 22, 214–227.
<https://doi.org/10.31399/asm.hb.v22b.a0005518>
17. Maciejewski, J. (2015). The Effects of Sulfide Inclusions on Mechanical Properties and Failures of Steel Components. *Journal of Failure Analysis and Prevention*, 15(2), 169–178. <https://doi.org/10.1007/s11668-015-9940-9>

III. HIGH TEMPERATURE JOHNSON-COOK STRENGTH OF A HIGH CARBON STEEL

Jacob M. Summers, Mario F. Buchely, Laura N. Bartlett, Ronald J. O'Malley

Department of Materials Science and Engineering, Missouri University of Science and Technology, Rolla MO 65409, USA.

Richard Pilon

Amsted Rail Company, Overland Park, KS, USA.

Nicolas Poulain

TRANSVALOR AMERICAS, Chicago, IL, USA

ABSTRACT

The use of finite element analysis to solve complicated industrial problems including hot rolling and ring rolling at elevated temperatures is important to industrial processing. To understand material behavior at elevated temperatures, the Johnson Cook strength material model has been used to fit results from hot tensile testing and as the framework for a Finite Element Analysis complex ring-rolling model. Hot tensile tests were performed at 830°C, 900°C, 1000°C, and 1200°C, at strain rates of 0.1 s⁻¹, 1.0 s⁻¹, 5.0 s⁻¹, and 10.0 s⁻¹. These temperatures were based on experimental hot rolling trials under plane strain conditions performed isothermally. The strain rates selected were selected to encompass the strain rates observed during hot rolling with 0.1 s⁻¹ and 1.0 s⁻¹ included to allow material behavior to be predicted upon contact and lower strain rate conditions to ensure dynamic simulation of the full process. The model was prepared in the Forge NxT software to simulate an industrial wheel-rolling operation.

1. INTRODUCTION

Out of a need to reduce the amount of laboratory testing needed to understand material behavior during high velocity impact and explosive detonation, Johnson & Cook¹ developed a constitutive model based on high temperature tensile tests and true stress-true strain data.¹ This relationship is shown in Equation (1).

$$\sigma_{eff} = (A + B\varepsilon_{pl}^n) \left(1 + C \ln \left(\frac{\varepsilon_{pl}^*}{\varepsilon_o^*} \right) \right) \left(1 - \left(\frac{T - T_r}{T_m - T_r} \right)^m \right) \quad (1)$$

This formula relates the effective stress (σ_{eff}) as a function of the plastic strains (ε_{pl}), plastic strain-rates (ε_{pl}^*), strain rate of reference (ε_o^*), reference temperature in Kelvin (T_r) and melting temperature in Kelvin (T_m). A, B, n, C, and m are constants which are obtained empirically. They showed for 12 materials that this model held true. This model is based on strain hardening, strain-effects, and thermal softening. Schwer² adjusted this relationship by tweaking an assumption made in the Johnson Cook model ($\varepsilon_o^*=1 \text{ s}^{-1}$) which was shown to underpredict real bi-linear material behavior and demonstrated that the strain rate of reference (ε_o^*) should reflect material behavior and be included as an additional variable in the regression.² Buchely et. al.³ utilized the technique proposed by Johnson & Cook¹ using the correction proposed by Schwer² by allowing the strain rate of reference to be an additional empirically derived constant. Using a Genetic-Algorithm in Matlab, true stress-true strain data was fit to the formula for the Johnson-Cook Strength model with high accuracy for as-cast 15V48 steel ($R^2=0.97$).³ Therefore, these techniques will be employed in this work to determine the Johnson-Cook Strength parameters for

AISI 1070 steel for development of a Finite Element Analysis (FEA) model of the wheel rolling process.

Typical test windows for this testing targets the temperature range of 900-1200°C as these are considered the typical formability windows of steels and were observed in the previous studies mentioned.^{1,2,3} These temperatures are selected based on the recrystallization temperature and the austenite window for general steels. In the case of AISI 1070 steel, the A3 plus ~50°C is 830°C which was examined as well for comparison as it has been shown in previous work to lead to fine grained products after hot rolling AISI 1070 steel isothermally. Therefore, a temperature range of 830-1200°C is observed in this study to determine the Johnson-Cook Strength model and determine the behavior for thermomechanical process conditions.

Industrial wheel rolling is a process in the forging production process for heavy haul wheels which involves expansion of the overall diameter of the wheel through use of a complicated rolling mill with a variety of rollers used to both stabilize the wheel and drive reduction. The fundamental work in literature relating to processing and modeling these systems begin with simplified ring rolling operations. When attempting to accurately mesh the parts without initiating long computational times, different mathematical models have been used including Lagrangian and Euler methods. Lagrangian FE codes were found to be inefficient as the sole meshing technique due to the high density meshing while pure Eulerian methods were found to fail to accurately capture evolving geometry.¹¹ Work by Davey and Ward showed that an Arbitrary Lagrangian and Euler (ALE) method could render useful 3D models with low computation time.¹¹ Work conducted by Shen et al.⁸ aimed to model a traditional wheel

rolling operation with reduction in the rim profile and increase in the overall wheel diameter being the main targets using ALE. Their model accurately simulated experimental testing for the rim profile variations along with a variety of small deviations in the wheel during rolling. Simulations have also been run increasingly with the use of commercial software such as Simufact Forging, ABAQUS, and FORGE which allow the ability to model complex parts with lower computational and development times. The aim of this work is to implement the Johnson-Cook Strength model into an adapted wheel rolling process to simulate the process as a proof-of-concept for industrial application of a new product line.

2. MATERIALS AND METHODS

Samples were prepared from as-cast samples of thickness of ~3 inches and were machined using a CNC lathe according to ASTM E21-20 and E8 specifications.^{5,6} A steel heat was melted using the electric arc furnace, EAF, process in a commercial foundry from corporate sponsors. The steel was fully killed (Mn, Si, and Al) and the resulting melt was transferred to a ladle. The steel was cast into semi-permanent graphite molds using pressure pouring technology. The as-cast material which conforms to AAR specifications has a chemistry displayed in Table 1 which were obtained from the as-cast material in the bulk web section through optical emission spectroscopy and LECO combustometric analysis for C and S content. Samples prepared for hot tensile testing are displayed in Figure 1a along with the MTS hydraulic load frame used to test the specimens (Figure 1b). The specimen is held by two grips as shown. The sample threads

are protected from welding to the grips using a mixture of Yttria and acetone to create a ceramic slurry. The furnace with SiC elements is used to heat the samples. The sample was protected by an Ar environment to prevent oxidation of the samples. A Linear Variable Differential Transformer (LVDT) was utilized as shown in Figure 1b which tracks the linear displacement during tensile testing at a rate of 1024 Hz. The heat treatment profile of each sample is given in Figure 2. This shows that four isothermal temperatures were investigated, 830°C, 900°C, 1000°C, and 1200°C. The specimens were heated to temperature, once all controllers were stable at the desired temperature, they were held for 10 minutes, followed by testing at the desired strain rate, and being allowed to cool slowly after testing. The displacement and force data were collected and rendered in Engineering Stress-Strain curves and then converted to True Stress-Strain curves using the following formulas in Equation (2) and Equation (3).

$$\varepsilon = \ln(1 + e) \quad (2)$$

$$\sigma_{true} = \sigma_{eng}(1 + e) \quad (3)$$

where e is engineering strain, ε is true strain, σ_{eng} is engineering stress, and σ_{true} is true stress. The strain to failure (ε^f) was also calculated based on the SEM images of the fracture surfaces which is calculated based on Equation (4) where A_0 is the initial cross-sectional area and A_f is the final cross-sectional area.

$$\varepsilon^f = \ln\left(\frac{A_0}{A_f}\right) \quad (4)$$

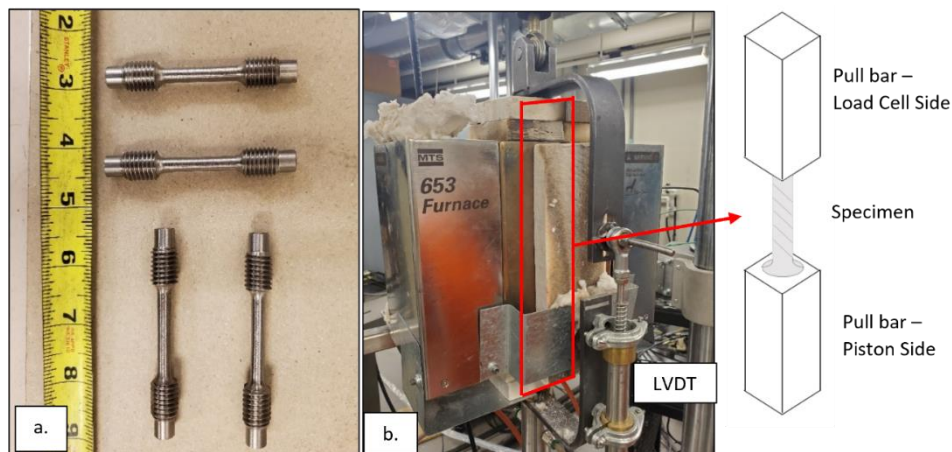


Figure 1. Depicted are the hot tensile samples (a) and the MTS hydraulic load frame and a depiction of the grip configuration (b).

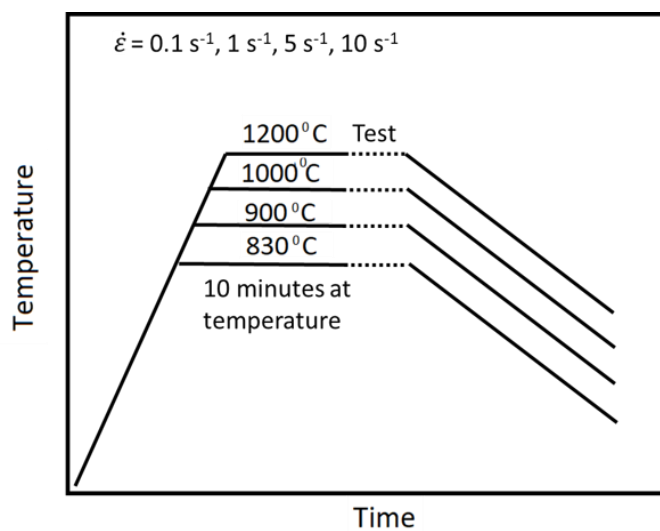


Figure 2. The treatment profile for hot tensile testing of as-cast samples.

Table 1. Composition of the Association of American Railroads (AAR) grade steel.

C*	Si	Mn	Cu	Cr	Mo	Ni	P	S*	Nb	Al	Ti	Fe
0.706	0.53	0.73	0.168	0.13	0.025	0.048	0.004	0.021	0.004	0.002	0.0008	Bal.

* Concentrations of sulfur and carbon were determined utilizing LECO combustometric analysis

3. RESULTS AND DISCUSSION

The results of hot tensile testing are displayed in Figure 3 which includes the engineering stress-strain and true-stress strain curves calculated by Equation 2. As expected, the lower the test temperature the higher the yield strength (YS) and ultimate tensile strength (UTS). By comparing the 0.1 s^{-1} strain rate (Figure 3a) to 10 s^{-1} (Figure 3d), it can also be seen that the tensile properties increase with increasing strain rate. In Figure 3d, it can also be seen that the curve is less stable than the other conditions. A high strain rate of 10 s^{-1} results in rapid elongation and failure and thus fewer data points, however, despite slight fluctuations in the curves, the sampling rate is appropriate to obtain the YS and UTS effectively. These results are further summarized in Table 2. To represent the trends in Figure 3a-d numerically, the 830°C isothermal condition increases from a UTS of 114.4 MPa to 209.1 MPa with increased strain rate of 0.1 s^{-1} to 10 s^{-1} . Testing at the 1200°C isothermal condition results in an increase in the UTS of 34.0 MPa to 67.4 MPa with an increase in the strain rate of 0.1 s^{-1} to 10 s^{-1} . The 1200°C condition maintains a UTS that is $\sim 31\%$ below the 830°C condition for all strain rates. Tabulated also are the strain to failure calculations from Equation 3. Fracture surfaces were examined by SEM Fractography on the Tescan Vega3 and post processed in Fiji as shown in Figure 4. These are four representative sample surfaces at the extreme temperatures and strain rates with 830°C at a strain rate of 0.1 s^{-1} (Figure 4a) and 10 s^{-1} (Figure 4c), and 1200°C at a strain rate of 0.1 s^{-1} (Figure 4b) and 10 s^{-1} (Figure 4d). The differences in final area are evident when examining the fracture surfaces. Higher magnification images are depicted in Figure 5a-d. 830°C at a strain rate of 0.1 s^{-1} is

depicted in Figure 5a with micro voids labeled as “V” and dimples labeled as “D”. The surface of the 1200°C at a strain rate of 0.1 s^{-1} is so small that it is not possible to delineate any particular features of the fracture surface. However, at a strain rate of 10 s^{-1} , the 830°C (Figure 5c) and 1200°C (Figure 5d) tensile fracture surfaces are more comparable and are each labeled with micro voids “V” and dimples “D”. Because these samples are taken from the as-cast condition, the voids are present and widespread in both samples but at 1200°C, the size of the voids are much larger. The dimples in the 830°C are also more easily discernible in a seemingly dendritic structure with the 1200°C dimples having an appearance that more closely resembles cleavage with greater size correlating to the larger grain size. However, these samples are not etched and therefore no direct correlations can be made about specific microstructural features. Figure 6 illustrates the relationship between accumulated damage and temperature at different strain rates. The lower the temperature the higher the damage and therefore the larger the strain to failure for a given strain rate.

Buchely et. al³ programmed a Genetic-Algorithm optimization process in MATLAB toolbox. This approach was used in this work to adjust the true stress-strain data to the Johnson Cook Strength model (Equation 1).³ The strain-rate of reference was also included as a material parameter in conjunction with the findings of Schwer.² The results of the fit to the true stress-true strain data are displayed in Figure 7. A summary of the resulting variables is shown in Table 3.

The Johnson-Cook Strength model was implemented as a framework for FEA modeling of a wheel rolling simulation for industrial cast pre-form rolling. A schematic drawing detailing the rolling mill configuration is shown in Figure 8. The mill

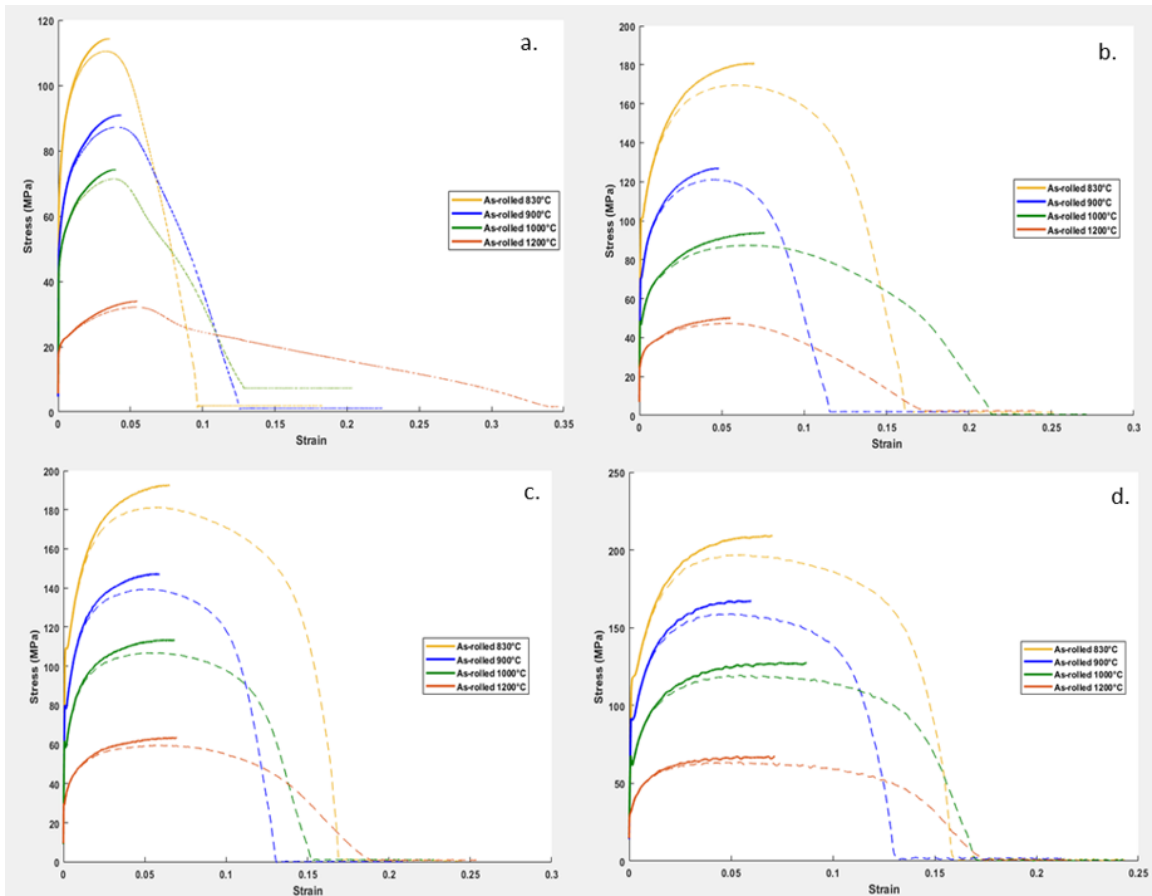


Figure 3. Engineering Stress-Strain curves and True Stress-Strain curves superimposed on the same plot. The dashed lines indicate the engineering-stress strain curves and solid lines indicate the true stress-strain curves. Each temperature is included in each plot with each representing a different strain rate, 0.1 s^{-1} (a), 1 s^{-1} (b), 5 s^{-1} (c), 10 s^{-1} (d).

configuration includes web rollers which are the only drive rolls (Figure 8d), the back roll (Figure 8e), which contours the rim profile, and the support rollers which include two edging rollers (Figure 8b), two guide rolls (Figure 8c), and two centering rolls (Figure 8a). Traditional wheel rolling in the forging process for railway wheels is primarily targeting the expansion of the overall wheel diameter along with minor reduction of the rim thickness.⁸ The process of determining an optimal route for modeling the wheel rolling process has also been described as engineering trial and error.

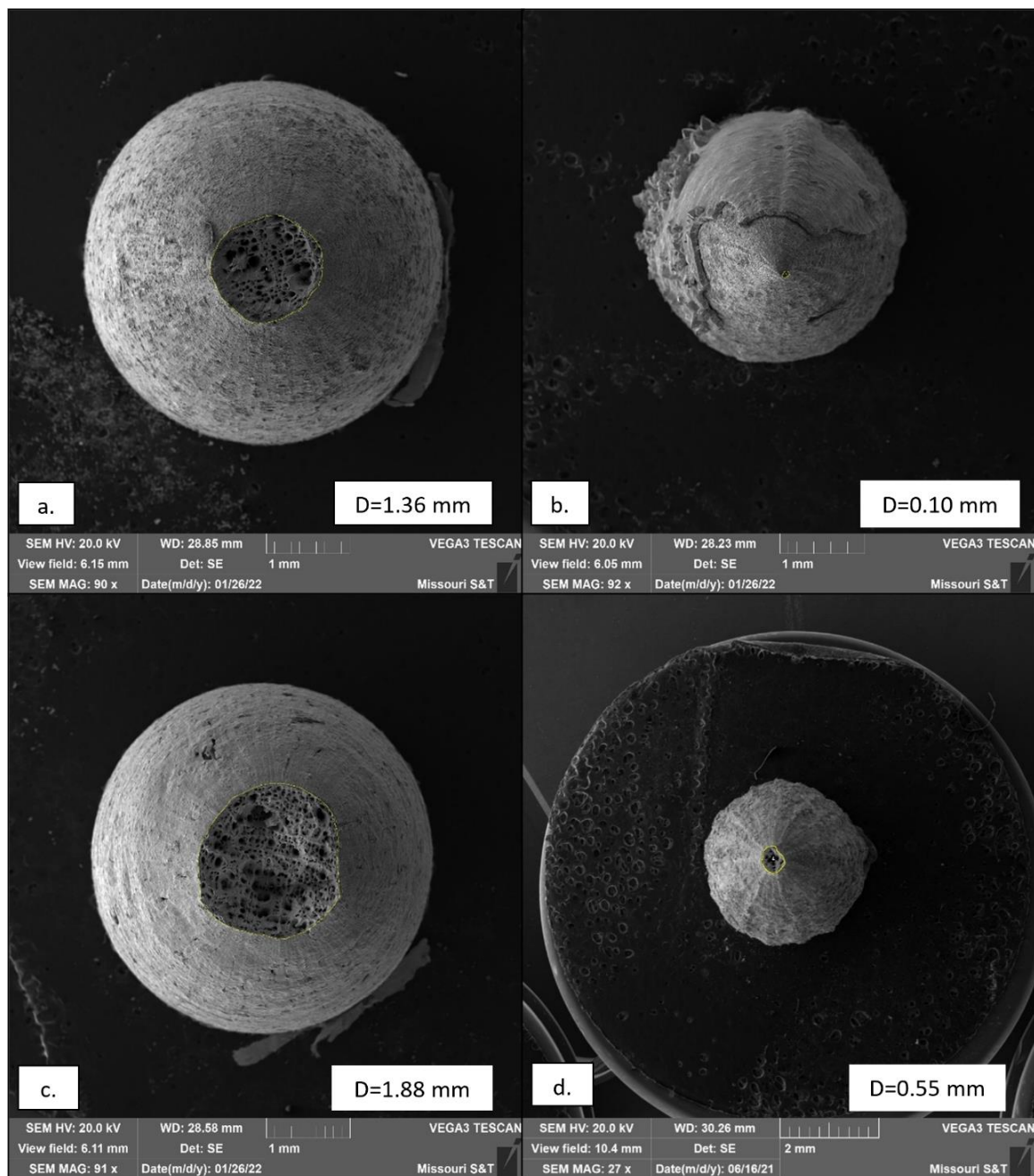


Figure 4. Four representative fracture surfaces of the hot tensile samples from SEM fractography with the fracture surface measured by feret diameter in Fiji. 830°C at a strain rate of 0.1 s^{-1} (a), 1200°C at a strain rate of 0.1 s^{-1} (b), 830°C at a strain rate of 10 s^{-1} (c), 1200°C at a strain rate of 10 s^{-1} (d).

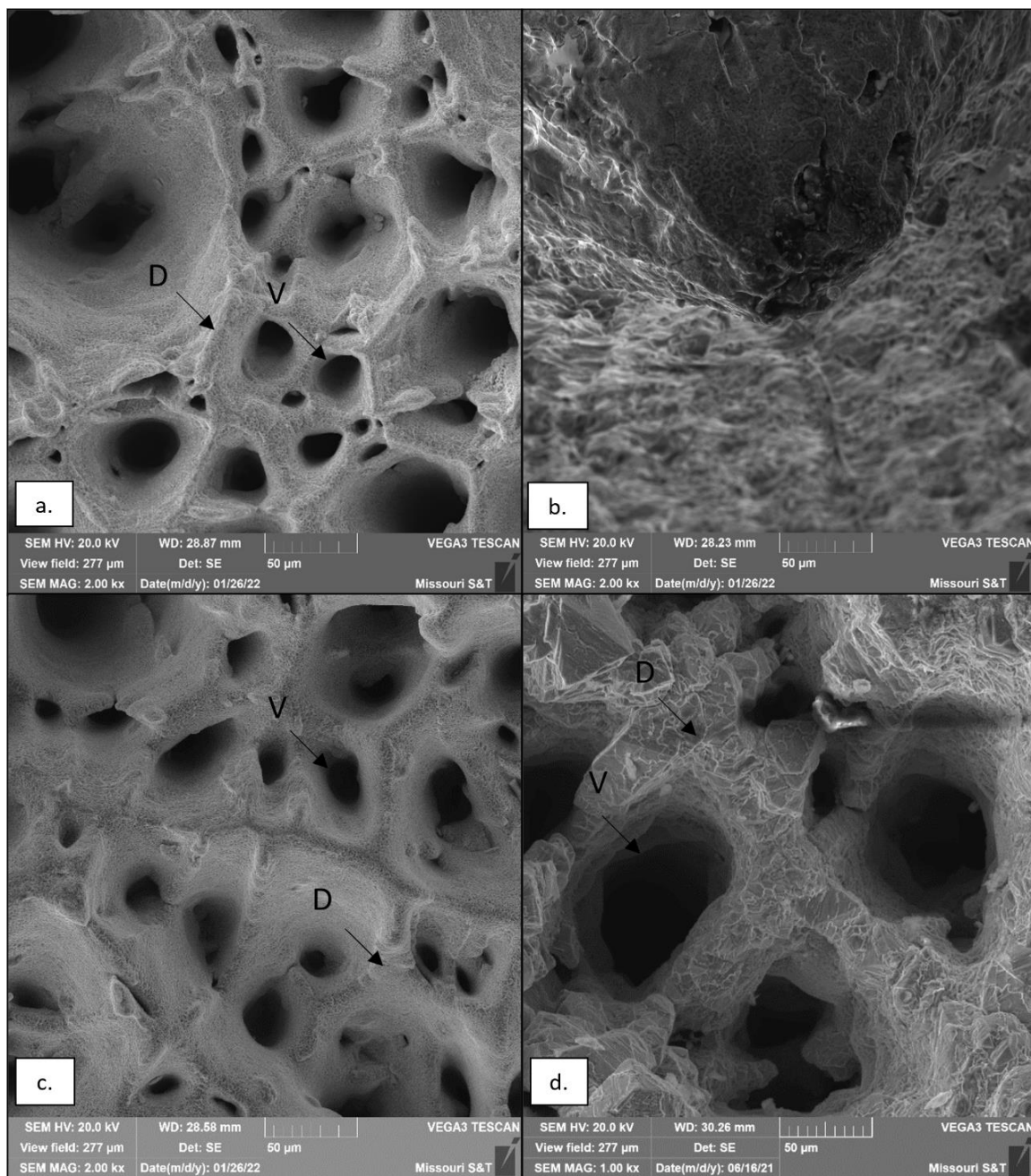


Figure 5. Higher magnification images of the 830°C at a strain rate of 0.1 s^{-1} (a), 1200°C at a strain rate of 0.1 s^{-1} (b), 830°C at a strain rate of 10 s^{-1} (c), 1200°C at a strain rate of 10 s^{-1} (d). Two primary features identified are labeled by “V” for voids and “D” for dimples.

Table 2. A summary of the tensile properties for each temperature condition under each strain rate (s^{-1}).

Condition	Strain Rate (s^{-1})	Yield Strength (MPa)	UTS (MPa)	Elongation	ϵ_f
830°C	0.1	66.4	114.4	0.19	3.1
900°C	0.1	50.1	91.0	0.22	2.9
1000°C	0.1	43.3	72.5	0.20	2.5
1200°C	0.1	17.0	34.0	0.36	2.4
830°C	1	101.2	180.7	0.25	4.2
900°C	1	70.4	126.9	0.20	3.7
1000°C	1	47.7	93.7	0.25	3.1
1200°C	1	24.9	50.0	0.24	2.7
830°C	5	108.5	192.6	0.25	4.8
900°C	5	80.1	147.2	0.21	3.9
1000°C	5	60.5	113.3	0.23	3.8
1200°C	5	29.4	63.5	0.25	3.3
830°C	10	115.4	209.1	0.25	8.4
900°C	10	91.8	167.2	0.21	6.8
1000°C	10	67.4	127.3	0.24	5.8
1200°C	10	29.9	67.4	0.22	4.8

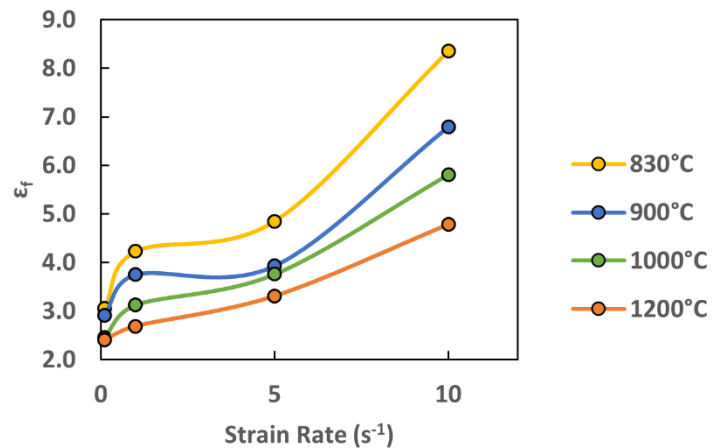


Figure 6. Strain to failure versus strain rate which demonstrates the accumulation of damage at higher strain rates which is enhanced as temperature decreases.

Therefore, several models were run with different assumptions and roller configurations before settling on this configuration to run in the Forge NxT software. As mentioned, the traditional movement in the rolling stage of the wheel forging process involves the rim and diameter primarily.

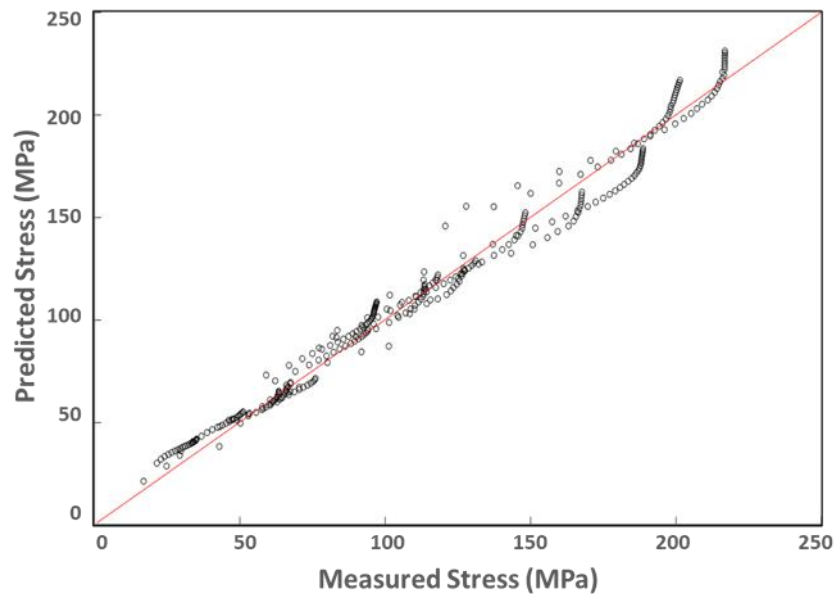


Figure 7. Johnson-Cook Strength model fit to true stress-true strain data from 830°C to 1200°C with a strain rate of 0.1 s⁻¹ to 10 s⁻¹. The R² of the linear regression is 0.983 showing high accuracy of the fit.

Table 3. Johnson Cook Parameters determined between 830°C and 1200°C at 0.1 to 10 s⁻¹ through 10 iterative runs of a Genetic Algorithm programmed in Matlab. The run with the lowest error was selected and is displayed below with the selected run having 1,439 computational steps.

Condition	$\sigma_{eff} = (A + B\varepsilon_{pl}^n)(1 + C \ln\left(\frac{\varepsilon_{pl}^*}{\varepsilon_0^*}\right))(1 - \left(\frac{T - T_r}{T_m - T_r}\right)^m)$					
As-cast AAR Steel	A [MPa]	B [MPa]	n	C	m	ε_0^* [s ⁻¹]
	62.254	118.805	0.288	0.158	0.640	0.079

In this case, it was desirable to deform the material in the web section to induce local plastic deformation with the aim of initiating dynamic recrystallization, reducing the as-cast grain size, and closing shrinkage porosity as these features have been shown to be detrimental for Charpy properties. The movement of the web roller for the following simulation is shown in Figure 8. The web rollers are designed to uniformly reduce the

thickness in the web section of the wheel from 64.77 mm to 31.75 mm to meet AAR specifications as shown in Figure 9.⁹

The resulting model rendered in the Forge NxT software is given in Figure 10 which shows that a central mandrel was also added to stabilize the wheel for simulation and prevent deformities in the hub. This was done to simplify the model but can also be implemented in conventional wheel rolling mills and therefore does not reduce the feasibility of the process. Utilizing JMatPro material data for recrystallization, behavior of the material information after wheel rolling regarding the ASTM, grain size can be estimated based on the starting grain size of the material which has been estimated to be between Macro Size M-10.5 and M-11.0.¹⁰ Displayed in Figure 11 is the expected grain size seven seconds into the simulation in a cross section of the wheel. As mentioned, the plastic deformation is localized to the web section of the wheel. Small amounts of deformation as a result of contact friction between the web rollers and the back roll results in small fluctuations in grain size in the rim. However, this area is not targeted primarily for reduction in the following model. Along with information about grain size, the triaxiality stresses were also observed in the cross section of the wheel seven seconds into the simulation as depicted in Figure 12. The resulting triaxiality stress in the web section can be seen throughout the wheel profile. behavior of the material information after wheel rolling regarding the ASTM, grain size can be estimated based on the starting grain size of the material which has been estimated to be between Macro Size M-10.5 and M-11.0.¹⁰ Displayed in Figure 11 is the expected grain size after rolling is completed in a cross section of the wheel. As mentioned, the plastic deformation is localized to the web

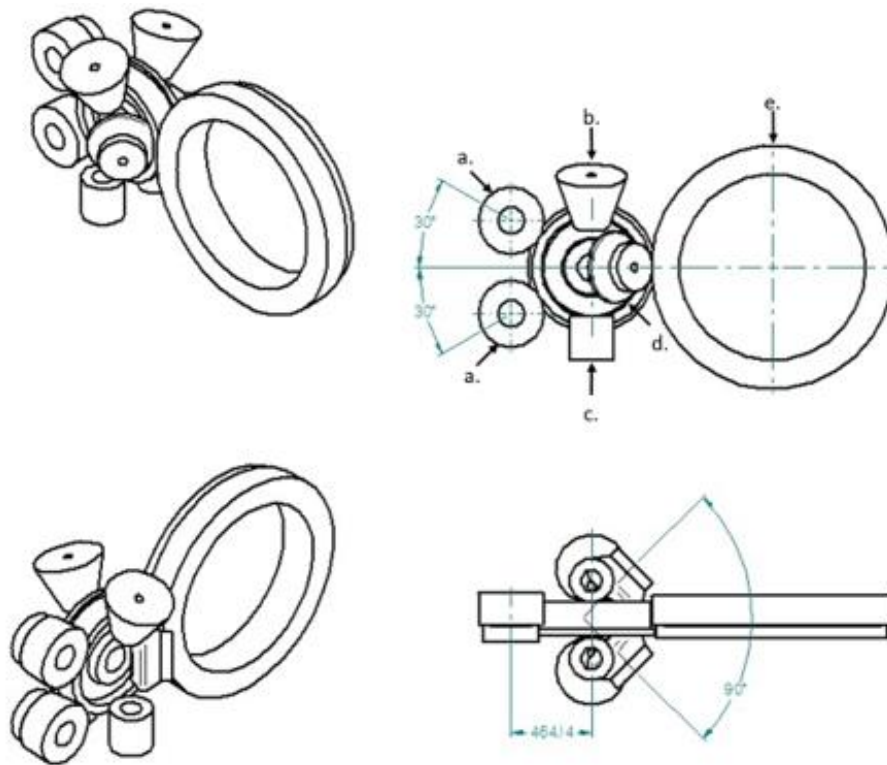


Figure 8. Schematic drawing of wheel rolling mill design for FEA modeling. The mill is composed of centering rolls (a), edging rolls (b), guide rolls (c), web rolls (d), and the back roll (e).

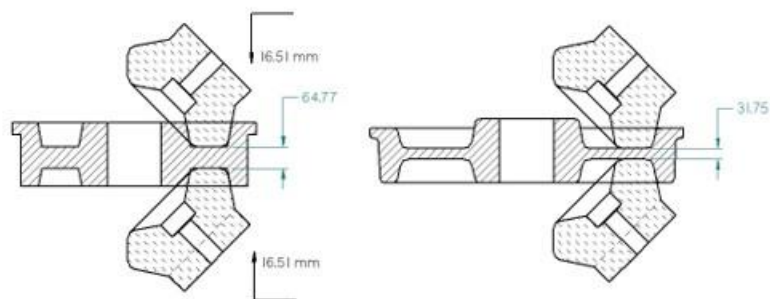


Figure 9. A cross section of the wheel assembly that shows the movement of the web rollers to induce plastic deformation in the web section of the wheel.

section of the wheel. Small amounts of deformation as a result of contact friction between the web rollers and the back roll results in small fluctuations in grain size in the rim. However, this area is not targeted primarily for reduction as the intended treatment profile will result in hardening of the rim surface making grain size less important in terms of industrial processing. Along with information about grain size, the triaxiality stresses were also observed in the cross section of the wheel at the end of the simulation in Figure 12. The resulting triaxiality stress in the web section can be seen throughout the wheel profile.

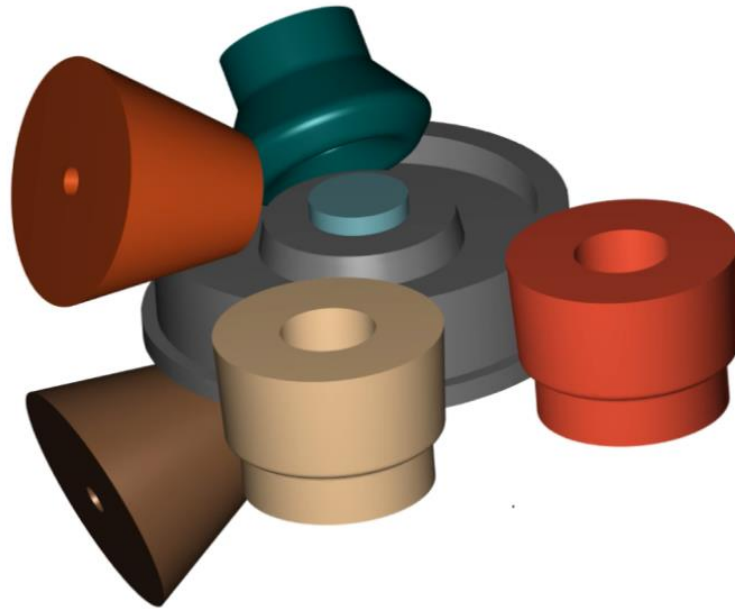


Figure 10. Schematic of wheel rolling model in Forge NxT.

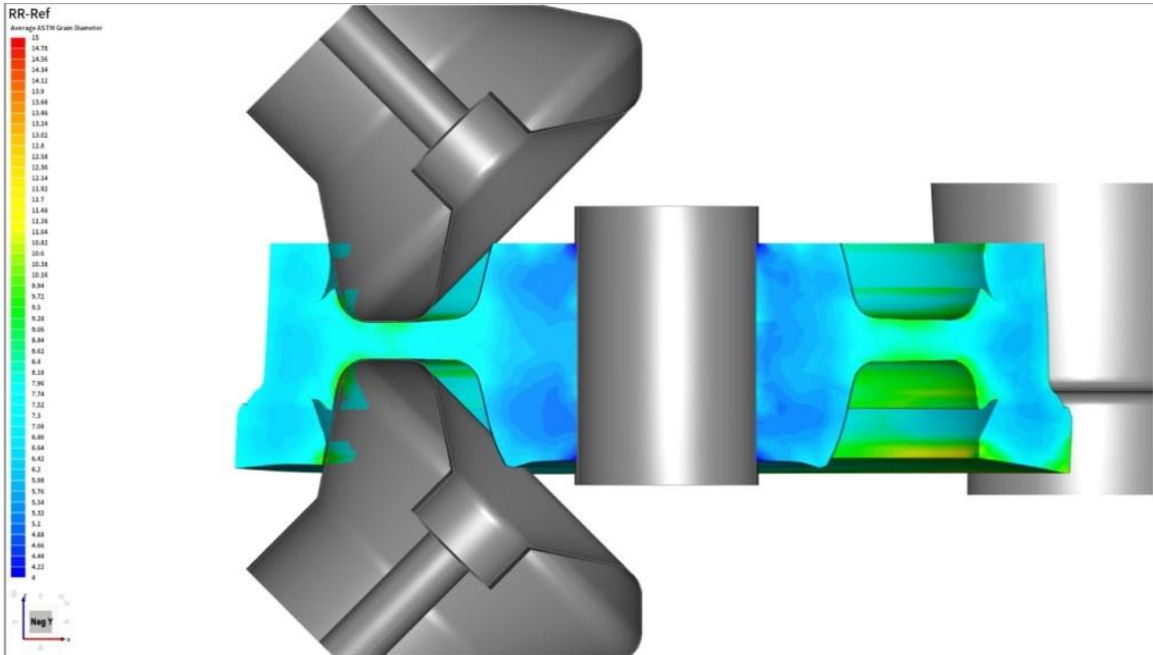


Figure 11. Cross section of the wheel model in Forge NxT for grain size at seven seconds.

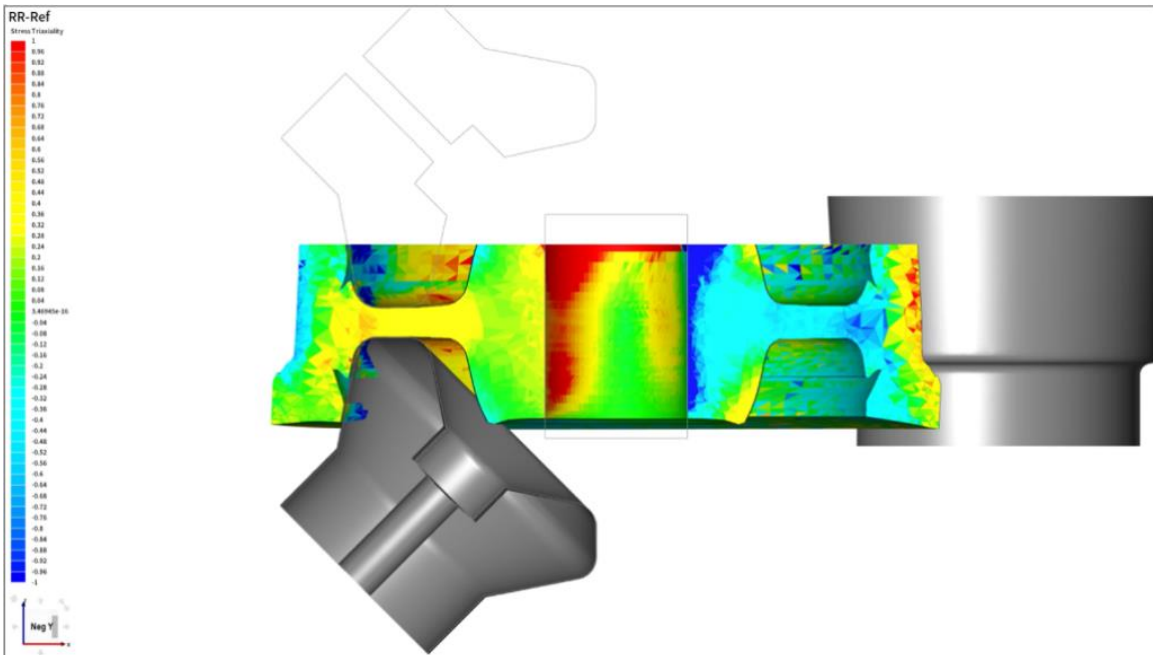


Figure 12. Cross section of the wheel model in Forge NxT for triaxiality stress at seven seconds.

Along with internal stresses and properties of the material, the mill response to this process is also important to determine the feasibility for industrial application. The tonnage on the web rolls is given in the X direction (Figure 13) and Z direction (Figure 14). The forces in the X-direction of the web rolls is observed in Figure 13 which show that the maximum force reached in the X-direction during simulation is ~45 tonnes. Figure 14 shows that the force in the Z-direction on the web rollers peaks just above that of the X-direction at ~47 tonnes with the edging rolls experiencing forces of ~40 tonnes at the maximum.

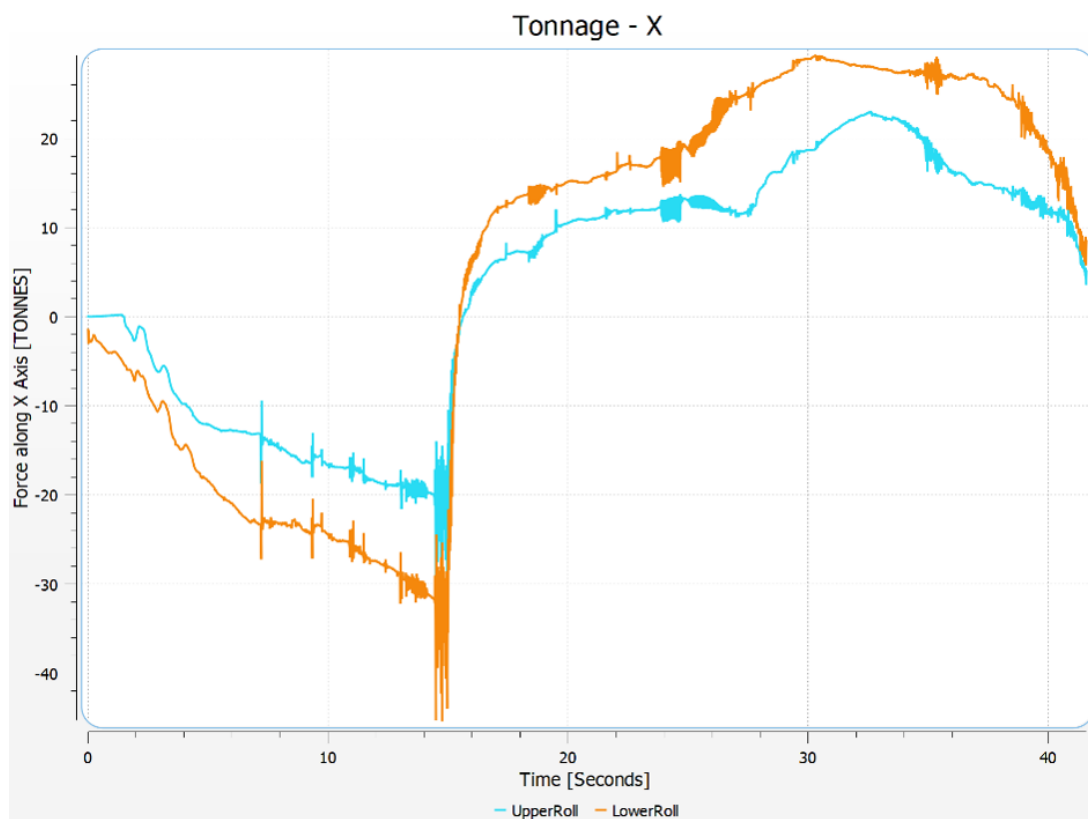


Figure 13. The tonnage on the web rolls (upper and lower rolls) for the X direction.

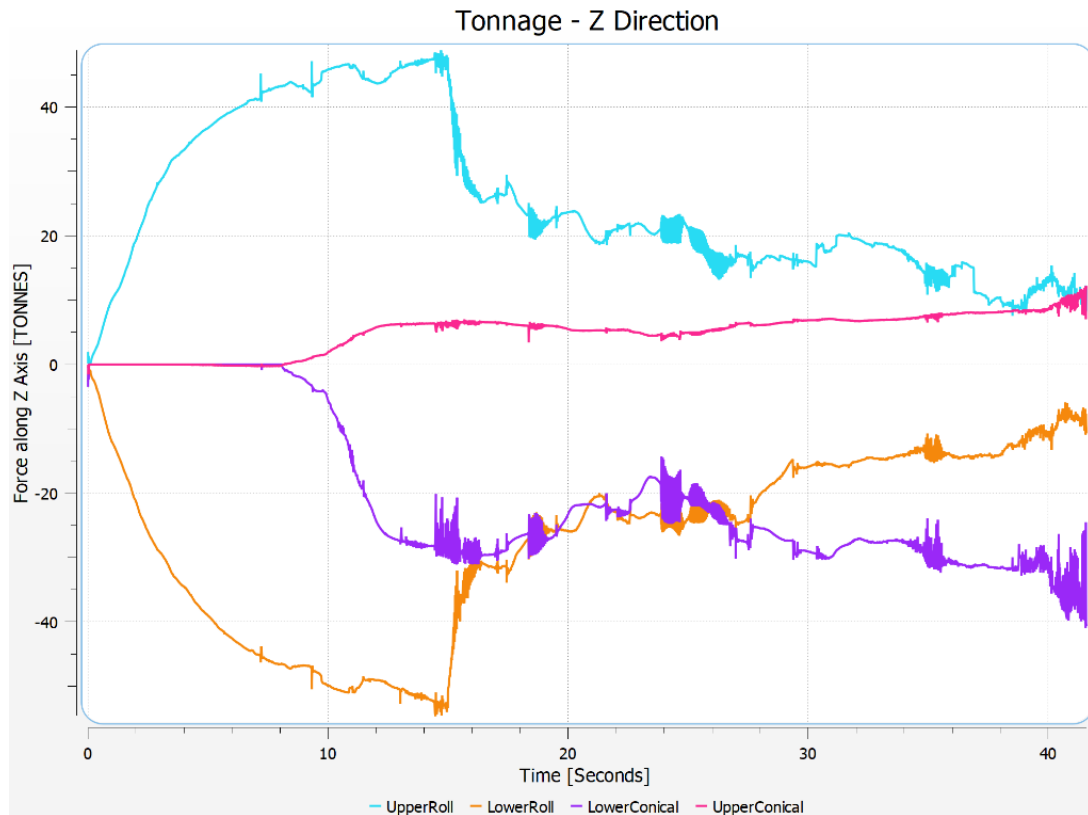


Figure 14. The tonnage on the web rolls (upper and lower rolls) and the tonnage on the edging rolls (upper and lower conical rolls).

4. CONCLUSIONS

In conclusion, the Johnson-Cook Strength model was developed based on the hot tensile properties gathered between 830°C and 1200°C and strain rates of 0.1 and 10 s⁻¹ and showed good agreement with experimental data. This, along with JMatPro material information for dynamic recrystallization, was used to develop a FEA model for a modified wheel rolling process for industrial application using the existing body of literature and minimal engineering trial and error. Simulation of the process resulted in

information about predicted final grain size, triaxiality stresses, and roller forces allowing for a better understanding of the viability of the proposed industrial process.

ACKNOWLEDGMENTS

This work was supported by Amsted Rail Company and the Peaslee Steel Manufacturing Research Center (PSMRC) at Missouri S&T and the authors would like to thank them for sponsorship and support for the Cast Pre-Form Forging project for which this publication is a part of. Special thanks to Dr. Mario Buchely and Nicolas Poulain from Transvalor for their invaluable assistance with the FEA modeling of the wheel rolling process.

REFERENCES

1. Johnson, G. R., & Cook, W. H. (1983). A Computational Constitutive Model and Data for Metals Subjected to Large Strain, High Strain Rates and High Pressures. The Seventh International Symposium on Ballistics, 541–547.
2. Schwer, L. (n.d.). Optional Strain-Rate Forms for the Johnson Cook Constitutive Model and the Role of the Parameter ϵ_0 AUTHOR Len Schwer Keywords parameter ϵ . 6th European LS-DYNA Users' Conference.
3. Buchely, M., Aken, D., O'Malley, R., Lekakh, S., & Chandrashekhara, K. (2018). Hot Rolling Effect upon the High Temperature Johnson-Cook Strength and Failure Models for a 15V38 Grade Steel. 1045–1053.
https://doi.org/10.7449/2017/mst_2017_1045_1053
4. Hosford, W.F. and R.M. Caddell, Metal forming: mechanics and metallurgy. 2011: Cambridge University Press.

5. ASTM E8. (2010). ASTM E8/E8M standard test methods for tension testing of metallic materials 1. Annual Book of ASTM Standards 4, C, 1–27. <https://doi.org/10.1520/E0008>
6. ASTM International. (2006). ASTM E21-20: Standard Test Methods for Elevated Temperature Tension Tests of Metallic Materials. i, 1–24. <https://doi.org/10.1520/E0021-20.2>
7. Matlab, Global Optimization Toolbox, User's Guide. 2015, MathWorks INC.
8. Shen, X., Yan, J., An, T., Xu, Z., & Zhang, J. (2014). Analysis of railway wheel rolling process based on three-dimensional simulation. *International Journal of Advanced Manufacturing Technology*, 72(1–4), 179–191. <https://doi.org/10.1007/s00170-014-5637-6>
9. Technical, A. A. R., Division, S., Committee, W., & Qualification, A. B. (2013). M-107/M-208 Standard: Wheels, Carbon Steel. 1–42.
10. INTERNATIONAL, A. (2010). Standard Test Methods for Determining Average Grain Size. *Astm E112-10*, 1–27. <https://doi.org/10.1520/E0112-13.1.4>
11. Davey, K., & Ward, M. J. (2002). A practical method for finite element ring rolling simulation using the ALE flow formulation. *International Journal of Mechanical Sciences*, 44(1), 165–190. [https://doi.org/10.1016/S0020-7403\(01\)00080-7](https://doi.org/10.1016/S0020-7403(01)00080-7)
12. Molinari, A., Jacques, N., Mercier, S., Leblond, J. B., & Benzerga, A. A. (2015). A micromechanical model for the dynamic behavior of porous media in the void coalescence stage. *International Journal of Solids and Structures*, 71, 1–18. <https://doi.org/10.1016/j.ijsolstr.2015.05.003>
13. Pineau, A., Benzerga, A. A., & Pardoën, T. (2016). Failure of metals I: Brittle and ductile fracture. *Acta Materialia*, 107, 424–483. <https://doi.org/10.1016/j.actamat.2015.12.034>
14. Sidhom, H., Yahyaoui, H., Braham, C., & Gonzalez, G. (2015). Analysis of the Deformation and Damage Mechanisms of Pearlitic Steel by EBSD and “in-situ” SEM Tensile Tests. *Journal of Materials Engineering and Performance*, 24(7), 2586–2596. <https://doi.org/10.1007/s11665-015-1537-7>

SECTION

3. CONCLUSIONS AND RECOMMENDATIONS

3.1. CONCLUSIONS

3.1.1. Impact Testing and Characterization. The results of Charpy testing at -20°C and 20°C with Charpy V- and U-notch respectively at a 66% cumulative reduction were shown to increase the notch toughness from 2.7 to 4.5 J at -20°C from the as-cast to as-rolled 830°C and 3.4 to 7.3 J at 20°C from the as-cast to as-rolled 830°C.

Quantification of as-rolled microstructure supported the notion from some literature sources that PAG size is the primary microstructural feature in these pearlitic steels indicating the increase is notch toughness, although it is also likely correlated to pearlite colony size as well. Lower temperature correlated to lower grain size which correlated with increased notch toughness in the L-S orientation, although the low temperature conditions also showed anisotropy.

By applying these concepts to thermomechanical processing trials, more recent results have been gathered which involved hot rolling at a 75% cumulative reduction. The configuration for Charpy testing and sampling are given in Figure 3.1. The adjustments to the experimental rolling procedure are given in Figure 3.2. Figure 3.3 details the experimental Charpy results obtained at 20°C given in KCU in J/cm² for comparison to the work by Getmanova et al³. The as-cast Class C impact toughness was reported at 8 J/cm² without reported orientation, therefore it is compared against the L-S and T-L orientation. The as-cast material tested experimentally had a value of 6.1 J/cm² in the L-S

and 7.1 J/cm^2 in the T-L orientation which are in good agreement. The 30%/70% trial shows similar behavior to the isothermal trials with high anisotropy but the 70%/30% trial has a mean L-S impact toughness of 16.5 J/cm^2 and mean T-L impact toughness of 13.3 J/cm^2 . The GOST 10971 Grade T has a similar C range (0.62 to 0.70 wt. % C) to AAR Class C steel under investigation (0.67 to 0.77 wt. % C) and the toughness is close to being competitive with that forged grade at 18 J/cm^2 in particular when the standard deviation is considered.

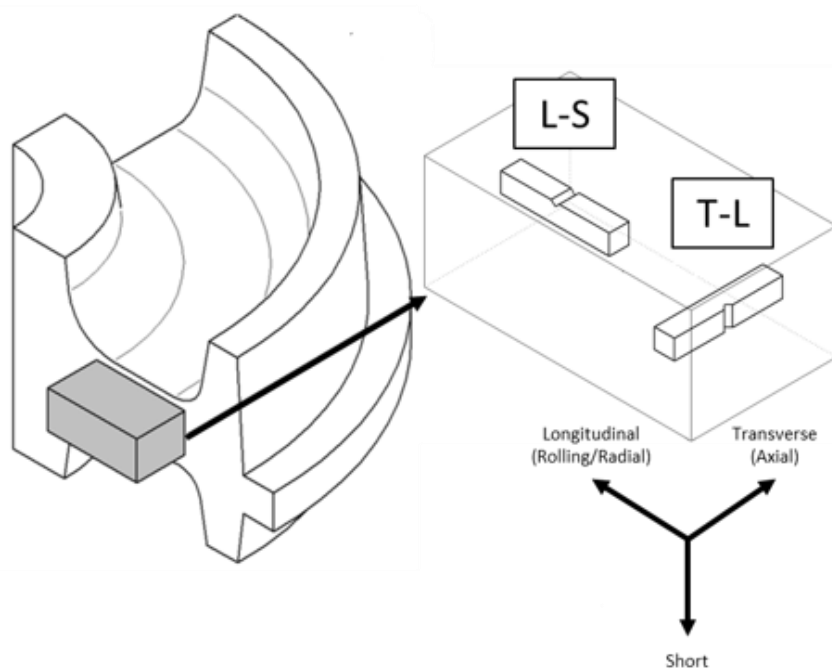


Figure 3.1. Sampling for hot rolled specimens and testing orientation.

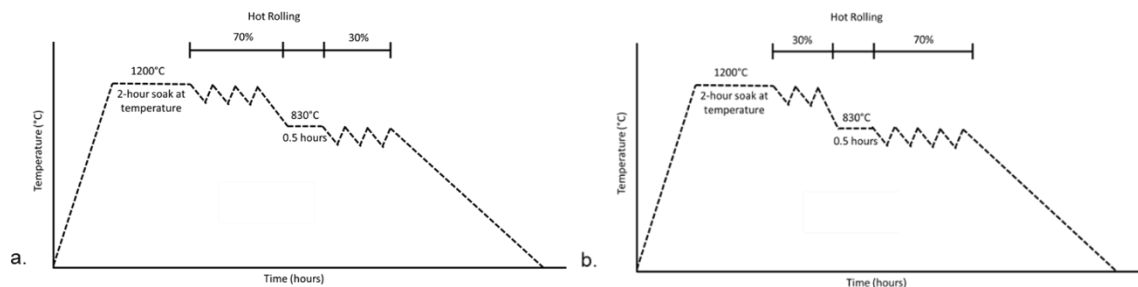


Figure 3.2. Experimental hot rolling procedures based on the isothermal rolling conditions. These include a “70/30” or 70% of the cumulative reduction at 1200°C and 30% of the overall reduction at 830°C (a), and a “30/70” procedure or 30% of the cumulative reduction at 1200°C and 70% of the overall reduction at 830°C (b).

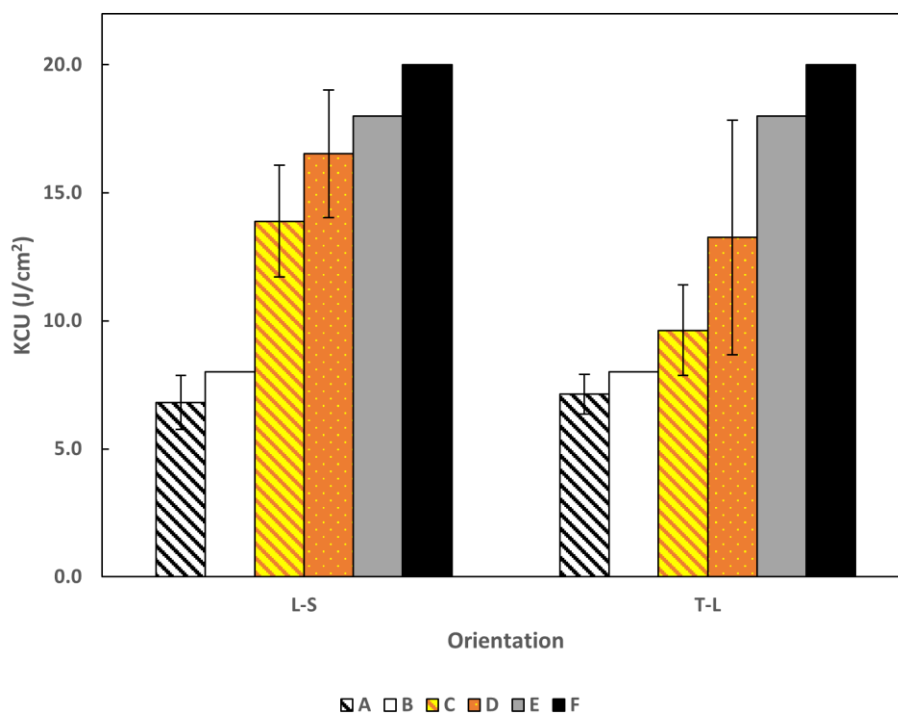


Figure 3.3. Included in this diagram are KCU (J/cm²) values for the TMP trials described in Figure 3.2. Experimental results from the industrial sponsor is included with results by Getmanova et al³ for as-cast Class C steel (B), the GOST 10971 Grade T (E), and GOST 10971 Grade 2 (F). The as-cast condition tested experimentally is given by (A) which is in good agreement with the value reported by Getmanova et al. The thermomechanical processing routes include 30% at 1200°C, 70% at 830°C (C) and 70% at 1200°C, 30% at 830°C (D). The 70/30% trial reached an average value of 16.5 J/cm² making it very close to being competitive with the forged grade Steel T which is in the same C range at a value of 18 J/cm².

3.1.2. Hot Rolling and Shrinkage Porosity and Nonmetallic Inclusions. The AFA for porosity conclusively showed that the porosity content is decreased by hot rolling at a 66% cumulative reduction from 177.5 ppm in the as-cast condition to 11.3 ppm, 34.7 ppm, 12.9 ppm, and 4.5 ppm in the as-rolled 830°C, 900°C, 1000°C, and 1200°C which also showed fairly conclusive temperature dependence in agreement with the literature but extending the relationship to lower temperatures. By selecting a representative temperature for analysis, the as-cast and as-rolled 1000°C condition were further compared using micro-X-Ray CT-scans showing the time effective and cost-effective ability to examine a large volume in comparison to AFA. It was also shown that at 66% cumulative reduction at 1000°C that 98% of shrinkage porosity greater than 15.73 μm was closed through the CT-scans and the AFA extended the analysis to micro voids ($>0.5 \mu\text{m}$) indicating that ~92% of the total porosity was closed at 1000°C.

MnS, Al_2O_3 , and complex inclusions of Al_2O_3 cores with MnS shells were the primary inclusions in the inclusion population with trace amount of mixed silicates and calcium aluminates present. MnS inclusions had increased aspect ratios for all rolling conditions with particularly large inclusions for the 830°C which correlated with an increase in area fraction MnS inclusions which was verified in the BSE cross sections. Al_2O_3 inclusions had similar area fraction, size, distribution, and aspect ratio before and after hot rolling as they are not as plastic as MnS inclusions. However, the MnS shell allowed complex inclusions to show a similar trend to MnS inclusions with increased complex inclusion area fraction showing increased aspect ratio.

3.1.3. Johnson-Cook Strength Model and Finite Element Analysis

Simulation. Through the use of hot tensile testing, a Johnson-Cook Strength model was developed based on the hot tensile properties gathered between 830°C and 1200°C and strain rates of 0.1 and 10 s⁻¹ and showed good agreement with experimental data ($R^2=0.983$). Simulation of the modified wheel rolling process resulted in information about predicted final grain size, triaxiality stresses, and roller forces allowing for a better understanding of the viability of the proposed industrial process.

3.2. RECOMMENDATIONS

This work focused primarily in deformation processing, future work pertains to the industrial processing and resulting microstructure to further improve the impact toughness. Additions of rare earth elements for inclusion engineering have been shown to improve the final morphology of NMI after hot rolling, improving anisotropy in all conditions.^{41,42} Alloy design could be used to further optimize the mechanical properties. A few researchers have investigated the use of microalloy additions to pin prior austenite grains and further refine the grain size during hot rolling through grain pinning, thus increasing impact toughness.⁴³ This typically includes Ti, V, and Nb additions of which the specification of AAR Class C steel allowing for up to 0.04 % V, 0.05% Nb, and 0.03% Ti.^{44,45} Alloy design for improving the strength of cementite and increasing proeutectoid ferrite content in eutectoid steel has been shown to be possible for a medium carbon steel which could then be modeled as shown in another work for pearlitic steels.^{46,47} The approach taken by the authors to create a FEA simulation of the wheel rolling process utilized previous work in the area and fundamentals of ring rolling

operations along with a good deal of engineering trial and error. The Forge NxT industrial software package was utilized to create this model but future work to create a model in ABAQUS may be warranted to further improve the simulation results for industrial application. Because the process in question was a modified wheel rolling process, adjustments to the traditional wheel rolling model were required which could cause problems in industrial application. An approach involving omitting the centering rolls and imposing an imaginary central mandrel to stabilize the wheel was examined as well as the approach presented. The imaginary central mandrel approach is in line with the approach by Shen et al.⁴⁸ The mandrel was found to be the most efficient for stabilization and computational time during the rolling simulation but future work to better approximate the movement of the centering rolls through development of a translational algorithm would further improve the viability of the simulation.

BIBLIOGRAPHY

1. Technical, A. A. R., Division, S., Committee, W., & Qualification, A. B. (2013). M-107/M-208 Standard: Wheels, Carbon Steel. 1–42.
2. R. LUNDEN, C. (2009). State-of-the-art research. Wheel–Rail Interface Handbook.
3. Getmanova, M. E., Ilyukhin, D. S., Nikulin, A. N., & Filippov, G. A. (2017). Composition and properties of steel in cast and forged railroad wheels. *Steel in Translation*, 47(1), 70–77. <https://doi.org/10.3103/S0967091217010065>
4. Okagata, Y. (2013). Design Technologies for Railway Wheels and Future Prospects. *新日鐵住金技報*, 395(105), 26–33.
5. BSI Standards Publication Railway rolling stock materials Part 7 : Specification for product and technical approval requirements for. (2014). 1.
6. Whitehurst, D. B. (2004). Griffin Wheel Company : railroad wheels, a better way to make them (p. 44).
7. Shu, Q., Visuri, V. V., Alatarvas, T., & Fabritius, T. (2020). Model for Inclusion Precipitation Kinetics During Solidification of Steel Applications in MnS and TiN Inclusions. *Metallurgical and Materials*
8. Yuki, N., Shibata, H., & Emi, T. (1998). Solubility of MnS in Fe-Ni Alloys as Determined by In-situ Observation of Precipitation of MnS with a Confocal Scanning Laser Microscope. *ISIJ International*, 38(4), 317–323. <https://doi.org/10.2355/isijinternational.38.317>
9. Singh, V., Lekakh, S., & Peaslee, K. (2008). Using Automated Inclusion Analysis for Casting Process Improvements. SFSA Technical and Operating Conference, Steel Founders' Society of America (SFSA), May, 1–18. http://scholarsmine.mst.edu/post_prints/pdf/TO_08_MSTInclusions_09007dcc805d93e9.
10. Cho, H. E., Hammi, Y., Bowman, A. L., Karato, S. I., Baumgardner, J. R., & Horstemeyer, M. F. (2019). A unified static and dynamic recrystallization Internal State Variable (ISV) constitutive model coupled with grain size evolution for metals and mineral aggregates. *International Journal of Plasticity*, 112(August 2018), 123–157. <https://doi.org/10.1016/j.ijplas.2018.08.009>

11. State, T. D. (2005). Recovery , Recrystallization , and Grain-Growth Structures. 14, 552–562. <https://doi.org/10.31399/asm.hb.v14a.a0004019>
12. Wheels. (n.d.). Retrieved June 30, 2020, from <https://lucchinirs.com/railway-products/wheels/>
13. Krauss, G. (2018). Microstructures, Processing, and Properties of Steels[1]. Properties and Selection: Irons, Steels, and High-Performance Alloys, 1, 126–139. <https://doi.org/10.31399/asm.hb.v01.a0001008>
14. Thomas G. Digges and Samuel J. Rosenberg. (2012). National Bureau of Standards Library Heat Treatment and Properties of Iron and Steel. 6–21.
15. Hyzak, J. M., & Bernstein, I. M. (1976). The role of microstructure on the strength and toughness of fully pearlitic steels. *Metallurgical Transactions A*, 7(8), 1217–1224. <https://doi.org/10.1007/BF02656606>
16. Doi, S. N., & Kestenbach, H. J. (1989). Determination of the pearlite nodule size in eutectoid steels. *Metallography*, 23(2), 135–146. [https://doi.org/10.1016/0026-0800\(89\)90015-3](https://doi.org/10.1016/0026-0800(89)90015-3)
17. Elwazri, A. M., Wanjara, P., & Yue, S. (2005, July 11). The effect of microstructural characteristics of pearlite on the mechanical properties of hypereutectoid steel. *Materials Science and Engineering: A*. <https://www.sciencedirect.com/science/article/pii/S0921509305005459>.
18. Zhang, M. R., & Gu, H. C. (2008). Fracture toughness of nanostructured railway wheels. *Engineering Fracture Mechanics*, 75(18), 5113–5121. <https://doi.org/10.1016/j.engfracmech.2008.07.007>
19. Zhang, F., Zhao, Y., Tan, Y., Ji, X., & Xiang, S. (2019). Study on the nucleation and growth of pearlite colony and impact toughness of eutectoid steel. *Metals*, 9(11). <https://doi.org/10.3390/met9111133>
20. Boonsukachote, P., Kingklang, S., & Uthaisangsuk, V. (2019). Modelling of mechanical properties of pearlitic rail steel. *Key Engineering Materials*, 798 KEM, 3–8. <https://doi.org/10.4028/www.scientific.net/KEM.798.3>
21. Diener, M., & Ghidini, A. (2010). Materials for heavy haul solid wheels: New experiences. *Proceedings of the Institution of Mechanical Engineers, Part F: Journal of Rail and Rapid Transit*, 224(5), 421–428. <https://doi.org/10.1243/09544097JRRT356>

22. Tanaka, Y., Pahlevani, F., Moon, S. C., Dippenaar, R., & Sahajwalla, V. (2019). In situ characterisation of MnS precipitation in high carbon steel. *Scientific Reports*, 9(1), 1–12. <https://doi.org/10.1038/s41598-019-46450-y>
23. Shu, Q., Visuri, V. V., Alatarvas, T., & Fabritius, T. (2020). Model for Inclusion Precipitation Kinetics During Solidification of Steel Applications in MnS and TiN Inclusions. *Metallurgical and Materials*
24. Yuki, N., Shibata, H., & Emi, T. (1998). Solubility of MnS in Fe-Ni Alloys as Determined by In-situ Observation of Precipitation of MnS with a Confocal Scanning Laser Microscope. *ISIJ International*, 38(4), 317–323. <https://doi.org/10.2355/isijinternational.38.317>
25. Loder, D., Michelic, S. K., Mayerhofer, A., & Bernhard, C. (2017). On the Capability of Nonmetallic Inclusions to Act as Nuclei for Acicular Ferrite in Different Steel Grades. *Metallurgical and Materials Transactions B: Process Metallurgy and Materials Processing Science*, 48(4), 1992–2006. <https://doi.org/10.1007/s11663-017-0984-y>
26. Moroz, A. N., & Glotka, A. A. (2017). Effect of the Temperature of Hot Rolling on Formation of Microdiscontinuities on Nonmetallic Inclusions in Steel ShKh15SG. *Metal Science and Heat Treatment*, 58(9–10), 574–577. <https://doi.org/10.1007/s11041-017-0058-4>
27. E1245-95. (1999). Standard Practice for Determining the Inclusion or Second-Phase Constituent Content of Metals by Automatic Image Analysis. *Annual Book of ASTM Standards*, 3.02(April), 1–8. <https://doi.org/10.1520/E1245-03R16.2>
28. Smirnov, L. A., Rovnushkin, V. A., Dobuzhskaya, A. B., Yunin, G. N., Polevoi, E. V., Boikov, D. V., & Spirin, S. A. (2016). Influence of rare-earth modification on the formation of nonmetallic inclusions in high-carbon steel. *Steel in Translation*, 46(11), 805–813. <https://doi.org/10.3103/S0967091216110127>
29. Wu, M., Zhao, F., Yang, Y., Jiang, B., Zhang, C. L., & Liu, Y. Z. (2018). The Effect of Size and Distribution of MnS Inclusions on the Austenite Grain Growth in a Low Cost Hot Forged Steel. *Steel Research International*, 89(2), 1–8. <https://doi.org/10.1002/srin.201700270>
30. Trojan, P. K. (2018). Inclusion-Forming Reactions. *Casting*, 74–83. <https://doi.org/10.31399/asm.hb.v15.a0005193>
31. 30. Han, Q. (2018). Shrinkage Porosity and Gas Porosity. *Casting*, 9, 370–374. <https://doi.org/10.31399/asm.hb.v15.a0005222>

32. Sarkar, R., Pathak, S., & Kela, D. H. (2019). Root Cause Analysis of Low Impact Toughness of Cast Steel Yokes Used in Railway Freight Cars. *Journal of Failure Analysis and Prevention*, 19(1), 76–84. <https://doi.org/10.1007/s11668-018-0565-7>
33. Davey, K., & Ward, M. J. (2002). The practicalities of ring rolling simulation for profiled rings. *Journal of Materials Processing Technology*, 125–126(January), 619–625. [https://doi.org/10.1016/S0924-0136\(02\)00356-4](https://doi.org/10.1016/S0924-0136(02)00356-4)
34. Bolin, R. (2018). Ring Rolling. *Metalworking: Bulk Forming*, 14, 136–155. <https://doi.org/10.31399/asm.hb.v14a.a0003982>
35. Shen, X., Yan, J., An, T., Xu, Z., & Zhang, J. (2014). Analysis of railway wheel rolling process based on three-dimensional simulation. *International Journal of Advanced Manufacturing Technology*, 72(1–4), 179–191.
36. Buchely, M. F., Ganguly, S., Van Aken, D. C., O'Malley, R., Lekakh, S., & Chandrashekhara, K. (2020). Experimental Development of Johnson–Cook Strength Model for Different Carbon Steel Grades and Application for Single-Pass Hot Rolling. *Steel Research International*, 91(7), 1–10. <https://doi.org/10.1002/srin.201900670>
37. D.Y. Yang, K.H. Kim, Rigid plastic finite element analysis of plane strain ring rolling, *Int. J. Mech. Sci.* 30 (1988) 541–550.
38. T.C. Tszeng, T. Altan, Investigation of ring rolling by pseudo-plane- strain FEM analysis, *J. Mater. Process. Technol.* 27 (1991) 151–161; S.G. Xu, J.C. Lian, J.B. Hawkyard, Simulation of ring rolling using a rigid–plastic finite element model, *Int. J. Mech. Sci.* 33 (5) (1991) 393–401.
39. Davey, K., & Ward, M. J. (2002). The practicalities of ring rolling simulation for profiled rings. *Journal of Materials Processing Technology*, 125–126(January), 619–625. [https://doi.org/10.1016/S0924-0136\(02\)00356-4](https://doi.org/10.1016/S0924-0136(02)00356-4)
40. Zhou, J., Gong, X. T., Yang, X. B., & Xu, W. J. (2011). Effect of drive roll rotation speed on ring rolling process. *Advanced Materials Research*, 189–193, 2586–2592. <https://doi.org/10.4028/www.scientific.net/AMR.189-193.2586>
41. Wu, M., Zhao, F., Yang, Y., Jiang, B., Zhang, C. L., & Liu, Y. Z. (2018). The Effect of Size and Distribution of MnS Inclusions on the Austenite Grain Growth in a Low Cost Hot Forged Steel. *Steel Research International*, 89(2), 1–8. <https://doi.org/10.1002/srin.201700270>

42. Smirnov, L. A., Ravnushkin, V. A., Dobuzhskaya, A. B., Yunin, G. N., Polevoi, E. V., Boikov, D. V., & Spirin, S. A. (2016). Influence of rare-earth modification on the formation of nonmetallic inclusions in high-carbon steel. *Steel in Translation*, 46(11), 805–813. <https://doi.org/10.3103/S0967091216110127>
43. K. Hulka, Dusseldorf, E. Koerfer, L. Mauritzat, K. GroB, Georgsmarienhutte, und E. Kudielka, D. (1984). Niob als Mikrolegierungselement in eutektoiden Stahlen am Beispiel der Schienenstahle. *Berg- Und Huttenmnische Monatshefte*, 129(1), 25–34.
44. Ray, A. (2017). Niobium microalloying in rail steels. *Materials Science and Technology (United Kingdom)*, 33(14), 1584–1600. <https://doi.org/10.1080/02670836.2017.1309111>
45. Wu, S., Li, X. C., Zhang, J., Shang, C. J., & Misra, R. D. K. (2015). Microstructural Refinement and Mechanical Properties of High-Speed Niobium-Microalloyed Railway Wheel Steel. *Steel Research International*, 86(7), 775–784. <https://doi.org/10.1002/srin.201400236>
46. Boonsukachote, P., Kingklang, S., & Uthaisangsuk, V. (2019). Modelling of mechanical properties of pearlitic rail steel. *Key Engineering Materials*, 798 KEM, 3–8. <https://doi.org/10.4028/www.scientific.net/KEM.798.3>
47. Zeng, D., Lu, L., Gong, Y., Zhang, N., & Gong, Y. (2016). Optimization of strength and toughness of railway wheel steel by alloy design. *Materials and Design*, 92, 998–1006. <https://doi.org/10.1016/j.matdes.2015.12.096>
48. Shen, X., Yan, J., An, T., Xu, Z., & Zhang, J. (2014). Analysis of railway wheel rolling process based on three-dimensional simulation. *International Journal of Advanced Manufacturing Technology*, 72(1–4), 179–191. <https://doi.org/10.1007/s00170-014-5637-6>

VITA

Jacob Michael Summers received his bachelors of science in Metallurgical Engineering from the Missouri University of Science and Technology in May of 2020. He received his masters of science in Metallurgical Engineering from the Missouri University of Science and Technology in May 2022.